

UNIVERSITA' DEGLI STUDI DI NAPOLI "FEDERICO II"



FACULTY OF ENGINEERING

Ph.D. Thesis in Chemical Engineering

XXIV Cycle

Department of Chemical Engineering

**WALL EFFECTS IN
PARTICLE-LADEN FLOWS**

Supervisor:

Prof. PIERO SALATINO

Ph.D. Student:

FIorenzo AMBROSINO

Scientific Committee:

Prof. PIERO SALATINO

Dr. FRANCESCO SAVERIO MARRA

Dr. FABIO MONTAGNARO

November 2011

Abstract

The aim of this study is to investigate about the complex phenomenology associated with the interaction of a particle-laden turbulent flow with the slag-covered wall of an entrained-flow gasifier. Recent observations, indeed, highlighted that this phenomenology can have an impact on the global gasifier performance greater than that expected from previous analyses. The design of new generation of entrained-flow coal gasifiers aims at favoring ash migration/deposition onto the reactor walls, whence the molten ash (slag) flows and is eventually drained separately at the bottom of the gasifier.

In terms of efficiency, the oxidation of the volatile compounds released around the particles depends upon its mixing with the fresh oxidant mixture. Therefore combustion efficiency is influenced by the spatial distribution of the particle phase, with an homogeneous distributions favoring a better mixing. From the observation that a significant number of coal particles can spent most of the time in the gasifier close to the slag layer, where usually their concentration largely increase, leads to the need to understand the effective conditions experienced before complete conversion.

An experimental evidence of a picture for the fate of coal particles has been recently assessed by analyzing the chemical composition of samples of coarse slag and slag fines generated in the ELCOGAS entrained-flow gasifier located in Puertollano, Ciudad Real (Spain). Quantitative SEM-EDX analysis of the coarse slag revealed the presence of small marks with a significant carbon content as high as 48.8%-54.2%. This fact can be explained by assuming the entrapment of not fully burned coal particles into the slag. The results of the SEM analysis performed on whole slag fines particles showed that the carbon content was larger than the value obtained from the inspection of coarse slag particles. This is particularly evident for porous particles where C-content ranged between 82.3% and 86.5%. A considerable amount of unreacted coal is therefore entrapped into the slag matrix. From this observations emerges that a certain level of spatial non homogeneity of the solid phase distribution exists. In a recently published study by Montagnaro & Salatino (2010), these data have been interpreted by assuming that different

regimes of particles-slag interaction can occur: either char entrapment inside the melt or carbon-coverage of the slag may occur, depending on properties like char density, particle diameter and impact velocity, slag viscosity, interfacial particle-slag tension. Occurrence of char entrapment prevents further progress of combustion/gasification. On the contrary, if char particles reaching the wall adhere to the slag layer's surface without being fully engulfed, the progress of combustion/gasification is still permitted. The observed high rate of coal conversion can actually be explained only if this second regime establishes on the slag surface.

The addressed considerations highlights the technological need to build up methods for the prediction of the mechanism particles clustering and segregation in condition representative of coal particle flying and converting into a gasifier.

Actually a comprehensive numerical simulation of the whole range of spatial and temporal chemical and turbulent time scales involved in a full scale gasifier, is still unfeasible due to the high computational cost: the scales of turbulence involved in the gasification processes range from sub-micron scale up to the integral scale of a gasifier reactor chamber (of the order of tens of meters). To overcome this difficulty, the approach proposed in this study is based on the development of a multilevel approach..

In a first level, the motion of particles representing classes of partially converted coal in a 3-dimensional representation of the gasifier is modeled with a Computational Fluid Dynamic (CFD) approach.. Turbulence of the flow field is described adopting the Reynolds Averaged Navier Stokes (RANS) approach, while particle motion is resolved with a Lagrangian Particle Tracking (LPT) approach. The use of the RANS method for the gas phase coupled with the LPT for the solid phase in this analysis is twofold. Firstly it has been used to address the behavior of coarse and fine coal particles trajectories when subjected to a swirl motion which induced a turbulent field. This model, while avoiding the great complexity and computational effort required by comprehensive numerical CFD models of gasifiers already proposed in the literature, is sufficient to characterize the range of conditions, in terms of momentum possessed and direction, that the different particles show when approaching the gasifier walls. The second aspect concerns the identification of regions where different mechanisms for the coal clustering becomes foreseeable: distinct regions close to the wall have been identified: finer particles could be mainly responsible of particle layering near the solid walls as they, after their first impinging on the wall, assumes a pathway parallel to the wall; in contrast, larger particles continue to bounce over the walls along the whole length of the gasifier.

The identification of these two different regions and the characterization

of particle classes representative of partially burned coal particles, was the basis for the proper setup of numerical simulations based on a Large Eddy Simulation (LES) approach in two completely different configurations. This level aims at a detailed investigation of the mechanisms of slag-particle interaction. The first is a plane particle-laden channel flow, that well represents the main features of the gasifier regions where particles move parallel to the wall. The second is a periodic particle laden curved channel flow, that best represent regions close to the wall but dominated by the external swirling flow. For these two configurations the particle interaction with the slag has been treated as a rebound on a not perfectly elastic wall. A parametric study has been conducted obtaining results for different particle sizes (representing different particle inertia) and different momentum restitution in the particle-wall impact.

Numerical multiphase simulations are based on the Eulerian-Lagrangian approach implemented in the OpenFOAM CFD framework. Both RANS and LES turbulence models are implemented for the gas phase. The equations of particles motion were solved via a Lagrangian particle tracking algorithm with the TrackToFace method. Simulations were performed involving a number of particles from 10^5 to 10^6 , a level of detail that allowed to obtain a clear picture of the multiphase flow behavior responsible for char deposition phenomena.

Numerical simulation results with the LES approach do confirm the establishment of a region near the wall slag layer (the dense-dispersed phase leading to the formation of the slag fines), in which particles impacting the slag accumulate to an extent depending on the system fluid-dynamics and on parameters such as particles Stokes number and restitution coefficient. However, particle concentration near the wall in all the simulated cases does not appear perfectly steady not evenly spatially distributed. Interestingly, the segregation of char particles near the wall is more evident for the curved channel flow geometry and is enhanced for coarser particles, making evident the role played by the effective impact with the slag not recovered by the simpler models adopted in the RANS simulations.

Acknowledgements

I wish to express my gratitude to my supervisor, Prof. Piero Salatino, for the useful and fruitful discussions on everything related to chemical reactors and the underlying physical phenomena, that has been a new matter for me.

I thank Francesco S. Marra of CNR-IRC for his constant guidance in all phases of the work development, from the study of the scientific literature to the support given to me in CFD related topics and through the mysteries of OpenFOAM. His help was essential, among other things, in developing the multilevel approach and in the interpretation of the simulation results. I remember with pleasure all chats and enthusiastic discussions on the ideas on how to improve the Lagrangian Particle Tracking of the OpenFOAM libraries.

I want to thank Fabio Montagnaro for the helpful explanations of the phenomena associated with chemical interaction between the slag and coal particles, and for sharing his information on experimental evidences collected from real operative gasifiers.

Special thanks also to Andrea Arovitola for his valuable contribution to the modeling of turbulence through the LES and RANS implementation in the solvers.

I would also like to thank my supervisors in ENEA ICT division and in particular Silvio Migliori, Giovanni Bracco and Salvatore Podda for allowing me to continue this work over the years and giving me all the needed time and necessary support for my training and self-learning in OpenFOAM. I would also thank them for supporting me in computational issues and for the opportunity to work on the CRESCO supercomputing facility.

Special thanks goes to all my colleagues and friends at HPC laboratory of the ENEA ICT division, particularly to Giuseppe Aprea, Guido Guarnieri, Agostino Funel, Roberto Ciavarella, Giovanni Ponti, Salvatore Raia, Antonio Colavincenzo and Umberto Ferrara that in these years have supported me not only through the management of various aspects of the computer center but also with lots of advices on an efficient use of computing resources and with moral support. Really thank you guys!

Finally I would like to thank my family and all my friends who, as always, patiently helped and supported me over the years.

(.....and also thanks to myself for hanging in there and accomplishing this!)

If someone is wondering..., yep, this document has been typeset using L^AT_EX.

Contents

Abstract	iii
Contents	xi
List of Tables	xiii
List of Figures	xviii
1 Introduction	1
1.1 Coal gasification	1
1.2 Relevance of particle-wall Interaction	2
1.2.1 Assessment of carbon particle segregation regimes	4
1.3 Recent experimental evidences	6
1.4 Aim and scope	9
1.4.1 Advantages of the Computational Fluid Dynamics approach	10
2 Literature review	13
2.1 Prediction of fluid dynamics and solid phase properties in the whole gasifier.	14
2.2 Prediction of ash deposition	18
3 Theoretical background	21
3.1 Physics of solid particle transport	21
3.1.1 Classification of multiphase flows	21
3.1.2 Particle motion in fluids	24
3.2 Modeling of particle-wall and particle-particle interaction	28
3.2.1 Particle-wall interactions	28
3.2.2 Inter-particle collisions	30

4	Numerical modeling	31
4.1	OpenFOAM: an open source CFD toolbox	31
4.2	Euler-Lagrangian approach	32
4.2.1	Continuous phase	33
4.2.2	Particle phase	38
4.2.3	Phases coupling	40
4.3	Lagrangian Particle Tracking	40
4.3.1	Wall interaction	42
4.4	Parallel computing	43
5	Simulations of ash particles-slag interaction: Multilevel approach	45
5.1	Rationale of the modeling approach	45
5.1.1	Discrete element model	47
5.2	U-RANS level	47
5.2.1	Configuration specification	47
5.2.2	Fluid phase	50
5.2.3	Particle phase	50
5.2.4	Results	51
5.2.5	Validation	54
5.3	From U-RANS to LES level	56
5.4	LES level	58
5.4.1	Configurations specification	59
5.4.2	Fluid phase	61
5.4.3	Particle phase	62
5.4.4	Results	63
5.4.5	Validation	72
6	Further results	83
6.1	Effect of a tangential restitution coefficient at wall	83
6.2	Effect of two-way coupling	84
7	Conclusions	87
7.1	Discussion of results	87
7.2	Future works	89
A	OpenFOAM	91
A.1	The solvers	91
A.1.1	Turbulence modeling	92
A.2	Improvement in the standard LPT algorithm	93

B Planar channel driving force	95
C On the initial conditions in the Gasifier simulations	97
Bibliography	105

List of Tables

5.1	Characteristic parameters of the two simulated clouds	51
5.2	Characteristic particle simulation parameters	63
5.3	α/α_0 validity values for different coupling levels for both planar and curved channel configurations.	80

List of Figures

1.1	Schematic diagram of the entrained-flow gasifier (from Montagnaro & Salatino, 2010).	2
1.2	Regimes of micromechanical interaction and criteria for their occurrence (E = entrapment; S = segregation; SC = segregation and coverage) (from Montagnaro & Salatino, 2009).	5
1.3	SEM micrographs of cross-sections of: a) a whole coarse slag particle (magnification = 50x); b-c) selected zones of slag particles (magnification = 1600x) displaying carbon-rich patches (from Montagnaro <i>et al.</i> , 2011).	8
1.4	SEM micrographs of different whole slag fines particles: a) at magnification = 1600x; b) at magnification = 3000x (from Montagnaro <i>et al.</i> , 2011).	8
3.1	Dilute, dispersed, and dense flow conditions based on various interphase and intraphase coupling (from Loth, 2006).	22
3.2	Classification map of dispersed two-phase flows (from Elghobashi, 2006).	24
3.3	Drag coefficient as a function of particle Reynolds number (from Sommerfeld, 2000).	26
3.4	Configuration of a particle-wall collision (from Sommerfeld, 2000).	30
4.1	Example of <i>tracktoface</i> motion of a particle during a single time step	42
5.1	2D sketch of the inlet jets of the combustor; only a portion of the gasifier is reported (from Apte <i>et al.</i> , 2003).	48
5.2	3D view of the meshed combustor inlet	49
5.3	2D view of the mesh of the combustor	49
5.4	Computational domain and grid for the 3D RANS computations	50
5.5	Wall-normal velocity component in the gasification chamber [$m s^{-1}$].	52

5.6	Velocity profiles [$m s^{-1}$] along the gasifier length [m]: $U(0)$ is the swirl component, $U(1)$ is the wall-normal component, $U(2)$ is the axial component; Velocities computed at 20 mm distance from the wall.	52
5.7	Particle mass concentration α for $d_p = 45.6 \mu m$ (right) and $d_p = 102 \mu m$ (left) in the gasification chamber.	53
5.8	Particles pathlines in the gasifier for $d_p = 45.6 \mu m$ (top) and $d_p = 102 \mu m$ (bottom) from time 8s to 10s, U magnitude scale [$m s^{-1}$] refers to particle velocity, Umean Z scale [$m s^{-1}$] refers to flow axial mean velocity.	55
5.9	Particle trajectories for $d_p = 30 \mu m$ (top) and $d_p = 100 \mu m$ (bottom) from Sommerfeld & Qiu (1993).	56
5.10	Distribution of the wall shear stress of the gasifier chamber.	57
5.11	Velocity profiles [$m s^{-1}$] in the gasifier chamber section at $z = 0.7 m$; $U(0)$ is the swirl component, $U(1)$ is the wall-normal component, $U(2)$ is the axial component;	58
5.12	Particle-laden turbulent gas flow in a periodic planar channel.	60
5.13	Particle-laden turbulent gas flow in a periodic curved channel.	61
5.14	Average particle mass concentration α/α_0 along y^+ for the planar channel, $St = 5$ and different ϵ ;	64
5.15	Average particle mass concentration α/α_0 along y^+ for the planar channel, $St = 25$ and different ϵ ;	65
5.16	Probability density function of the vertical velocity for particles close to the bottom wall of the planar channel: $St = 5$, different ϵ values;	66
5.17	Probability density function of the vertical velocity for particles close to the bottom wall of the planar channel: $\epsilon = 1$, different St values;	67
5.18	3D view of the curved channel: fluid velocity contours [$m s^{-1}$] and particle positions for $St = \{10, 50\}$ and $\epsilon = 1$ at 30s after injection;	68
5.19	Average particle mass concentration α/α_0 along y^+ for the curved channel, $St = \{10, 50\}$ and $\epsilon = 1$, 1s after injection;	68
5.20	Average particle mass concentration α/α_0 along y^+ for the curved channel, $St = 10$ and $\epsilon = \{1, 0.2\}$, 1s after injection;	69
5.21	Probability density function of the vertical velocity for particles close to the bottom wall of the curved channel: $\epsilon = 1$, different St values, 1s after injection;	69
5.22	Probability density function of the vertical velocity for particles close to the bottom wall of the curved channel for $St = 10$ and $\epsilon = \{1, 0.2\}$, 1s after injection;	70

5.23	Snapshots of the particles distribution near the wall (maximum distance less than $4mm$). Planar channel flow case. Top (left and right): $St = 5$. Bottom (left and right): $St = 25$. Left (top and bottom): $\epsilon = 0.2$. Right (top and bottom): $\epsilon = 1$	70
5.24	Particle concentration α/α_0 along the distance from points A and B in the planar channel: $St = 25$, $\epsilon = 1$	71
5.25	Total kinematic energy in the planar channel: mesh coarse (<i>LES 1</i>)	73
5.26	Total kinematic energy in the planar channel: mesh fine (<i>LES 2</i>) .	73
5.27	Velocity profiles in wall units for the planar channel for different LES levels and DNS data.	74
5.28	Averaged fluid velocities (a) and rms (b) profiles for the fine mesh <i>LES-2</i> , planar channel; velocities are dimensionless (divided by u_τ)	75
5.29	Streamwise (a) and spanwise (b) energy spectral density for coarse mesh <i>LES-1</i> , planar channel	75
5.30	Streamwise (a) and spanwise (b) energy spectral density for fine mesh <i>LES-2</i> , planar channel	76
5.31	Average streamwise fluid velocity v_θ , curved channel;	76
5.32	Average particle mass concentration α/α_0 along y^+ for the planar channel and both fine and coarse mesh, $St = 5$ and $\epsilon = 1$	77
5.33	Maximum particle concentration α/α_0 at the wall as function of time for the planar channel: $St = 5$ (top) and $St = 25$ (bottom), $\epsilon = \{1, 0.2\}$	78
5.34	Maximum particle concentration α/α_0 at the wall as function of time for the curved channel: $St = 10$ (top) and $St = 50$ (bottom), $\epsilon = \{1, 0.8, 0.5, 0.2\}$	79
5.35	Maximum particle concentration α/α_0 as function of time for different slices distribution on the planar channel: $St = 5$, $\epsilon = 1$; . . .	82
5.36	Maximum particle concentration α/α_0 as function of time for different slices distribution on the planar channel: $St = 25$, $\epsilon = 1$; . .	82
6.1	Average particle mass concentration α/α_0 along y^+ for the planar channel and both one-way and $\mu_w = \{0, 0.2, 0.5\}$, $St = 5$ and $\epsilon = 1$	84
6.2	Average particle mass concentration α/α_0 along y^+ for the planar channel and both one-way and two-way coupling models, $St = 25$ and $\epsilon = 1$	85
6.3	Probability density function of the vertical velocity for particles close to the bottom wall of the planar channel for both one-way and two-way coupling models, $St = 25$ and $\epsilon = 1$	86

7.1	Snapshot of particles and vortical turbulent structures in the planar channel configuration.	88
A.1	Particle mass fraction α/α_0 as a function of y^+ for different wall impact algorithms: $St = 25$, $\epsilon = 1$, $T = 80 s$, planar channel configuration;	94

Chapter 1

Introduction

1.1 Coal gasification

Coal combustion is considered to be among the main primary energy supply that will last for very long time. Scenarios depict that a large share of the energy demand will be supplied by coal combustion for at least more than a century from now. In contrast, coal combustion is among the most pollutant energy technologies thus requiring an huge research effort to introduce new, less pollutant combustion technologies.

Entrained-flow gasification is considered one of the best technologies for clean coal utilization; this is due to the low pollutant concentration in the released smokes obtained from this technology and due to high conversion efficiency. Modeling coal gasification under entrained-flow conditions is of great interest for the combustion community (Montagnaro & Salatino, 2009).

However there are still many areas where a lack of knowledge on the fundamental mechanisms is present. One of these areas cover the transport mechanisms that govern the motion of pulverized coal in the combustion chamber, especially in proximity of the confining walls. This problem arises not only in this specific application but also in several other technologies involving particle-laden flows, making difficult to design devices used in so many chemical engineering fields ranging from pharmaceutical to environmental. The focus of this PhD thesis is on the clean combustion technology, thus limiting the investigations to conditions usually applicable to a coal gasifier, but it is expected that the knowledge and modeling tools that will be acquired on this phenomena could be easily extended to other field of applications.

1.2 Relevance of particle-wall Interaction

The micromechanics interaction of dispersed particles and the confining walls plays a key role in determining not only the deposition rates, but also the concentration distribution of particles in the flow field and therefore, in the case of reacting particles, the map of energy release in the reactor and, as a consequence, its efficiency. This mechanism have, especially in the case of gas fluids, through the coupling of temperature with the density of the gas, a non-linear and complex interaction with the flow, making difficult the modeling prediction of these device for design purposes.

Entrained-flow gasifiers of new generation are characterized by operating conditions that promote ash migration/deposition onto the reactor walls, whence the ash is drained as a molten phase and eventually the collection of the slag at the bottom of the gasifier take place (see Figure 1.1).

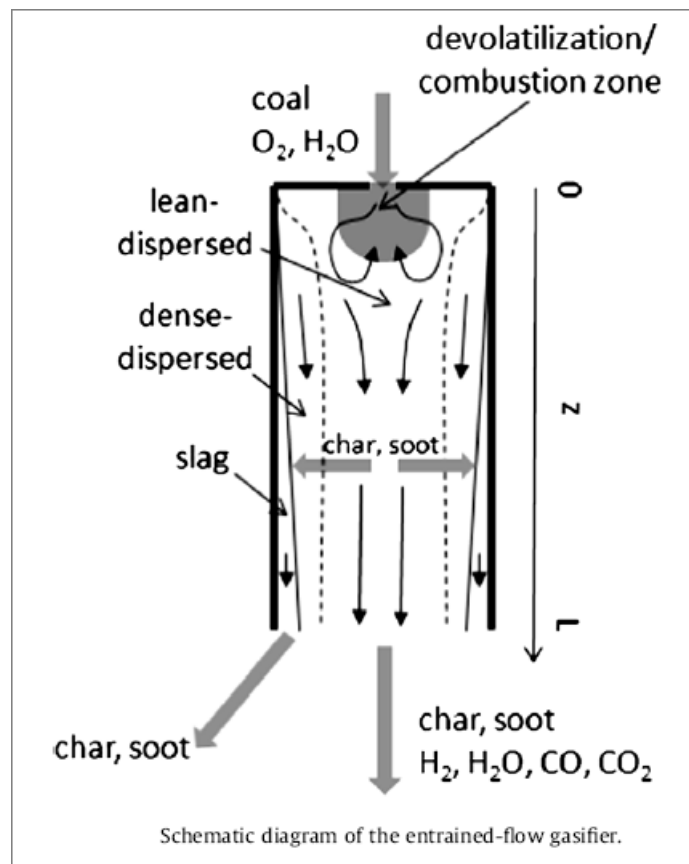


Figure 1.1: Schematic diagram of the entrained-flow gasifier (from Montagnaro & Salatino, 2010).

Modeling coal gasification under entrained-flow conditions is still a challenging goal and reveals broad areas of uncertainty despite the fact that several entrained-flow gasifiers are in operation since decades. Early one-dimensional models were based on the assumption that the gas and solid phase both moved in plug flow. At this days more comprehensive models consider the relevance of complex hydrodynamics and multiphase flow to the gasifier performance, in some cases with the aid of CFD-based detailed description of the flow, temperature and concentration fields.

Montagnaro & Salatino (2010) discussed about the possibility that coal and ash particles, injected into the gasification chamber, contribute to the formation of a dispersed particle-laden gas stream whence migration toward the chamber walls, covered by ash slag, takes place. In this context, the fate of char particles which are transferred to the molten ash slag before they are completely gasified has received limited attention and is as yet largely unknown. This aspect is relevant to the levels of unconverted carbon as well as to the thermal effects associated with the course of heterogeneous chemical reactions on the slag. Migration toward chamber walls is induced by a combination of two mechanisms:

- *inertial mechanisms*, relevant to coarser particles characterized by larger Stokes numbers, induced by strong forces associated with the main flow structures, such as centrifugal forces in swirled flows;
- *turbulence-promoted dispersive mechanisms*, driven by concentration gradients of the suspended particle phase and determined mainly by turbulence inherent to the gas phase.

The fate of char particles upon interaction with the slag layer must take into account the heterogeneous composite nature of the char, which is constituted by both ash and organic fractions where only the former is fusible at slag temperature. When particle interact with the slag layer, the inorganic fusible ash fraction is contributed to the slag, enabling its build-up. Carbon may remain segregated at the surface of the slag layer or be embodied into the ash melt depending on the combined effect of: a) particle inertia; b) ash-carbon interfacial tension, providing the driving force for carbon segregation at the slag surface; c) ash viscosity, which contrasts carbon segregation; d) buoyancy, active only in non-vertical orientation of the gasifier's walls.

Occurrence of carbon particle entrapment upon collision with the slag layer is related to the either of the following processes:

plunging of the carbon particle within the slag layer upon impact;

overlaying of carbon particles deposited on the slag layer by newly impacting ash material.

Particle plunging requires particle inertia to overcome viscous and interfacial forces, which counteract particle penetration in the slag layer upon impact. Montagnaro & Salatino (2010) developed and applied a simplified criterion for dipping and an analysis of orders of magnitude of physical quantities involved, and assumed that the phenomenon is negligible. They made also some considerations about the possibility of overlaying and found that it is not likely to occur under realistic operation of slagging gasifiers.

The establishment of a *coverage* of segregated carbon particles at the surface of a stationary slag layer, analyzed in Montagnaro & Salatino (2010), is based on competitive effects of char impingement rate and carbon gasification on the slag layer. Under slag flow conditions, slag coverage by carbon particles has been mainly interpreted as a competition of:

- a) carbon impingement on the slag layer;
- b) convective transport of the deposited carbon by the flowing slag;
- c) gasification of carbon deposited on the slag.

The impingement of small rigid sphere particles with rigid flat walls is a very well studied and understood phenomenon. The extension of this phenomenology to include the effect of stickiness due to viscosity, that is the first phenomenology just itemized, has been investigated in the past, see Wang *et al.* (2007); Shannon *et al.* (2008); Montagnaro & Salatino (2010) and references therein, with less attention to the case of impingement of particles on soft walls (Guha, 2008).

The aim of this work is therefore devoted to develop the necessary background about how the mentioned mechanisms acts in the specific situation of coal solid particle in the gasifier environment, meaning a proper characterization on terms of specific particle sizes, their physical properties and a flow motion representative of conditions in the near wall slag covered regions of a gasifier.

1.2.1 Assessment of carbon particle segregation regimes

The entrapment and the ash layer carbon-coverage criteria may combine with each other to yield different regimes as regards segregation of carbon particles as shown in Figure 1.2:

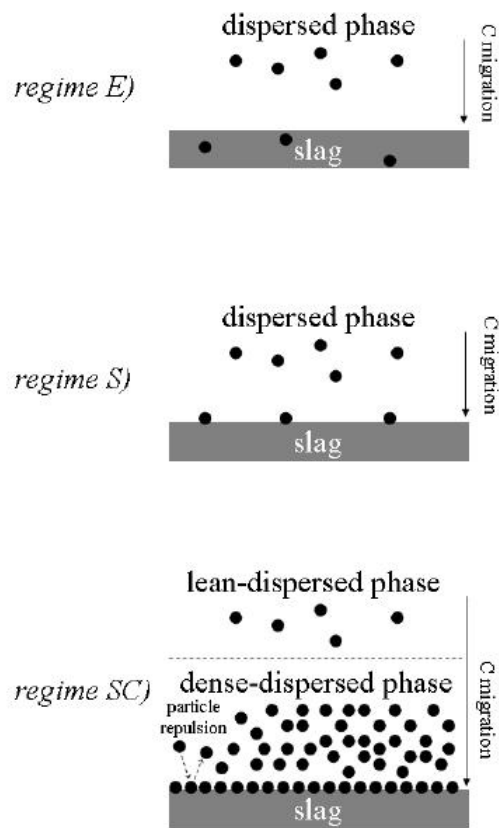


Figure 1.2: Regimes of micromechanical interaction and criteria for their occurrence (E = entrapment; S = segregation; SC = segregation and coverage) (from Montagnaro & Salatino, 2009).

Regime E) (entrapped carbon regime): this regime is established when particle entrapment takes place. If the entrapment criterion is not satisfied and segregation of C-particles is effective, two additional subregimes may establish.

Regime S) (segregated carbon regime - incomplete carbon-coverage of the ash wall layer): this regime is established when coverage of the slag layer with refractory carbon particles is not complete. Further progress of carbon combustion and gasification is permitted in this regime.

Regime SC) (segregated carbon regime - extensive carbon-coverage of the ash wall layer): is established when coverage of the slag layer with refractory carbon particles is extensive.

Results from the literature suggest that inelastic interaction of particle-laden gas with an inelastic wall (Horn & Schmid, 2008) promotes particle accumulation in the near-wall region. It is inferred that a dense-dispersed annular phase is established in the close proximity of the wall ash layer in the SC regime, whose motion is driven by momentum transfer with the neighboring phases: the high-velocity lean-dispersed phase traveling in the core of the gasifier and the slowly moving ash wall layer.

1.3 Recent experimental evidences

In an experimental investigation done by Montagnaro *et al.* (2011), solid residues coming from an industrial-scale entrained-flow slagging gasifier have been characterized. All references to experimental evidences reported in this section are made by Montagnaro *et al.* (2011) and are discussed also in Ambrosino *et al.* (2011a).

The properties of the different ash streams have been analyzed in the light of the different regimes of char-slag micromechanical interaction and of the different phases that are established in the gasification chamber (see Figure 1.1). In this context, it is useful to remind that the solid waste other than fly ash is quenched in a water bath generating, besides the slag (sometimes referred to as *coarse slag*), a black water whence *slag fines* are recovered by filtration (Wu *et al.*, 2007). Only recently differences between coarse and fine slag received consideration: the reader is referred, for example, to the works of Wu *et al.* (2007); Xu *et al.* (2009b); Zhao *et al.* (2010).

Samples of coarse slag and slag fines were generated in the ELCOGAS entrained-flow gasifier located in Puertollano, Ciudad Real (Spain). This

material was provided in the summer of 2009 and it might not be fully representative of the ash generated by the industrial gasifier during normal operation. While elemental analysis on slag did not highlight the presence of carbon in this material, interestingly, different results were obtained when cross-sections of coarse slag particles were analyzed by Scanning Electron Microscopy/Energy Dispersive X-ray (SEM-EDX) analysis as shown in Figure 1.3-a. The whole slag particle shown in Figure 1.3-a appeared to be mostly vitreous and dense. While the inorganic fraction is primarily constituted by Si+Al (47.5%), a considerable amount of carbon (9.3%) could also be detected. Figures 1.3-bc report SEM results obtained carrying out the analysis at a greater magnification on the cross-section of two selected zones of slag particles. In both cases the occurrence of darker patches was observed. Quantitative EDX results refer to these regions: C-contents as high as 48.8%-54.2% were obtained. This finding contributes to the assessment of the relevance of carbon entrapment in slag particles. It is worth to note that elemental analysis did not show the presence of any organic fraction and this was essentially because C was permanently embedded into the slag matrix in a way that could not have been disclosed by thermal analysis. Only the cutting procedure associated with the SEM-EDX analysis was able to disclose the unreacted carbon, which appeared to be somewhat segregated (in the patches) with respect to the inorganic slag matrix. Figure 1.4 reports the results of the SEM analysis performed on whole slag fines particles. In particular, particles having prevailing either porous (Figure 1.4-a) or compact (Figure 1.4-b) structures were observed. In any case, the carbon content was larger than the value obtained from the inspection of coarse slag particles, in line with results of elemental analysis. This is particularly evident for porous particles (Figure 1.4-a): C-content ranged between 82.3% and 86.5%. Thus, these particles should be mainly associated with unreacted char present in the dense-dispersed phase giving rise to slag fines upon impingement on the quench bath. On the other hand, dense particles (Figure 1.4-b) display morphological and chemical features that are closer to coarse slag particles, at least as far as SEM-EDX results are concerned: C-content ranged between 13.9% and 18.4%, and the Si+Al fraction was as high as 33.1%-35.0%.

These results are consistent with the previously reported C-content of slag fines (about 57%), obtained by standard elemental analysis carried out on waste containing both high-C porous and low-C dense materials. Moreover, the more compact slag fines should be regarded as having intermediate properties between porous slag fines and coarse slag: this observation highlights again the establishment of a dense-dispersed phase that, together with the slag phase, generates both streams: slag and slag fines, the latter being characterized by a mean particle size and density around 100 μm and 1000

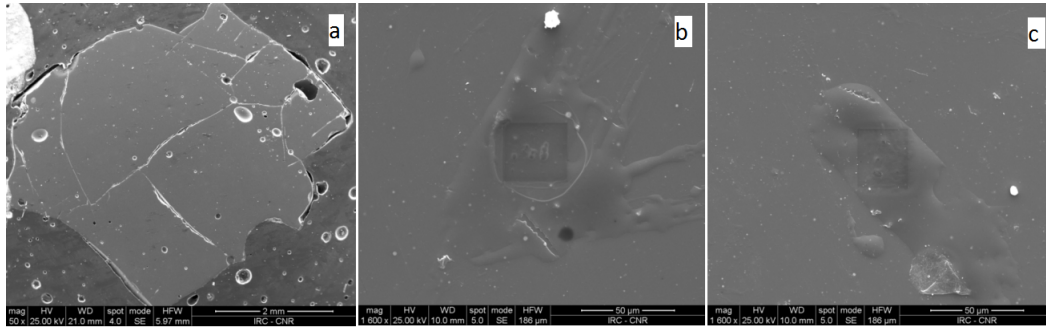


Figure 1.3: SEM micrographs of cross-sections of: a) a whole coarse slag particle (magnification = 50x); b)-c) selected zones of slag particles (magnification = 1600x) displaying carbon-rich patches (from Montagnaro *et al.*, 2011).

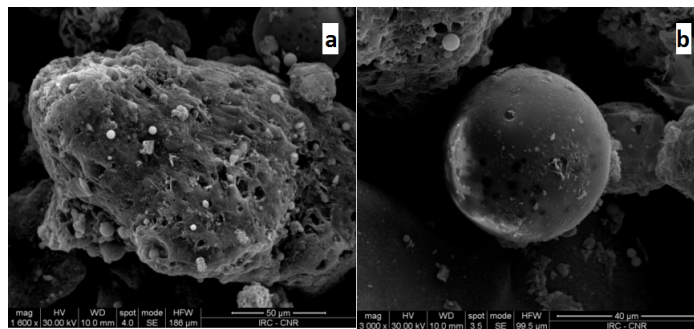


Figure 1.4: SEM micrographs of different whole slag fines particles: a) at magnification = 1600x; b) at magnification = 3000x (from Montagnaro *et al.*, 2011).

$kg\ m^{-3}$, respectively.

1.4 Aim and scope

The aim of this study is to investigate about the complex phenomenology associated with interaction of a particle-laden turbulent flow with the slag-covered wall of an entrained flow gasifier. As discussed in section 1.3, there are experimental evidences that indicate the likely establishment of a segregated solid phase in the near wall region of the gasifier. On one side Montagnaro & Salatino (2010) have proposed different possible regimes of coal particle-wall interaction as discussed in section 1.2.1, on the other side this work wants to set up a numerical model that describes the interaction mechanics giving possible reasons of the establishment (or not) of one or more regimes characterizing them with respect to operating parameters of the gasifiers. Details of the numerical model are given in chapter 4 while details of the implemented multilevel approach of CFD-DEM simulations and related results are described in chapter 5.

The multilevel approach has built to study the phenomena on different scales: from the scale related to the entire gasifier geometry to the more accurate modeling of less extended near wall zones. This approach is very well suitable for parametrize the different and most important phenomena that occur in the particle-wall interaction mechanics. It is possible indeed to characterize fluid dynamic effects of the swirled flow and turbulence, particle properties such as their inertia and part of the mechanics of the particle-slag collision via restitution coefficients of a non elastic rebound. Being a multilevel system there is also the advantage of the possibility of study very complex phenomena that would be computationally prohibitive otherwise. As discussed in the next section however, the computational cost of proposed simulations is still expensive so it was not possible to do a campaign of simulations that could give a exhaustive study of the phenomenon with respect to all parameters previously described. Main studied parameter effects are particle inertia and wall normal restitution for motion of particles driven by both turbophoresis and swirl.

In the chapter 2 will be shown an overview on the state of the art about the physical mechanism of the char particle-slag interaction in the gasifier/combustor in operation. Chapter 3 will discuss of the theoretical background behind the physics of solid particle transport, with particular care about particle-wall and particle-particle interaction. A brief overview on confined particle laden flows will be discussed in the light of the recent and important results obtained by the scientific community. Chapter 4 will

focus on the numerical modeling: the structure and of the CFD OpenFOAM package, the Eulerian-Lagrangian approach, Lagrangian Particle Tracking (LPT) and about the High Performance Computing (HPC) system. Chapter 5 will discuss about the multilevel simulation approach and relative results obtained.

1.4.1 Advantages of the Computational Fluid Dynamics approach

Conducting experimental analysis on industrial plants is typically very costly. In fact, a considerable effort must be done to retrieve detailed information on physical quantities such as local fluid properties and velocity, and those related to the dispersed solid particles such as their velocity, mass, location and so on. Moreover a less invasive techniques should to be used to avoid disturbing the values of variables that are of interest. It should be also considered that to investigate a single effect of each parameter, an experimental campaign made by a large number of experiments must be designed and this is the main reason of high costs.

Computational fluid dynamic (CFD) simulations can be less expensive and more accurate depending on modeling accuracy and computational resources. It is not too difficult to obtaining a large number of data related to each fluid property and related to each dispersed simulated particle. This abundance of data is very useful to build statistical information, particularly for turbulent flows.

It should be noted, however, that accurate CFD simulations of turbulent dispersed flows on industrial plants are still a very difficult task in terms of computational cost (in fact the scales of turbulence involved in the gasification processes range from sub-micron scale up to the integral scale of a gasifier reactor chamber). As already mentioned, to overcome this difficulty, the approach proposed in this study is based on the development of a multilevel approach (Ambrosino *et al.* , 2011b). In a first level turbulence of the flow field is described adopting the Reynolds Averaged Navier Stokes (RANS) approach, while particle motion is resolved with a Lagrangian Particle Tracking (LPT) approach. In the second level numerical modeling of turbulence is based on a Large Eddy Simulation (LES) approach. At this latter level, configurations made by small domains, in comparison to the gasifier scale, have been studied. The building up of the multilevel model has required to develop several codes (see appendix A), the implementation of appropriate numerical models (see chapter 4) and the availability of adequate computing power. In fact, as will be shown in section 4.4, the computational

effort required to solve turbulence with a defined level of accuracy was not at all trivial. In this study, all simulations at both levels on every studied configuration have been performed on the HPC system CRESCO of ENEA, the Italian agency for new technologies, Energy and sustainable economic development, situated in Portici, Naples (Italy).

Chapter 2

Literature review

IGCC (Integrated coal Gasification Combined Cycle) is a promising technology, allowing for an easier Carbon Capture and Sequestration (CCS) while maintaining, or even increasing, the overall efficiency of the energy conversion process.

A summary of the most important features of this type of plants for electricity power production can be found in Maurstad (2005).

An important unit of such plants is the gasifier. Here the coal burns to release thermal energy and it is transformed into residual minerals and syngas for further energy conversion and thermal processes. An high combustion efficiency is obtained by feeding pulverized coal, oxidant (air or oxygen) into the furnace at high speed from tangentially placed injectors, to promote swirling flow and centrifugal motion of particles towards the walls. In this way the residence time is increased too.

The gasification process, conducted at high pressure and temperature, is thus allowed to complete, especially for fine coal particles. The highest coal conversion efficiency can be realized in entrained-flow dry gasifiers: observed efficiencies in pilot plants ranges from 98 to 99.5%. However, this efficiency can dramatically reduce in many practical situations. It is common to observe an high unreacted carbon content in the slag, up to a value of 60% (Xu *et al.*, 2009a). A review of the performance for several type of gasifier can be found in Mondal *et al.* (2011).

The overall efficiency is influenced by several factors. We can group these factors following the different main processes involved:

- the fluid dynamics of both gas (mainly oxygen) and solid (mainly pulverized coal) inside the gasifier;
- the physical and chemical transformations leading to the production of syngas and residues;

- the physics governing the exchange terms occurring at the gasifier boundaries, mainly the mass accumulation from the solid flying ash into the slag and the energy flux.

Among all these factors, strongly interconnected, this study focus on the mass transfer that occurs at the confining walls, in form of transfer of mass from the coal particles that undergo a combustion process and the forming slag covering the side walls of the gasifier.

Under this perspective, three different groups of literature results need to be collected to understand the present state of the art.

The first comes from the work dealing with the overall gasifier functioning. This body of literature establish the global parameters, such as the particle composition and size, their velocity in the gasifier, the average residence time as well the characteristic temperatures encountered during their flight and the typical properties of the oxidant gas environment. To this group belong all the papers describing the gasifier modeling with a lumped parameters approach, leading to the formulation of 0D, 1D or 1.5D models. In the same way, papers relevant to the detailed numerical simulation of the whole gasifier plant, belong to the same group.

Myhnen & Hyppnen (2011) recently reviewed the several approaches that can be adopted to model a gasifier with the previously mentioned approaches.

Among the second group of papers, only those focusing on the properties of the coal products that will participate in the formation of the slag and the mechanisms of ash deposition will be here considered.

The third is relevant to the micro-mechanical and thermodynamical mechanisms involved in the interaction of solid particles with a confining wall, and more specifically with a liquid phase surface formed by the molten deposit collected at the gasifier walls.

2.1 Prediction of fluid dynamics and solid phase properties in the whole gasifier.

The number of parameters influencing a gasifier behavior is so high that it results very difficult to predict their performance. Some general indications can be, of course, obtained by simple reasoning. For instance, it is immediately realized that the way coal particles are injected into the gasifier strongly influence the overall conversion efficiency. Very small coal particle dimensions promote the heat up and the reaction of carbon with the surrounding hot oxidant and steam as they flow through the gasifier, but are immediately dragged by the flow reducing the ability to separate the residual mineral

matter. While thermal cracking reactions and pyrolysis can be considered weakly affected by the particle concentration, the oxidation of the volatile compounds released around the particles depends upon its mixing with the fresh oxidant mixture. Therefore combustion efficiency is influenced by the spatial distribution of the particle phase, with an homogeneous distributions favoring a better mixing.

Successive use of the flue gases in turbines for the electricity production or into units for CO₂ sequestration and capture, require a very small particulate concentration. This is another reason why the design of new generation of entrained-flow coal gasifiers aims at favoring ash migration/deposition onto the reactor walls, whence the molten ash (slag) flows and is eventually drained separately at the bottom of the gasifier Shimizu & Tominaga (2006).

It clearly appears that a proper prediction of the fate of burning particles is crucial for proper design and scale up, especially in regions close to the gasifier walls Seggiani (1998), where large part of the oxidation process takes place under a competition between the release of a large amount of volatile compounds and the poor mixing conditions with the oxidant mixture due to the hindered flow motion, both effects due to the presence of a dense dispersed solid phase.

Several gasifier models have been presented in the past, with different levels of approximation. The simplest approach is to model the gasifier as a chemical reactor with state variables representing average conditions, usually along the gasifier length, following a plug-flow approximation.

Even if this is a very crude approach, requiring a lot of empiricism to describe effects that depends upon non uniformity of spatial field distributions, they possess the great advantage to be very simple and of immediate integration, allowing to obtain a prompt order of magnitude evaluation of the most important working parameters and to perform sensitivity analyses to establish suitable operative conditions. These advantages promote the continuous developing of these models. To this approach belong the models recently proposed by Montagnaro & Salatino (2010) and Sun *et al.* (2011).

In this study, such models will be adopted to define the order of magnitude for the properties of gas phase inside the reactor, the typical particle size distribution coming from the burning coal particles when they reach the surface and their composition in the range from fresh coal to fully burned, ash particles. Of course, they cannot give information about the spatial distribution of the main fields.

A much more accurate evaluation of these properties can nowadays be obtained by adopting a Computational Fluid Dynamics (CFD) approach. With this approach the full description of the field of state variables is directly attempted, with simplifications belonging to the possibility to reduce the total

number of degree of freedom by establishing proper filters of the governing equations. The governing equations are invariably the balance equations for mass, momentum and energy. The filtering procedure applied to this equations will establish the effective methodology adopted. Thus, by applying a time filter, the form of the RANS (Reynolds Averaged Navier Stokes) equation is obtained. This appears the most appropriate, and computationally feasible, form to obtain the solution of the so called comprehensive models of the whole gasifier and is almost invariably applied in all the models presented in the literature.

One of the oldest work to build a comprehensive combustion model for coal combustion was the development during the first 90th years of the PCGC-3 code Richards *et al.* (1993); Hill *et al.* (2000). The computational power available at that time constrained the model to be relatively simple but already included all the most important effects recognizable at a global length scale: turbulence, particle devolatilization, char oxidation, gas phase combustion, radiation, NO_x pollutant formation were all included with proper formulation of submodels. It is worth to note that several approaches adopted to formulate these submodels have been successively confirmed by many of the following models: the Reynolds Averaged formulation of the Navier-Stokes governing the gas phase equation coupled with a two equation model for the closure of the turbulence model, and a Lagrangian formulation of the solid phase, that include only a one way coupling with the gas phase, are the choices confirmed in almost all the following development presented in the recent literature. Less attention in this work has been devoted to the deposition of particles on the gasifier walls.

A first attempt to include a model for the particle deposition rate and slag formation into a 3D-CFD code for the numerical simulation of a gasifier is probably due to Seggiani (1998). Starting from the experimental observation of the Prenflo coal gasifier installed in Puertollano, Spain, he derived an empirical model of the slag to be included in 3D CFD models of gasifiers. In this model no attempt is made to determine the portion of impinging ash particles that are able to be entrapped into the slag, just assuming that all particles that reach the slag surface perfectly stick.

Quite immediately, the need to include a proper modeling of the slag formation arose.

Tominaga *et al.* (2000) developed a model, based on the general purpose commercial CFD package FLUENT, based on assumption similar to the model PCGC-3. They clearly recognized the critical lack of information available on the slag formation recognizing that in the literature existent at that time "*The mechanisms and criteria for ash particle deposition were hardly mentioned, even though ash deposition on the wall of a slag tap reac-*

tor would control particle entrainment that would, in turn, have significant effects on carbon conversion in the reactor". Performing a sensitivity analysis with different numerical simulation of a pilot gasifier, they recognized the limit of models simply based on the number of impingements of particle onto the wall surfaces. Then an empirical model for the slag formation was proposed, mainly based on a correlation between the ash and slag viscosity and the efficiency of the deposition rate of impinging particles. A similar approach was proposed also by Fan *et al.* (2001); Tomeczek *et al.* (2004). These work differ mainly in the way the sticking efficiency is correlated to the chemical properties of coal.

The difficulty to relate the ash deposition rate with the properties of the mineral matter and transformation of coal particles was recognized by Chen *et al.* (2001). They highlighted the gap due to the strong influence of the effective flow conditions in the gasifier. Their effort, however, concentrated in the improvement of models for the gas phase, leading only indirect indications for the ash deposition rates.

In his PhD Thesis, Benyon (2002) proposed a model for the ash deposition, mainly based on a inertial impact hypothesis, that included some mechanistic criteria, based on angle of impact (> 20 degrees), particle velocity (> 5 m/s), particle temperature (presence of a liquid phase in the particle), slag temperature (liquid surface). Further hypotheses of the model are that *"On adhesion it is assumed that the ash in the particle melts and completely mixes with any existing slag layer. It is also assumed that the slag is in equilibrium and is not undergoing phase change. Any residual carbon in the particle is allowed to continue heterogeneous reaction by releasing it back into the gas stream in the same manner as if the particle did not adhere. It is released at a small distance from the wall at the point of impact with its velocity set to zero"*.

A collaborative work promoted by the Department of Energy in the USA (Bockelie *et al.* , 2002) still proposed a model based on main assumptions similar to that proposed in the PCGC-3 model, with improvements mainly due to inclusion of more accurate schemes. In that work, the role of the ash deposition mechanism is limited to the formation of the slag layer.

Watanabe & Otaka (2006) also proposed a variant of the previously reported models. Watanabe *et al.* (2009) were probably the first to propose the use of more sophisticated approach for the modeling of the gas phase in a gasifier, based on the adoption of the formulation of spatially filtered Navier-Stokes (Large Eddy Simulation). This model, however, was only restricted to the computation of the cold flow in the gasifier, due to the great increase of computation effort required but the adoption of more accurate model for the gas phase was clearly recognized. In the same year, equally recognizing the

need of a better prediction still required for the gas phase, Wu *et al.* (2009) proposed an analysis of the range of fluctuations observable in a gasifier. From this analysis, it results that the RANS approach can hardly correctly predict the flame behavior of particle coal combustion. Unfortunately, the analysis does not include the range of scale at the particle-wall interaction but it is easy to recognize the even more severe discrepancy between the scales typical of the boundary layer and those adopted in RANS simulations close to the walls.

Very recently, under the increasing pressure of the demand of clean coal technologies, the effort for a good modeling of coal gasifiers is also increased.

Many improvements are being included in the models, like alternative formulations of the two equations turbulent closure models that are able to better describe recirculating flows (RNG $k - \varepsilon$, $k - \omega$, etc.), tuning of the devolatilization and combustion mechanisms, allowing to study different gasifier configurations Silaen & Wang (2010); Slezak *et al.* (2010). Still less attention is devoted to a proper modeling of the fate of particles moving close to the walls, where the modeling of particle deposition rate rely on some criteria depending upon inertial impacts.

A further enhancement of the numerical models, especially for the particle phase, was very recently proposed by Snider *et al.* (2011). The proposed formulation have the great advantage that allows, also in application to the full scale gasifier, the inclusion of the full four-way interaction between the gas and the solid phases.

2.2 Prediction of ash deposition

The prediction of ash deposition is an old question due to its importance in the determination of the overall performance of reactors, coal burners and gasifiers in particular.

Several factors influencing the deposition of ash on solid surface, that in practical applications are often the tank tubes for heat recovery, have been clearly recognized. Following Huang *et al.* (1996), they include: *"initial composition of the coal and variation in inorganic content over different particle sizes; ash-intermediate formation during the combustion process and the nature of the ash formed; this is necessary since inorganic material tends to be distributed differently over each size range; aerodynamic influences within the boiler and their effect on the local combustion environment; coalescence of ash particles and the deposition of flame volatilized species on the fly ash; deposition of the fly ash on heat exchange and boiler surfaces (this requires consideration both of the different mechanisms and of the physical and chem-*

ical nature of the deposition surface itself); the nature of the deposit formed, i.e. whether it becomes sintered or is easily eroded”.

The submodel for the prediction of ash deposition included in the previously mentioned PCGC-3 code is described extensively in Wang *et al.* (1997).

The complexity of the phenomenology was recognized by Lee & Lockwood (1999). They indicated that the property of the slag surface have an important role in determining the effective ash deposition rate. However the only role played in this analysis was a modification of the sticking efficiency upon impaction. Actually, by modeling the gas phase in the RANS framework, it is not possible to include the effects of the turbulent flow structures close to the wall and therefore the real shape of the trajectories of particles rebounding over a soft material.

Costen *et al.* (2000) proposed a model for the particle arrival rate that depend on the determination of a critical velocity at the border of the viscous sub-layer. They estimated a critical velocity as the ratio between the viscous sublayer thickness and the particle’s relaxation time. It is then assumed that if the velocity of a particle crossing this border is higher than the critical velocity, the particle is able to deposit onto the surface, with an efficiency proportional to a viscosity index. Otherwise, it will be transported by the flow to the outlet remaining entrapped in the viscous sublayer. Indirectly they established a criterion for the existence of a dense layer of particles over the slag.

A similar approach was proposed also by Pyykonen *et al.* (2002). However they recognized the additional difficulties that arise when modeling the ash deposition rate over furnace walls in comparison to deposition rate over cooling tubes, due to the need to distinguish between at least two different possible mechanisms: inertial impaction and turbulent impaction. The proposed model try to take into account the flow field structure that establishes close to the walls by adopting empirical correlations. A similar approach was followed also by Mueller *et al.* (2005), by including several effects that depends upon coal particle composition and angle of impact.

The slagging behavior of 12 different coals/blends was analyzed by Barroso *et al.* (2007) in an entrained flow reactor. They observed large discrepancies in the sticking efficiencies and proposed a new approach to account for the effect of the aerodynamic diameter and the total mass of mineral matter injected with the coal.

A first attempt to build a dynamic mechanistic model of ash deposition is reported in Zhou *et al.* (2007). This work focus only on the deposition of solid particles over cooling tube, a situation clearly different from the interaction with a molten slag, but it is recognized the need to include at an

increased level the detail of the particle-surface interaction.

Following a similar reasoning, Wang *et al.* (2007) proposed a further enhancement of ash deposition models that takes into account the possibility of wall burning, i.e. the fact that not fully burnt coal particles can continue to burn on the slag surface, changing the local properties of the thermo-fluid dynamic fields. It is maybe the first time that local non uniformity effects play a role into ash deposition models.

More recently Li *et al.* (2010) investigated the fate of particles impacting onto a solid surface. Their analysis elucidated the effect of the different level of burning of coal particles, clarifying the possible mechanism for particles at an intermediate level of burning. However the main mechanism assumed for the particle-slag interaction was still that of inertial impaction, despite that the prevalence of this mechanism with respect to near wall effects has been never definitively proven.

This mechanism is still at the basis of recent investigation on the slagging behavior of gasifier Fang *et al.* (2010); Li *et al.* (2010).

Chapter 3

Theoretical background

3.1 Physics of solid particle transport

3.1.1 Classification of multiphase flows

In general, to numerically model a multiphase flow, it is often important to use separate formulations for the different phases. The particle phase represents the phase that consists of particles (and in general bubbles, drops and so on) and the continuous phase the fluid in which these particles are generally immersed. The particles can be composed of solid, liquid, or gas, whereas the continuous fluid can be a liquid or a gas. The coupling between the particle motion and its surroundings can be used to classify the character of the multiphase flow, and thus help determine appropriate numerical techniques. The broadest division is between dispersed and dense flows, and refers to which coupling mechanism primarily determines the particle motion (Loth, 2006).

As shown in Figure 3.1, a multiphase flow can be considered dispersed if the effect of particle-fluid interactions dominates the overall transport of the particles. Particle-fluid interaction generally includes a drag force, which hinders the relative velocity of the particle, and thus causes particle trajectories to tend toward continuous-fluid trajectories. In dilute dispersed systems the spacing between particles is rather large (i.e. bigger than 100 particle diameters), so a direct interaction between particles is rare and fluid dynamic forces are governing particle transport. If the particle-particle motion dominates, the flow can be considered to be dense. In dense dispersed systems the inter-particle spacing is comparatively low (i.e. smaller than 10 particle diameters) and the transport of particles is considered to be strongly influenced by collisions between them.

Dispersed flow will generally include one-way coupling (where the dispersed-

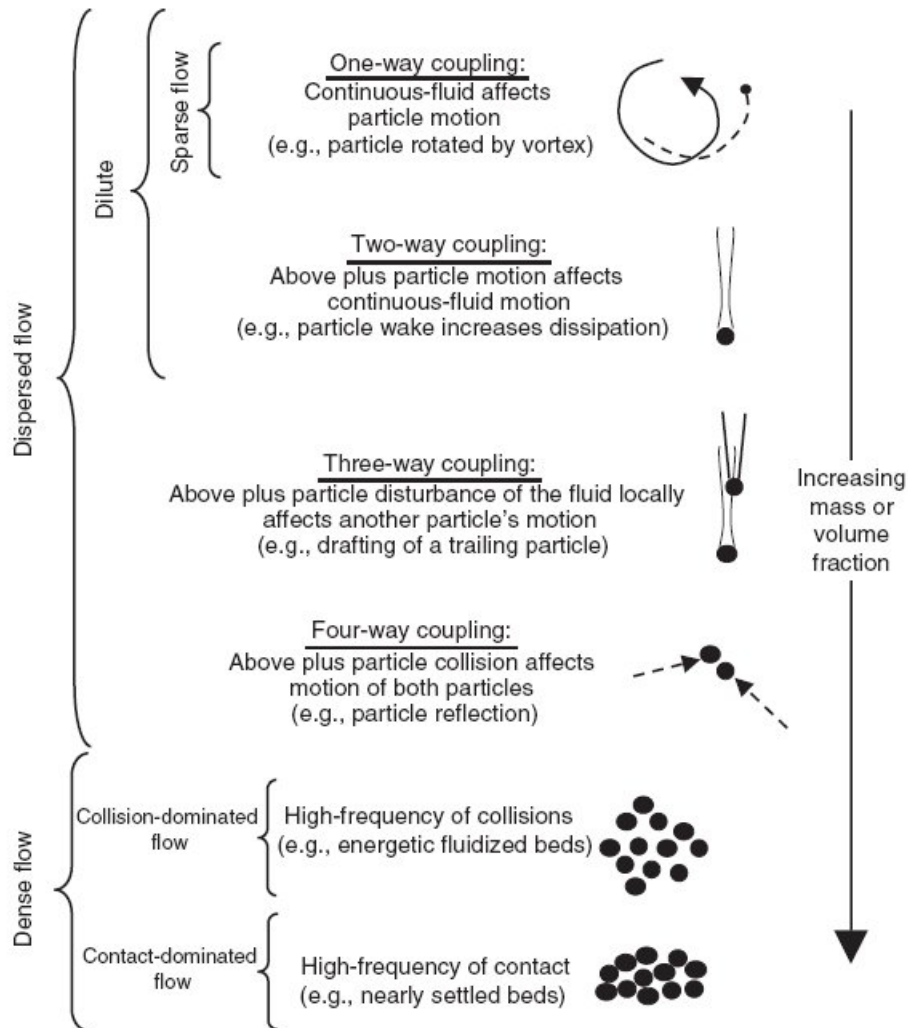


Figure 3.1: Dilute, dispersed, and dense flow conditions based on various inter-phase and intraphase coupling (from Loth, 2006).

phase motion is affected by the continuous phase, but not vice versa), two-way coupling (where the dispersed phase also affects the continuous phase), and four-way coupling (where collisions and other particle-particle interactions influence the overall particle motion). Dense flows will be generally defined as having four-way coupling, although in some cases (e.g., granular flows), the effects of the particles on the continuous fluid are weak and often neglected (Loth, 2006).

Let consider a gasifier similar to the one considered by Montagnaro & Salatino (2009) in order to obtain characteristic values of particle concentration and coupling levels. Considering so the *lean* phase and averaged values in the middle and terminal part of the gasifier. The total mass flow rate of solid (coal and ash) is about $F_c = 0.1 \text{ kg s}^{-1}$, the gas volumetric flow rate is about $Q = 0.36 \text{ m}^3 \text{ s}^{-1}$ and the gas density (at $p = 28 \text{ bar}$ and $T = 1800 \text{ K}$) is about $\rho_f = 5 \text{ kg m}^{-3}$. So, in steady conditions, the mean mass particle concentration in the *lean* phase is about $\alpha_0 = 0.05$ (the particles density considered is about $\rho_p = 1000 \text{ kg m}^{-3}$). Considering the *dense* phase described in the same paper, the total mass flow rate of solid (coal and ash) is about $F_c = 0.3 \text{ kg s}^{-1}$ and the velocity of the *dense* phase is about $v = 0.05 \text{ m s}^{-1}$. To obtain an estimate of the particle concentration it is necessary an estimate of the *dense* layer thickness. This thickness δ can be written as a function of the mass particle concentration α : in $t = 1 \text{ s}$ a solid mass of $M_c = F_c/v = 6 \text{ kg}$ occupies a volume that is a cylindrical segment of diameter $D = 1 \text{ m}$, that is the gasifier diameter, height $h = 1 \text{ m}$ and thickness δ ; being

$$\alpha \approx \frac{M_c}{\pi D h \delta \rho_f}$$

the thickness δ is inversely proportional to the mass particle concentration of the *dense* phase by

$$\delta \approx \frac{M_c}{\pi D h \alpha \rho_f}$$

The thickness δ is about 2.7 mm for a limit mass particle concentration of about $\alpha = 740$ (related to the maximum packing ratio of spheres) and should be about 2 m for $\alpha = 1$ that are the limit values of the four-way coupling application range. Being $\delta \leq D/2$ can be inferred that should be considered the particle-particle interaction in the *dense* phase.

In Figure 3.2 is shown a classification map of dispersed two-phase flows from Elghobashi (2006). In that figure the particle concentration α is a volumetric concentration so the mass particle concentration is obtained multiplying it by ρ_p/ρ_f . When the volume fraction is in the two-way coupling range, the particles enhance turbulence (zone B of the figure, if $\tau_p/\tau_k > 10$)

or dissipation (zone A of the figure, if $\tau_p/\tau_k < 10$). In the figure τ_k is the Kolmogorov time scale and τ_p is the particle relaxation time.

So in the conditions of the gasifier considered by Montagnaro & Salatino (2009) (average mass particle concentration $\alpha_0 = 0.05$ in the *lean* phase and $\rho_p/\rho_f = 2500$) it is possible to assume that it is necessary to consider the two-way coupling between particle and fluid phases.

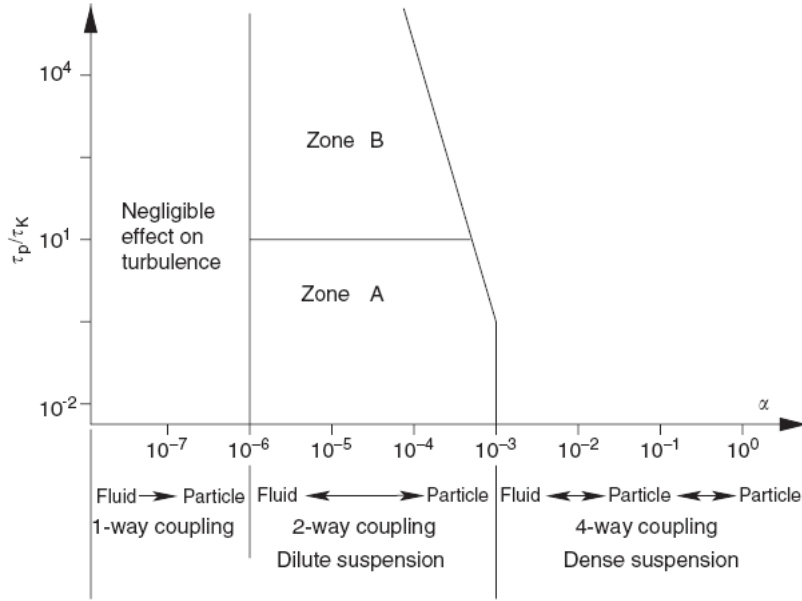


Figure 3.2: Classification map of dispersed two-phase flows (from Elghobashi, 2006).

3.1.2 Particle motion in fluids

The motion of particles in fluids is described in a Lagrangian way by solving a set of ordinary differential equations along the trajectory in order to calculate the changes of particle position and of the particle velocity (linear and angular components). This requires, in general, the consideration of all relevant forces acting on the particle. The equation of motion for small particles in a viscous quiescent fluid (i.e. for small particle Reynolds-numbers, which is also referred to as Stokes flow) goes back to the pioneering work made by Basset in 1888, Boussinesq in 1885 and Oseen in 1927 as shown in Sommerfeld (2000). Therefore, the equation of motion is mostly referred to as BBO-equation.

Considering spherical particles and neglecting mass transfer and heat phenomena, the calculation of particle trajectories requires the solution of three ordinary differential equations (when particle rotation is accounted for). Hence, the differential equations for calculating the particle location, and the linear and angular velocities in vector form are given by:

$$\frac{d\mathbf{x}_p}{dt} = \mathbf{u}_p \quad (3.1)$$

$$m_p \frac{d\mathbf{u}_p}{dt} = \sum \mathbf{F}_i \quad (3.2)$$

$$I_p \frac{d\boldsymbol{\omega}_p}{dt} = \mathbf{T} \quad (3.3)$$

where m_p is the particle mass, I_p is the moment of inertia for a sphere, \mathbf{F}_i represents the different relevant forces acting on the particle, and \mathbf{T} is the torque acting on a rotating particle due to the viscous interaction with the fluid. Analytical solutions for the different forces and the torque only are available for small particle Reynolds numbers (i.e. Stokes regime). An extension to higher Reynolds numbers is generally based on empirical correlations which are derived from experiments or direct numerical simulations (Sommerfeld, 2000).

Drag force

In most fluid-particle systems the drag force is dominating the particle motion and consists of a friction and form drag. The extension of the drag force to higher particle Reynolds numbers is based on the introduction of a drag coefficient C_D being defined as:

$$C_D = \frac{F_D}{\rho_F/2 (\mathbf{u}_F - \mathbf{u}_p)^2 A_p} \quad (3.4)$$

where A_p is the cross-section of a spherical particle. The drag force is then expressed by:

$$\mathbf{F}_D = \frac{3}{4} \frac{\rho_F}{\rho_p} \frac{m_p}{D_p} C_D (\mathbf{u}_F - \mathbf{u}_p) |\mathbf{u}_F - \mathbf{u}_p| \quad (3.5)$$

The drag coefficient is given as a function of the particle Reynolds number:

$$Re_p = \frac{\rho_F D_p |\mathbf{u}_F - \mathbf{u}_p|}{\mu_F} \quad (3.6)$$

The dependence of the drag coefficient of a sphere (spherical particle) on the Reynolds number is shown in Figure 3.3 based on numerous experimental

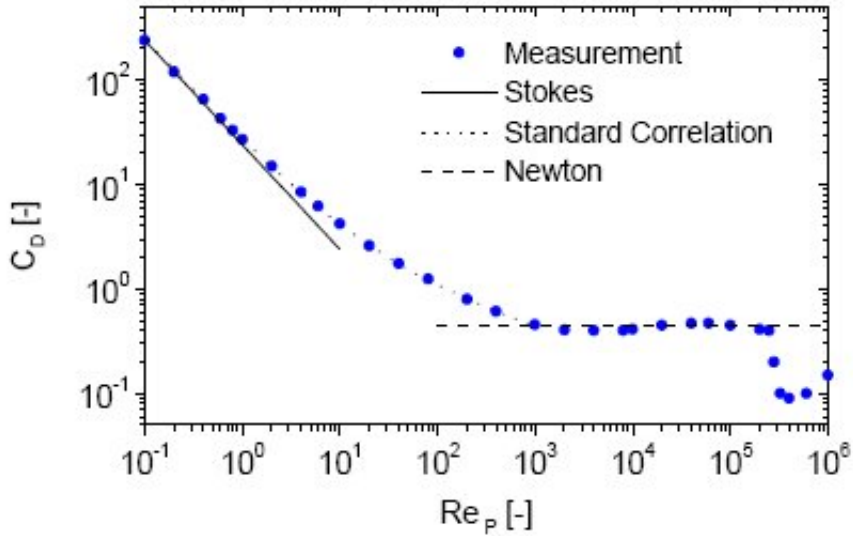


Figure 3.3: Drag coefficient as a function of particle Reynolds number (from Sommerfeld, 2000).

investigations Sommerfeld (2000). One may identify several regimes which are associated with the flow characteristics around the sphere.

The drag coefficient may be altered by numerous other physical effects, such as turbulence of the flow, surface roughness of the particle, particle shape, wall effects, compressibility of the fluid, rarefaction effects, which in general can be accounted for by empirical correction factors or functions being derived from detailed experiments (Sommerfeld, 2000; Guha, 2008). The expression used in this study is the Eq. (4.26), all secondary effects on drag force are neglected.

Pressure gradient and buoyancy force

The local pressure gradient in the flow gives rise to an additional force in the direction of the pressure gradient. From the Navier-Stokes equation of the fluid the pressure gradient and the shear stress can be related to the fluid acceleration and the gravity force (Sommerfeld, 2000). Hence the total pressure force is obtained in the following form:

$$\mathbf{F}_p = m_p \frac{\rho_F}{\rho_p} \left(\frac{D\mathbf{u}_F}{Dt} - \mathbf{g} \right) \quad (3.7)$$

The first term of Eq. (3.7) represents the fluid acceleration (material derivative) and the second one is the buoyancy force. In this study the fluid accel-

eration term has been neglected and the buoyancy force is taken in account only on configurations in which gravity has also been.

Added mass and Basset force

When a dispersed particle accelerates/decelerates relative to the fluid phase, a certain fraction of the surrounding fluid is also accelerated/decelerated; this is the so-called added mass because has the effect of an added inertia.

The Basset force is caused by the lagging of the boundary layer development on the particle with changing relative velocity (i.e. acceleration or deceleration of the particle) and is often referred to as *history* force.

Both forces are neglected in this study because generally their magnitude is smaller of the drag force (Ranade, 2002).

Body forces

Body forces in this study are represented only by the the gravity force. Particles are not moving in such electric field and also the thermophoretic force, which becomes of importance when a small particle moves in a flow with a high temperature gradient, has not been taken in account.

Slip-shear and slip-rotation lift force

Particles moving in a shear layer experience a transverse lift force due to the non-uniform relative velocity (or vorticity) over the particle and the resulting non-uniform pressure distribution. The lift force is acting towards the direction of higher slip velocity (Sommerfeld, 2000). In this study the effect of the slip-shear lift force has been neglected.

Particles which are not freely rotating in a flow may also experience a lift force due to their rotation, the so-called Magnus force. The rotation of the particle results in a deformation of the flow field around the particle, associated with a shift of the stagnation points and a transverse lift force Sommerfeld (2000). In this study particles are considered not rotating so this force, that typically have magnitude smaller of the drag force, has been neglected.

Response time and Stokes number

The particle (velocity or momentum) response time may be used to characterize the capability of particles to follow a sudden velocity change in the

flow (Sommerfeld, 2000). The equation of motion becomes

$$\frac{d\mathbf{u}_p}{dt} = \frac{1}{\tau_p} (\mathbf{u}_F - \mathbf{u}_p) \quad (3.8)$$

where τ_p has the dimension of a time, the particle response time:

$$\tau_p = \frac{\rho_p D_p^2}{18 \mu_F f_D} \quad (3.9)$$

and f_D is $C_D Re_p/24$. The solution of this equation for a simplified case with constant fluid velocity \mathbf{u}_F and zero initial particle velocity ($\mathbf{u}_p = 0$ at $t=0$) is

$$\mathbf{u}_p(t) = \mathbf{u}_F \left[\frac{1}{\tau_p} (1 - e^{-t/\tau_p}) \right] \quad (3.10)$$

From this equation τ_p is the time required for a particle released with zero velocity into a flow with uniform \mathbf{u}_F to reach 63.2 % of the flow velocity (Sommerfeld, 2000).

The Stokes number is the ratio of the particle response time to a characteristic time scale of the flow τ_F .

$$St = \frac{\tau_p}{\tau_F} \quad (3.11)$$

The fluid time scale τ_F can be related, in a turbulent flow field, to the time scale of the energetic eddies. In this study, in the channel configurations described in section 5.4.1, it has been considered the viscous time scale of the fluid $\tau_F = \nu/u_\tau^2$.

3.2 Modeling of particle-wall and particle-particle interaction

3.2.1 Particle-wall interactions

A deeper overview is devoted to this part of the phenomenology, as it will be the focus of this PhD research work. Indeed, the effects of the presence of a viscous slag layer on the wall and on the formation of the segregated carbon regime in particular, as discussed previously in section 1.2.1, will be modeled. This is devoted to obtain, for example, an accurate particle deposition rate on the slag.

From the classical point of view of the mean flow properties, particle-wall collisions become of importance in confined flows. In general there is

a momentum loss of a particle caused by an inelastic wall impact. This pressure loss depends on the average wall collision frequency that is mainly determined by particle mass loading, dimensions of the confinement, particle response time or response distance, particle shape, wall roughness and particular particle and wall material (Sommerfeld, 2000). A first estimate of the importance of particle-wall collisions may be based on the ratio of the particle response distance λ_p to the dimension of the confinement, e.g. the diameter of a pipe D or the height of a channel H . The particle response distance can be estimated from $\lambda_p = \tau_p \cdot w_t$ where w_t is the terminal velocity of the particle Sommerfeld (2000). For the case λ_p is larger than the dimension of the confinement (D or H), the particles do not have enough time to respond to the flow before they collide with the opposite wall; in this case particle motion is dominated by wall collisions.

Moreover the wall collision process may be affected by hydrodynamic interaction which eventually causes a deceleration of the particle before impact. In fact the motion of particles in the vicinity of a rigid wall results in an increase of the drag coefficient and is additionally associated with a transverse lift force.

From the point of view of particle-laden flows inside a gasifier, the attention is fully devoted to the deposition rate of coal particles on the soft boundary formed by the slag. In this case the number λ_p/D is not significant and others parameters have to be considered to characterize the phenomenology.

In the literature, there are two different approach to model the particle-wall collision (Ranade, 2002):

- the hard-sphere model
- the soft-sphere model.

In the so called hard-sphere model the collision is described with negligible particle deformation. In fact particles are assumed to interact through instantaneous binary collisions. This means particle interaction times are much smaller than the free flight time. In the soft-sphere approach, particles are allowed to overlap slightly. The contact forces are then calculated from the deformation history of the contact. In the-hard sphere approach the type of collision is determined by the static coefficient of friction μ_0 , the restitution ratio of the normal velocity components, ϵ , and the velocity of the particle surface relative to the contact point.

In general, the effect of a wall is to retard the motion of particles in both the parallel and the normal direction to the wall, thus reducing the rate of mass transport. As was mentioned previously, indeed, the lift on small

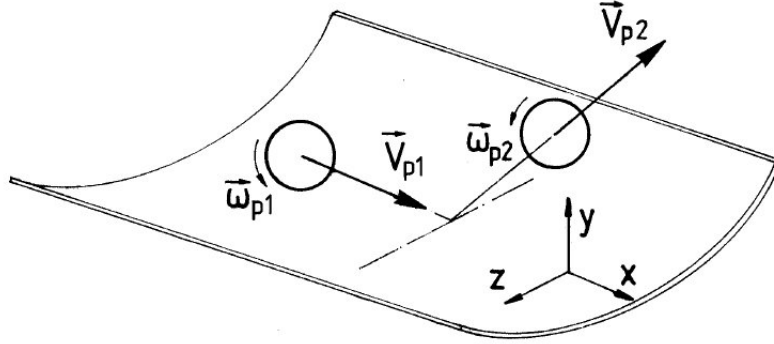


Figure 3.4: Configuration of a particle-wall collision (from Sommerfeld, 2000).

particles, which is induced by the shear layer close to any wall, is acting towards the direction of higher slip velocity, hence like a repulsive effect of the wall Crowe & Michaelides (2006).

As will be illustrated in the next chapter, in this study the particle-wall collision has been modeled with a hard-sphere approach; several restitution ratios of the velocity are considered to simulate the effect of the slag viscous layer that covers the walls of an entrained-flow gasifier.

3.2.2 Inter-particle collisions

Inter-particle collisions may have several consequences in particle-laden flows, such as heat and momentum transfer between particles, dispersion of regions with locally high particle concentration, and eventually also agglomeration of particles. The inter-particle collision probability depends mainly on the particle concentration, the particle size, and the fluctuating motion of the particles (Sommerfeld, 2000).

In dilute two-phase flows the particle motion will be mainly governed by fluid dynamic transport effects, i.e. drag force, and turbulence. Dense flows are characterized by high collision frequencies between particles and hence their motion is very influenced by inter-particle collisions.

In this study the inter-particle collision has not been modeled. All the configurations studied are in such nominal conditions of particle concentration that has been considered valid the hypothesis of dilute systems at the initial phase. However, the possibility of the formation of agglomerates of particles, starting from a dilute system, has been verified so the validity of the results discussed is limited by this strong assumption.

Chapter 4

Numerical modeling

As was anticipated in the introductory chapter, numerical modeling has been mainly adopted in this study. In this chapter the numerical models, upon which the multilevel approach is based on, will be illustrated; OpenFOAM, the numerical code adopted for simulating the physics involved in the study will be presented, and the ways in which necessary models are been implemented such as multiphase approach and coupling, turbulence modeling and Lagrangian particle tracking will be described. In appendix A some useful pieces of code, written for the OpenFOAM version 1.6.x, are reported. Furthermore some information about the computing platform used for carrying out numerical simulations are shown, with particular regard to the characteristics of parallel computing code.

4.1 OpenFOAM: an open source CFD toolbox

The OpenFOAM (Open Field Operation and Manipulation) CFD Toolbox is a free, open source CFD software package produced by a commercial company, OpenCFD Ltd. It has a large user base across most areas of engineering and science, from both commercial and academic organizations. OpenFOAM has an extensive range of features to solve anything from complex fluid flows involving chemical reactions, turbulence and heat transfer, to solid dynamics and electromagnetics.

The core technology of OpenFOAM is a flexible set of efficient C++ modules. These are used to build a wealth of: solvers, to simulate specific problems in engineering mechanics; utilities, to perform pre- and post-processing tasks ranging from simple data manipulations to visualization and mesh processing; libraries, to create toolboxes that are accessible to the solvers/utilities, such as libraries of physical models.

OpenFOAM uses finite volume numerics to solve systems of partial differential equations ascribed on any 3D unstructured mesh of polyhedral cells. The fluid flow solvers are developed within a robust, implicit, pressure-velocity, iterative solution framework, although alternative techniques are applied to other continuum mechanics solvers. Domain decomposition parallelism is fundamental to the design of OpenFOAM and integrated at a low level so that solvers can generally be developed without the need for any *parallel-specific* coding (OpenCFD, last visited October 2011).

The numerical meshes are built, when possible, by using software provided by the OpenFOAM package like the *blockMesh* utility: this utility is useful to build a structured mesh starting from an assigned geometry described in a text file and it is adequate in the case of not complicated geometries. The numerical simulations are computed by a solver specifically developed to solve the unsteady solutions of the gas and particle phases. The code is arranged to integrate the solution of both phases and their coupling and it has been written starting from tutorials and advices provided by the community.

4.2 Euler-Lagrangian approach

As mentioned in chapter 2, the Euler-Lagrangian approach for gas and particle phases respectively is a good compromise to model the particle dispersion in gas considering the need of a very big computational power. In a Large Eddy Simulation (LES) approach, turbophoresis effects of the fluid phase on particle motion, especially close to the confining walls, are very sensitive to the dimension of the resolved scales. Therefore, to model correctly the particle-wall interaction phenomena there is the need of a good resolution of the mesh size near the wall and an appropriate turbulence model. Direct Numerical Simulations (DNS) for the fluid phase are too computational expensive for industrial geometries and, on the other hand, Reynolds Averaged Simulations (RAS) can't get the effect of physical turbulent eddies on the particle motion.

Simulations are involving a lot of particles, from 10^5 to 10^6 particles. With a Lagrangian approach, every single particle is tracked. A good and proper choice of the computational mesh is required to meet the constraint that particle diameter should be smaller than the dimension of the computational cell. This constraint cannot be met everywhere in the domain for the characteristic size scales involved in the modeling of coal and ash particles evolving into a turbulent environment. As it will be described, this causes some computational difficulties that require special consideration and care.

4.2.1 Continuous phase

The continuous phase is considered to be air. A thermophysical model is constructed in OpenFOAM as a pressure-temperature $p - T$ system from which other properties are computed. The adopted thermophysical model consider the gas as a perfect gas. The specific heat coefficient c_p is constant and computed from enthalpy h and entropy S while the *ThermoModel* adopted is the general thermophysical model based on enthalpy h and compressibility ψ . The Navier-Stokes (NS) equations are obtained applying the conservation laws of mass and momentum at the fluid volume (and numerically at every finite control volume produced by the discretization). In general, gaseous flows may be considered to behave essentially as incompressible flows when $M < 0.3$ and compressible when $M > 0.3$. For an unsteady compressible flows the NS equations are:

$$\frac{\partial \rho}{\partial t} + \nabla \cdot \rho \mathbf{U} = 0 \quad (4.1)$$

$$\frac{\partial}{\partial t} \rho \mathbf{U} + \nabla \cdot (\rho \mathbf{U} \mathbf{U}) = -\nabla p + \nabla \cdot \boldsymbol{\sigma} + \mathbf{M} \quad (4.2)$$

$$\frac{\partial}{\partial t} \rho h + \nabla \cdot (\rho \mathbf{U} h) = \frac{Dp}{Dt} + \nabla \cdot \lambda \nabla T + \boldsymbol{\sigma} \cdot \nabla \mathbf{U} \quad (4.3)$$

where \mathbf{U} is the fluid velocity vector field, ρ is the gas density, p is the gas pressure, $\boldsymbol{\sigma}$ is the viscous stress tensor and $\mathbf{M} = \mathbf{M}(x, y, z, t)$ represents momentum sources in the flow field, h the enthalpy, T the temperature of the fluid. When the fluid flow field is considered to be dependent of the dispersed phase then the term \mathbf{M} will consider this coupling; in other words that term will consider the influence of the particles on the fluid (in one-way coupling of course this influence is null because the fluid phase is not affected by the dispersed phase). If the gravity is considered, in one-way coupling it is the only body force acting on the fluid flow then the momentum source term is

$$\mathbf{M} = \rho \mathbf{g}$$

In two-way coupling, the term \mathbf{M} will consider the forces that particles exert on the flow field. See section 4.2.3 for further details.

The viscous stress tensor is defined as

$$\boldsymbol{\sigma} = \mu(T) \left[\nabla \mathbf{u} + (\nabla \mathbf{U})^T \right] - \frac{2}{3} \mu (\nabla \cdot \mathbf{U}) \mathbf{I} \quad (4.4)$$

where μ is the fluid dynamic viscosity.

U-RANS approach

In the first step of the multilevel approach, described in section 5.2, an U-RANS (Unsteady-RANS) method has been applied to describe the motion of the Eulerian gas phase in the gasification chamber investigated by Sommerfeld & Qiu (1993). The char particles migration towards the slag layer is favored by the turbulent motion induced by the swirl applied at the flow domain inlet. Induced flow structures, whose dimensions are of the order of the swirler diameter, possess an unsteady behavior. For this reason, a time-dependent description of their dynamics is preferred to a fully time-averaged approach to investigate the deposition mechanisms.

The U-RANS method is based on a decomposition of the resolved variable among three contributions: a time averaged variable \bar{f} , a conditional average $\langle f \rangle_c$ on time frequencies of the velocity field characteristics of the coherent motions and the random fluctuations f'' (Sagaut, 2001):

$$f(\mathbf{x}, t) = \bar{f}(\mathbf{x}) + \langle f(\mathbf{x}, t) \rangle_c + f''(\mathbf{x}, t)$$

Even if no temperature variations occur in the present case, the model is based on the full compressible formulation aiming at a prompt generalization to variable density flows. According to the compressible formulation, a Favre average is used (Poinso & Veynante, 2001):

$$\tilde{f} = \frac{\overline{\rho f}}{\bar{\rho}} = \frac{\lim_{t^* \rightarrow \infty} \frac{1}{t^*} \int_{t^*} \rho f dt}{\lim_{t^* \rightarrow \infty} \frac{1}{t^*} \int_{t^*} \rho dt}$$

and the following decomposition holds $f = \tilde{f} + f''$ where \tilde{f} contains its conditional average (unsteady contribution) over the time scale t_c characteristic of coherent motion. Since the unsteady component of a U-RANS variable is limited to the time frequency relative to $1/t_c$, the velocity and particle time scales shorter than t_c cannot be described. This implies that a model has to be exploited to account for the short time phenomena like those characteristics of the very fast random motion of particles.

The Favre averaged Navier-Stokes equations take the form:

$$\frac{\partial \bar{\rho}}{\partial t} + \nabla \cdot \bar{\rho} \tilde{\mathbf{U}} = 0 \quad (4.5)$$

$$\frac{\partial}{\partial t} \bar{\rho} \tilde{\mathbf{U}} + \nabla \cdot (\bar{\rho} \tilde{\mathbf{U}} \tilde{\mathbf{U}}) = -\nabla \bar{p} + \nabla \cdot \bar{\boldsymbol{\sigma}} - \nabla \cdot \bar{\rho} \tilde{\mathbf{U}}'' \tilde{\mathbf{U}}'' \quad (4.6)$$

$$\frac{\partial}{\partial t} \bar{\rho} \tilde{h} + \nabla \cdot (\bar{\rho} \tilde{\mathbf{U}} \tilde{h}) = \frac{Dp}{Dt} + \nabla \cdot (\lambda \nabla T - \bar{\rho} \tilde{\mathbf{U}}'' \tilde{h}'') + \bar{\boldsymbol{\sigma}} \cdot \nabla \tilde{\mathbf{U}} \quad (4.7)$$

being:

$$\boldsymbol{\sigma} = 2\mu(T)\mathbf{S} - \frac{2}{3}\mu Tr(\mathbf{S})\mathbf{I} \quad (4.8)$$

the deviatoric of the shear stress tensor and \mathbf{S} the strain tensor. The unclosed terms in Favre averaged momentum and enthalpy equations are: the Reynolds stresses $-\bar{\rho}\widetilde{\mathbf{U}''\mathbf{U}''}$ and the enthalpy turbulent flux $-\overline{\rho\mathbf{U}''h''}$. They are modeled in terms of the velocity field $\widetilde{\mathbf{U}}$ adopting the Boussinesq hypothesis (Poinsot & Veynante, 2001):

$$-\rho\widetilde{\mathbf{U}''\mathbf{U}''} = 2\mu_t(\widetilde{T})\mathbf{S} - \frac{2}{3}\mu_t(\widetilde{T})Tr(\mathbf{S})\mathbf{I} - \frac{1}{3}Tr(\rho\widetilde{\mathbf{U}''\mathbf{U}''})\mathbf{I} \quad (4.9)$$

$$-\overline{\rho\mathbf{U}''h''} = -\bar{\rho}\alpha_t\nabla\widetilde{T} \quad (4.10)$$

The Eq. (4.5), Eq. (4.6) and Eq. (4.7) are closed adopting the compressible version of the $k-\omega$ SST model (Menter *et al.*, 2003), in which the turbulent viscosity and the thermal diffusivity are respectively:

$$\mu_t = \frac{\rho a_1 k}{\max(a_1\omega, SF_2)}$$

$$\alpha_t = \frac{\mu_t}{\bar{\rho}Pr_t}$$

where values of k and ω are derived by solving proper transport equations for these two variables.

Information about OpenFOAM implementation of turbulence U-RANS modeling adopted are given in section A.1.1.

LES approach

In the second step of the multilevel procedure described in section 5.4, a Large Eddy Simulation (LES) method is applied to solve the model equations of the Eulerian continuous phase. For density variable flows the Favre filter:

$$\bar{\rho}\tilde{f} = \int \rho f(\mathbf{x}', t) G(\mathbf{x} - \mathbf{x}'; \bar{\Delta}) d\mathbf{x}'$$

is usually adopted (Garnier *et al.*, 2009), where G is the filter function and $\bar{\Delta} = (\Delta_1\Delta_2\Delta_3)^{1/3}$ the filter width kept equal to the control volume measure. As in FV methods, the balance equations are discretized starting from the integral counterparts. Thus, being the volume averaged variable equivalent

to the top hat LES filter if a uniform filter width is adopted, the following formal equivalence, for a property f , holds on uniform grids:

$$\bar{f}(\mathbf{x}', t) = \frac{1}{\Delta} \int f(\mathbf{x}', t) d\mathbf{x}'$$

Thus the OpenFOAM equations can be interpreted as the evolution equations for the filtered variables. The compressible filtered equations take the form (Garnier *et al.*, 2009):

$$\frac{\partial \bar{\rho}}{\partial t} + \nabla \cdot \bar{\rho} \tilde{\mathbf{U}} = 0 \quad (4.11)$$

$$\frac{\partial \bar{\rho} \tilde{\mathbf{U}}}{\partial t} + \nabla \cdot \bar{\rho} \tilde{\mathbf{U}} \tilde{\mathbf{U}} = -\nabla \bar{p} - \frac{\Delta p}{L_x} \mathbf{i}_x + \nabla \cdot \hat{\boldsymbol{\sigma}} - \nabla \cdot \boldsymbol{\tau} + \nabla \cdot (\bar{\boldsymbol{\sigma}} - \hat{\boldsymbol{\sigma}}) \quad (4.12)$$

$$\begin{aligned} \frac{\partial \bar{\rho} \tilde{h}}{\partial t} + \nabla \cdot \bar{\rho} \tilde{h} \tilde{\mathbf{U}} &= \frac{\partial \bar{p}}{\partial t} + \tilde{\mathbf{U}} \cdot \nabla \bar{p} - \frac{\Delta p}{L_x} \mathbf{i}_x \cdot \tilde{\mathbf{U}} - \nabla \cdot \hat{\mathbf{q}} - \hat{\Phi} \\ &- [\nabla \cdot (C_v \mathbf{Q}) + \Pi_{dil} - \epsilon_\nu + \nabla \cdot (\bar{\mathbf{q}} - \hat{\mathbf{q}})] \end{aligned} \quad (4.13)$$

being:

$$\hat{\Phi} = \hat{\boldsymbol{\sigma}} : \nabla \tilde{\mathbf{U}} \quad (4.14)$$

$$\hat{\boldsymbol{\sigma}} = 2\mu(\tilde{T}) \tilde{\mathbf{S}} - \frac{2}{3}\mu(\tilde{T}) Tr(\tilde{\mathbf{S}}) \mathbf{I} \quad (4.15)$$

$$\hat{\mathbf{q}} = -\lambda(\tilde{T}) \nabla \tilde{T} \quad (4.16)$$

and \mathbf{i}_x the direction along which the forcing pressure is applied to determine the flow motion.

The resulting SGS terms present in the Eqs. (4.11)–(4.13) are the momentum flux, the temperature flux, the pressure dilatation and the viscous dissipation, respectively given by:

$$\boldsymbol{\tau} = \bar{\rho} (\widetilde{\mathbf{U}\mathbf{U}} - \tilde{\mathbf{U}}\tilde{\mathbf{U}}) \quad (4.17)$$

$$\mathbf{Q} = \bar{\rho} (\widetilde{\mathbf{U}T} - \tilde{\mathbf{U}}\tilde{T}) \quad (4.18)$$

$$\Pi_{dil} = \overline{p \nabla \cdot \mathbf{U}} - \bar{p} \nabla \cdot \tilde{\mathbf{U}} \quad (4.19)$$

According to the a priori evaluation made by Vreman *et al.* (1996), the SGS term $\nabla \cdot (\overline{\boldsymbol{\sigma}} - \widehat{\boldsymbol{\sigma}})$ can be neglected, being the turbulent Mach number for all cases here considered much less than 1. Using the change of variable proposed by Comte and Lesieur (Garnier *et al.*, 2009), and introducing the modified pressure $\bar{p} + 1/3 Tr(\boldsymbol{\tau})$, $\boldsymbol{\tau}$ can be replaced in the Eq. (4.12) by its deviatoric part $\boldsymbol{\tau}^d$ which is modeled according to an eddy viscosity assumption:

$$\boldsymbol{\tau} - \frac{1}{3} Tr(\boldsymbol{\tau}) \mathbf{I} = \boldsymbol{\tau}^d = -2\mu_t \left(\tilde{S} - \frac{1}{3} Tr(\tilde{S}) \mathbf{I} \right) \quad (4.20)$$

The built-in OpenFOAM compressible version of localized dynamic model LDKM developed by Kim *et al.* (1999) is adopted to compute μ_t . According to such formulation, the subgrid viscosity is given by $\mu_t = C_k \bar{\rho} (k_{sgs})^{1/2} \Delta$. The subgrid turbulent kinetic energy k_{sgs} is computed through the solution of the transport equation:

$$\frac{\partial \bar{\rho} k_{sgs}}{\partial t} + \nabla \cdot (\bar{\rho} \tilde{\mathbf{U}} k_{sgs}) = P_{sgs} - D_{sgs} + \nabla \cdot \left(\frac{\mu_t}{Pr_t} \nabla k_{sgs} \right) \quad (4.21)$$

where Pr_t is the turbulent Prandtl number. The production and dissipation terms are expressed with the assumptions $P_{sgs} = -\boldsymbol{\tau} : \nabla \tilde{\mathbf{U}}$ and $D_{sgs} = C_\epsilon \bar{\rho} (k_{sgs})^{3/2} / \Delta$ respectively. In the LDKM formulation C_ϵ and C_k are evaluated according a dynamic-based procedure (Germano *et al.*, 1991).

Thus the model is supposed to tune the effects of the sub-grid scales on the resolved field during the computation. Such feature overcomes the limitations based on the assumption of local equilibrium of energy transfer between the scales separated by the filter cut off at which Smagorinsky eddy viscosity closure is defined.

The implementation in OpenFOAM, called *dynOneEqEddy* (OpenCFD, 2008), adopts an average procedure over the entire flow domain to determine the constants C_ϵ and C_k . Hence, the sub-grid turbulent viscosity has a unique value over the entire flow domain which change at each time step. Such limitation has to be accounted for to evaluating the total amount of the sub-grid dissipation. However, being the computations here presented relative to small domains with an almost homogeneous and in equilibrium flow conditions, this limitation is expected to not affect too much the results.

According to the works of Martin *et al.* (2000), the SGS term ϵ_ν appearing in the enthalpy equation can be considered an order of magnitude smaller than the corresponding divergence of the SGS heat fluxes, while the SGS term $\nabla \cdot (\bar{\mathbf{q}} - \widehat{\mathbf{q}})$ can be neglected. Following the proposal reported in Moin *et al.* (1991) it is possible to neglect also the term Π_{dil} . Adopting these

assumptions, only an SGS model for the heat flux is needed to close the enthalpy equation:

$$\mathbf{Q} = -\frac{\mu_t}{Pr_t} \nabla \tilde{T} \quad (4.22)$$

being Pr_{sgs} the SGS Prandtl number.

Further details about the OpenFOAM implementation of turbulence LES modeling adopted are described in appendix A.1.1.

Continuous phase statistics

To obtain the fluid properties of the continuous phase from unsteady state calculation of the flow fields simulations, data have to be collected from results and then proper statistics need to be computed. These statistics are obtained by averaging the fluid properties at different times once the simulation has reached a statistical convergence in the fluid phase. A parameter adopted to evaluate this convergence (in a statistical meaning) has been the total specific kinematic energy of the flow field defined by Eq. (4.23):

$$E = \frac{1}{2V} \sum_i \rho_i (\mathbf{u}_i)^2 \quad (4.23)$$

where subscript i denotes cell values, V is the total volume of the domain and the summation is extended to the overall computational domain.

Another way to make averaged values is averaging in space when the geometry of the configuration is suitable (for example in the periodic planar and curved channel flow configurations).

4.2.2 Particle phase

The trajectory of the particles are computed solving the equations of motion (Eq. (3.1))-(Eq. (3.3)). Particles are supposed to be spherical and rigid and non rotating so Eq. (3.3) is not considered. Being the ratio of particles density over fluid density very large (order 10^3), it is possible to neglect the added mass, Basset (history effect), Magnus (rotation of the particle), Saffman (slip-shear lift force), pressure and buoyancy components of the force acting on the particle. So the Basset-Boussinesq-Oseen (BBO) equation can be reduced to the equation of motion for a point-particle Crowe & Michaelides (2006), that only considers the drag and gravitational force ($\sum \mathbf{F} = \mathbf{F}_D + \mathbf{F}_P$):

$$\frac{d\mathbf{x}_p}{dt} = \mathbf{u}_p \quad (4.24)$$

$$\frac{d\mathbf{u}_p}{dt} = \frac{3}{4} \frac{\rho_F}{d_p} \frac{C_D}{\rho_p} (\mathbf{u} - \mathbf{u}_p) |\mathbf{u} - \mathbf{u}_p| + \left(1 - \frac{\rho_F}{\rho_p}\right) \mathbf{g} \quad (4.25)$$

For the drag force, the considered relation between the drag coefficient C_D and the Reynolds particle number is

$$C_D = \begin{cases} \frac{24}{Re_p} & Re_p \leq 0.1 & \text{(Stokes regime)} \\ \frac{24}{Re_p} \left(1 + \frac{1}{6} Re_p^{2/3}\right) & 0.1 \leq Re_p \leq 1000 & \text{(Transition regime)} \\ 0.44 & Re_p > 1000 & \text{(Newtonian regime)} \end{cases} \quad (4.26)$$

where Re_p is the particle Reynolds number, defined as

$$Re_p = d_p |\mathbf{u}_p - \mathbf{u}| / \nu \quad (4.27)$$

in which d_p is the particle diameter, \mathbf{u}_p is particle velocity, \mathbf{u} is fluid velocity at particle position and ν is the cinematic viscosity of the fluid. The Eq. (4.26) is a fast and good approximation of the correlation proposed by Shiller and Naumann (1935). With this assumption are not taken in account other physical effects, such as surface roughness of the particle, particle shape, wall effects, compressibility of the fluid, rarefaction and so on, that may alter the drag coefficient (Crowe, 2006).

Particle phase statistics

Simulations involve a very large number of particles, each of them tracked by the Lagrangian Particle Tracking algorithm (LPT). Statistics are obtained averaging particle properties on a big number of particles, all of them grouped by their position in the computational domain. Typically, particles are grouped by decomposing the physical domain in layers at different distance from the bounding walls. Thickness of each layer have to hold a number of particles big enough to provide a statistical meaning of the averaged characteristics such as velocity of the particles and so on.

Particle concentration α_i is defined for each computational cell and is the ratio between the mass of the particles in the cell and the mass of the fluid assuming it being in the overall cell. The following expression defines α_i :

$$\alpha_i = \frac{\pi}{6\rho_f V} \sum_i \rho_{pi} d_{pi}^3 \quad (4.28)$$

where the summation is extended to all particles in the considered computational cell so the subscript pi denotes particle values, V is the volume of the

cell and ρ_f is fluid density. A useful dimensionless parameter is the ratio between α_i computed at time T and α_0 computed at injection time which has a quasi-uniform distribution being particles of the same density and randomly injected.

4.2.3 Phases coupling

According with the definitions given in section 3.1.1, here is shown how OpenFOAM manage the various levels of coupling between continuous and dispersed phases. Particles motion is computed by the Lagrangian Particle Tracking that, for each time step, calculates the final position of the particle starting from the initial position and considering the forces that are acting on. The one-way coupling corresponds to considering no interaction between particles and the fluid flow field; This is implemented solving the Navier-Stokes equations without any source term contribution due to the presence of particles so $\mathbf{M} = \mathbf{0}$ in Eq. (4.2).

When the fluid flow field is considered to be dependent on the effect of the dispersed phase, two-way coupling has to be implemented. Let consider a particle P of mass m_P and velocity \mathbf{u}_P . The force exerted by a particle on a unit volume of fluid is proportional to the difference in particle momentum between the instant it enters (t_{in}) and leaves (t_{out}) the control volume:

$$-m_P ((\mathbf{u}_P)_{t_{out}} - (\mathbf{u}_P)_{t_{in}})$$

That force is generated in each cell visited by the particle P along its path during one Eulerian time step. The contribution \mathbf{M}_k to the momentum source in Eq. (4.2) of all the particles which have been in the cell k (of volume V_k) during the Eulerian time step dt is written as

$$\mathbf{M}_k = -\frac{1}{V_k dt} \sum_P m_P ((\mathbf{u}_P)_{t_{outcellk}} - (\mathbf{u}_P)_{t_{incellk}}) \quad (4.29)$$

As it is described in section 4.3, the particle tracking algorithm used is able to compute the portion of the time step dt particles spent in each computational cell they are in.

The four-way coupling is usually implemented through a inter-particle collision model. In this study it has not been implemented in the LPT used to solve the particle motion.

4.3 Lagrangian Particle Tracking

The approach used to solve the equation of motion Eq. (3.1)-Eq. (3.3) is the Lagrangian Particle Tracking (LPT). Since the number of particles quite

easily exceeds the computational tracking capabilities when real configurations are of interest, typically a group of physical particles is represented by a computational unit called *parcel*. So a parcel is a computational particle. The physical particles inside a parcel are assumed to have the same position, diameter, velocity, temperature and other properties. The concept of parcel is useful when the size of the particles are very small compared to the computational cell sizes. Indeed the parcel dimension must be smaller of the computational cell size. Particles in the parcel are not supposed to interact each other, at least in the formulation provided in OpenFOAM.

In all simulations presented in this work, each parcel is tracked independently. Large Eddy Simulations, described in section 5.4, are coupled with the particle phase in which each parcel represent only one particle so, for that level of simulation, each particle is really tracked. In the previous level, the U-RANS level described in section 5.2, for computational economy, particles are grouped so each parcel represents 10 or 100 particles of coal. Particles are assumed to be hard spheres and the drag coefficient is assumed to be function of Reynolds particle number as shown in Eq. (4.26).

The algorithm implemented in OpenFOAM for the LPT is described in Macpherson *et al.* (2009) and is named the *TrackToFace* method. That method is able to track the motion of particles in complex 3D geometries, generated from CAD models and meshed with unstructured polyhedra, which may be deforming, in motion or spatially decomposed for parallel computation. The algorithm is designed to be computationally efficient and robust. It can be applied to a wide range of engineering problems ranging from injected fuel sprays in internal combustion engines to molecular dynamics modeling of nanoscale flows. The TrackToFace method practically consists of moving the particle between the faces it crosses in the time step duration. In Figure 4.1 is shown an example of motion of a particle during a single time step. The particle moves from position A to position B through the points P1, P2 and P3 situated on cell faces.

For each particle, fluid properties (such as its velocity), known from the computation as average values in the cell, are interpolated at particle position. Forces acting on the particle are then here computed and, applying the equation of particle motion, the final position of the particle at the end of time step is obtained. Doing this a virtual displacement vector is computed. The particle is moved only for a fraction of the time step that bring it on the first face crossed. At that face position new fluid fields interpolation is done, then new forces acting on the particle are computed as well as the new virtual displacement vector related to the remaining time step duration. The process is stopped at the end of the time step duration and the particle is, in general, in a position inside a cell and not on face anymore.

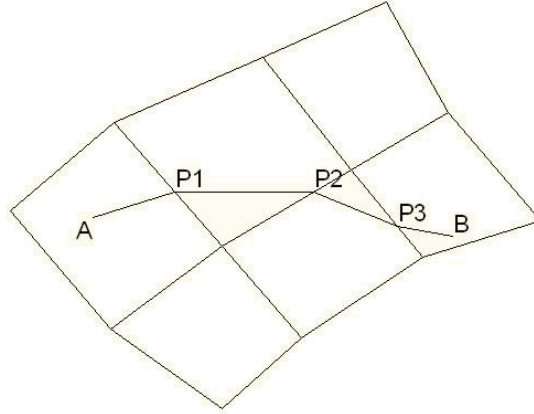


Figure 4.1: Example of *tracktoface* motion of a particle during a single time step

This method is useful also to compute the coupling source term described in Eq. (4.29), being known how much time a particle spends in each cell it crosses and the momentum exchange on crossed faces.

The algorithm is parallelized by the fluid phase domain decomposition so, each parallel computational unit performs the calculation of the particles that are in the corresponding domain at the beginning of the time step.

4.3.1 Wall interaction

When the virtual displacement vector, computed in the LPT algorithm, crosses a face of a wall boundary then it is applied the wall collision model. Precisely the collision occurs when the displacement vector passes through the projection of the wall face shifted, in the wall-normal direction and inside the domain, by the length of the particle radius. This is due because the collision must be occurs when the particle surface touch the wall and not its center and the displacement vector is related to the center of the particle.

When a particle radius (that is the distance from the particle position represented by its center and the actual particle surface) is bigger then the height of the mesh cell closer to the wall, the collision model goes wrong because the collision should happen when the particle (its center) is in an interior mesh cell and not in a boundary one. The author has proposed and implemented a correction that have the aim of simulate a correct wall rebound of particles bigger then the height of the wall boundary mesh cells. In appendix A.2 is shown the effect of the correction but, for the sake of

brevity, it has not been described in this thesis.

Being u_p and u'_p the velocities of the particle P before and after the wall collision and \mathbf{n} and \mathbf{t} respectively the unit vector normal and tangential to the wall, it is possible to write

$$\mathbf{u}_p = u_p^n \cdot \mathbf{n} + u_p^t \cdot \mathbf{t} \quad (4.30)$$

$$\mathbf{u}'_p = u_p'^n \cdot \mathbf{n} + u_p'^t \cdot \mathbf{t} \quad (4.31)$$

The normal component of the particle velocity after a collision with the wall is evaluated as

$$u_p'^n = -\epsilon \cdot u_p^n \quad (4.32)$$

where $\epsilon \in [0, 1]$ is the coefficient of normal restitution of the wall. The tangential component of the velocity will decrease after the collision with the wall

$$u_p'^t = (1 - \mu_w) \cdot u_p^t \quad (4.33)$$

where $\mu_w \in [0, 1]$ is the coefficient of friction of the wall.

Results shown in the chapter 5 are obtained considering the effect of several values of the normal restitution coefficient and no tangential friction at wall ($\mu_w = 0$). In chapter 6 some very recent results that consider the effect of the tangential friction at wall are shown.

4.4 Parallel computing

As mentioned in section 1.4.1, numerical simulations of models that implement the Euler-Lagrange approach, particularly implementing LES modeling for turbulence combined with LPT for particles, are very computational demanding. To overcome this problem, all the simulations described inherent described numerical models and studied configurations (see chapter 5) are been computed on the high performance computing system *CRESCO* of ENEA (Italian agency for the energy, environment and new technologies) with the code package OpenFOAM.

The OpenFOAM package is able to run in parallel on distributed processors. The method of parallel computing used by OpenFOAM is known as domain decomposition, in which the geometry and associated fields are broken into pieces and allocated to separate processors for solution. The process of parallel computation involves: decomposition of mesh and fields; running the application in parallel; and, post-processing the decomposed case (OpenCFD, last visited October 2011). The parallel running uses the

public domain openMPI implementation of the standard message passing interface (MPI).

The ENEA Cresco HPC system (Bracco *et al.*, 2009) is situated in Portici, Naples (Italy) and is, at the time of writing, the powerful computing facility in the south of Italy (the performance for the CRESCO HPC system has ranked 125 in the June 2008 top500 list). All simulations ran on the second section of the facility that is composed by:

- 256 blades IBM HS21 each supporting dual Xeon Quad-Core Clovertown E5345 processors (2.33GHz, 1333MHz, 8MB L2), 16 GB RAM for total of 2048 cores;
- 56 blades each with dual Intel Xeon Quad-Core Turbo Boost Nehalem E5530 processors (2.40GHz, 8MB L3), 16GB RAM for a total of 448 cores;
- 28 blades each with dual Intel Xeon Quad-Core Turbo Boost Westmere E5620 processors (2.40GHz, 8MB L3), 16GB RAM for a total of 224 cores;

. All nodes are connected with the Infiniband (IB) 4X DDR interconnection; the file system used has been the IBM General Parallel File System (GPFS).

To have an idea of the computational cost of some simulations performed, here are shown some information related to the planar channel configuration, described in section 5.4.1, regarding to the parallel computing aspects. The planar channel consists of about 230000 hexahedral cells; the optimal domain decomposition for the parallel run has been in 96 sub domains. The turbulence model description applied is the LES model described in this chapter, time step duration $dt = 0.0002 s$, one-way coupling model between fluid and particle phases; 8 particle clouds (where a cloud is a collection of Lagrangian particles/parcels), each of them with different properties related to particle size and wall interaction, are been considered in one simulation to reduce the computing time (in fact different particle clouds do not interact each other due to the one-way coupling modeling); each cloud is made by 100000 particles each of them tracked with the LPT algorithm described in this chapter. To compute the flow field and particle motion for a time interval of 1200 seconds were necessary about 650 hours of wall time (that is about a month) of parallel computing.

Chapter 5

Simulations of ash particles-slag interaction: Multilevel approach

5.1 Rationale of the modeling approach

The mechanics of particle-slag interaction depends on several parameters of both fluid and particle phases. As described in section 1.2.1 these parameters can be related to physical and chemical properties of char, ash and slag. The stickness capability between particle and slag depends indeed on the interaction between their unconverted portion of material, therefore depends on their conversion degree and other parameters such as char density, particle diameter and impact velocity, slag viscosity, interfacial particle-slag tension. The simplified approach proposed consider only a subset of these parameters. The particle-wall interaction is modeled with a hard collision model in which particles are characterized only by their size and density (velocity is computed by the simulation). The slag is treated as a non deformable wall with variable elastic behavior in normal direction (in chapter 6 some very recent results that consider the effect of the tangential friction at wall are shown). Particle and fluid velocities are obtained by CFD simulations in order to take into account the effects of fluid dynamic interaction with the wall. These effects, such as turbophoresis and swirled driven motion, can be analyzed and measured separately in a hierarchical sequence of CFD simulations:

- Jet-combustor/Gasifier (RANS-DEM modeling)
- Planar channel flow (LES-DEM modeling)
- Curved channel flow (LES-DEM modeling)

The aim of this study is to demonstrate the possibility to gather information from models developed at different scales and different levels of approximation to numerically investigate the phenomena occurring at very small scales in a gasifier. A particular emphasis is devoted to the char particles-slag interaction, for which a very detailed model, based on the Discrete Element Method (DEM) for the solid phase (Loth *et al.* , 2006) and the Large Eddy Simulation (LES) approach for the gas phase (Sagaut, 2001), has been adopted.

At first level a RANS-DEM CFD model is adopted to provide information about particle velocities and trajectories as they impinge the confining walls covered by the slag. Clouds of parcels representing particles of different size and mass, given distributions of particle diameter with respect to typical char and ash sizes, are introduced in a realistic representation of the gasification chamber also indicated as combustor. At this level, the focus is on the assessment of the distribution of particles in the gasifier, on the identification of the average particles load in the different zones of the gasifier and of their velocity and angle of impact onto the confining surface. Therefore, an approach based on a RANS model for the gas phase and on a Lagrangian Particle Tracking (LPT) algorithm to evaluate the particle motion is considered pertinent.

The second level of approximation addresses the detailed simulation of the particle-wall interaction, performed at comparable conditions, in terms of particle loads, particle size distribution and relative importance between drag and inertial effects, using an accurate LES-DEM (Sagaut, 2001) model. In this model the real particles trajectories are affected by the interaction with an unsteady turbulent field and with the confining surfaces. Properties of these surfaces are varied to take into account the different mechanisms of particle deposition due to the presence of a bare wall, a molten slag, or a slag already covered by a layer of particles. This latter level enables the assessment of the particle deposition regimes that are likely to occur in specific regions of the gasifier under the assigned boundary conditions.

The procedure will be illustrated with reference to a simple configuration proposed by Sommerfeld & Qiu (1993). This configuration provides a kind of benchmark; extensive data have been published on this configuration, both from experimental measurements (Sommerfeld & Qiu, 1993) and numerical investigations with both RANS (Sommerfeld & Qiu, 1993) and LES (Apte *et al.* , 2003) approaches.

The OpenFOAM code is adopted to compute the numerical solutions in the two CFD levels of modeling procedure (see section 4.1 and appendix A for further implementation details).

5.1.1 Discrete element model

Details about the models that are adopted at both levels of the approach will be presented. Both levels have the common features of being based on a CFD Eulerian-Lagrangian approach. The Eulerian gas phase, which is modeled with a RANS approach at level 1 and with a LES approach at level 2, is discussed in the next section. In both levels the Discrete Element Method is adopted for the solid phase, solving the equation of motion for each single parcel (level 1) or particle (level 2) included in the domain, following the LPT method discussed in section 4.3, where the gas phase velocities are those obtained with the RANS and LES approaches, respectively.

Following the same assumption done in section 4.2.2, particle motion is driven by drag force and, but only for the level 1 configuration, by gravity.

One-way and two-way coupling approaches are considered in this work. In the former, the particle phase motion is affected by fluid phase flow conditions while the flow does not feel the presence of the particles. Instead in the two-way coupling approach, also the fluid phase is influenced by the momentum exchange with the particle phase. One-way coupling is considered a valid assumption if the particle volumetric concentration is not too high (dispersed regime). For high concentration values a four-way coupling approach is needed to take into account proper interaction mechanisms (see Figure 3.2). Therefore, the effective structure of the eventually dense but very thin film of solid particles in the dense-dispersed phase (see Figure 1.1) cannot be reproduced, limiting the present analysis to the incipient formation of such a layer.

5.2 U-RANS level

5.2.1 Configuration specification

The prototype gasifier configuration chosen in order to develop and validate the proposed procedure is the one proposed by in Sommerfeld & Qiu (1993). The configuration is reported in Figure 5.1, where all lengths are made dimensionless using the radius $R = 0.032 m$ of the outer wall of the external annular jet as the reference length. Two gas streams are coaxially injected into the main cylindrical chamber. The outer stream feeds gas (with axial and swirl components), while the inner stream feeds gas loaded with particles (axial direction).

The main chamber extends for $L = 0.96 m$, corresponding to 5 times the diameter of the main chamber ($D = 0.192 m$). The mass flow rates of the gas feedings are $G_1 = 9.9 \cdot 10^{-3} kg s^{-1}$ and $G_2 = 38.3 \cdot 10^{-3} kg s^{-1}$ related to the

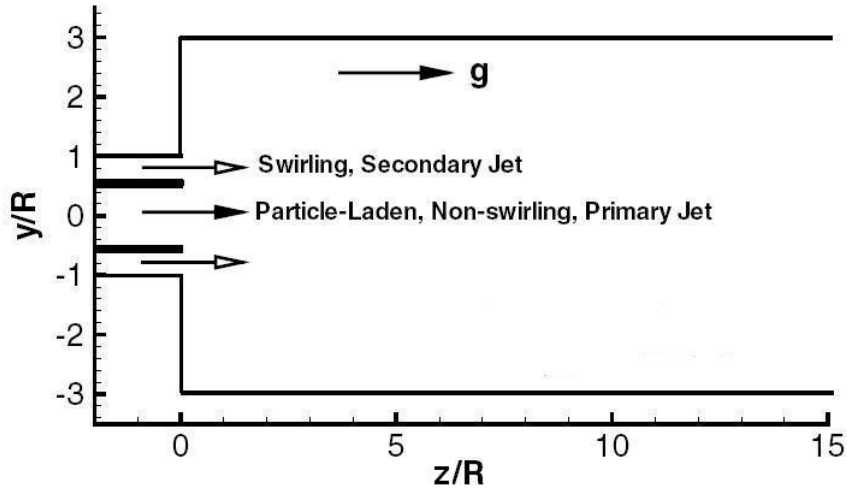


Figure 5.1: 2D sketch of the inlet jets of the combustor; only a portion of the gasifier is reported (from Apte *et al.* , 2003).

central gas jet and the annular swirled gas jet, respectively. The mass flow rate of the solid phase feeding is $G_s = 0.34 \cdot 10^{-3} \text{ kg s}^{-1}$. The swirl number, computed as the ratio of the axial flux of angular momentum to the axial flux of linear momentum, is assumed equal to $S_n = 0.47$ as proposed in the reference case.

Wall functions are applied to turbulent properties and a zero-gradient boundary condition at the outlet (further details are given in A.1.1). The inlet turbulence intensity has been set to 4%.

The mesh used is a multi-block structured mesh as can be seen in Figure 5.2 and Figure 5.3.

A mixture of air and lightly loaded, spherical particles with a uniform size-distribution enters the primary jet, while a swirling stream of air flows through the annulus.

In appendix C the reader can find some calculations on parameters related to the configuration proposed by Sommerfeld & Qiu (1993) in order to get some useful fluid property values (such as gas density and viscosity, fluid velocity profile at inlet in both central and annular swirled jets) to setup the CFD simulations properly.

In this kind of configuration the particle-wall collisions are promoted essentially by the flow field conditions in the gasifier, that mainly are the effect of turbulence and centrifugal forces due to the swirl.

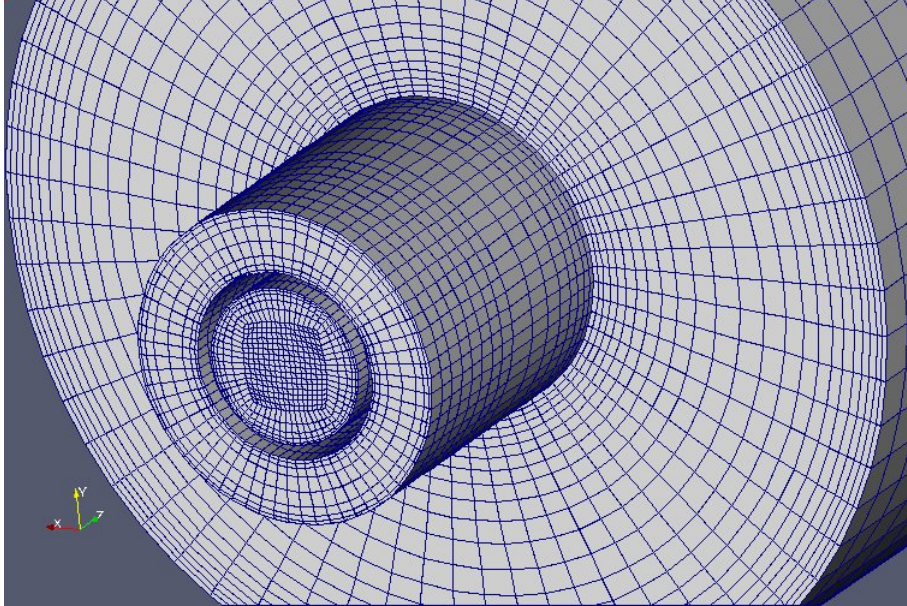


Figure 5.2: 3D view of the meshed combustor inlet

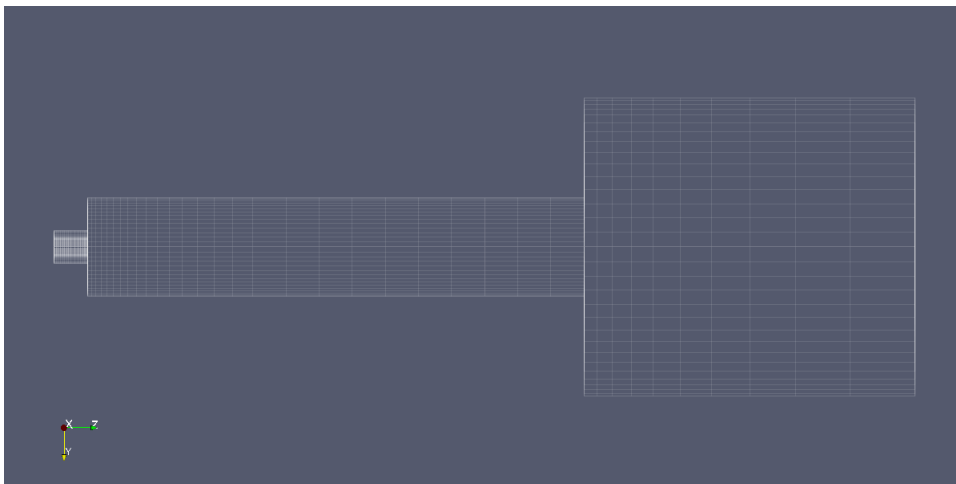


Figure 5.3: 2D view of the mesh of the combustor

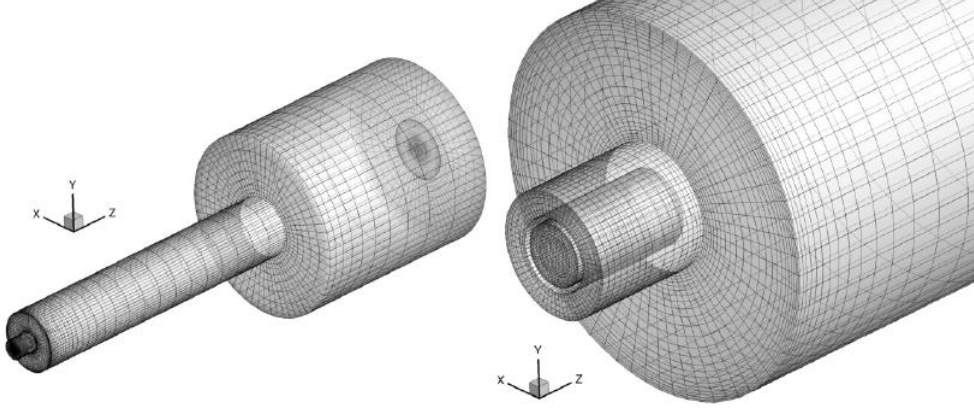


Figure 5.4: Computational domain and grid for the 3D RANS computations

5.2.2 Fluid phase

The gas model used is the perfect gas. The dynamic viscosity is $\mu = 1.83 \cdot 10^{-5} \text{ kg m}^{-1} \text{ s}^{-1}$ to obtain at the temperature of $T = 300 \text{ K}$ the density value $\rho = 1.162 \text{ kg m}^{-3}$ and then a cinematic viscosity $\nu = 1.57 \cdot 10^{-5} \text{ m}^2 \text{ s}^{-1}$.

The numerical model is based on the U-RANS method discussed in section 4.2.1. The momentum equation consider also a generation term in order to consider the effect of the gravity oriented from the inlet to the outlet of the gasifier.

The solver and numerical schemes used in the simulations are described in detail appendix A.1. The solver is a standard OpenFOAM compressible PISO solver modified to support the Lagrangian particle tracking method. In this case a one-way coupling between continuous and particle phase is considered.

5.2.3 Particle phase

Parcels are injected at time $t = 2 \text{ s}$ after that fluid flow passed the transient phase related to the initial condition. Parcels are injected in the central jet at the same velocity of the fluid but with a random direction inside a conic volume with a 30 degrees aperture (cone injection). Particles are all identical: same density, same diameter and so on; are also considered point-wise, rigid and spherical. The particle density is $\rho_p = 2501 \text{ kg/m}^3$ that is the same proposed in the reference case of Sommerfeld & Qiu (1993). All particles rebound at gasifier walls with perfect elasticity. Two different simulation cases are carried out with same fluid flow but different particle properties; in particular particles have different diameter therefore different Stokes num-

ber (different inertia) in order to cover a different possible behavior between particles that have different dimensions (fly-ash, char particles) and/or different conversion degree. As previously underlined in this kind of simulation, particles properties are constant during the simulation process so there is no influence on them by the residence time in the gasifier (that change the conversion degree and then some particle properties such as the diameter).

Each parcel has the same number of particles as discussed in section 4.3. Table 5.1 summarize the difference between the two clouds of parcels simulated within this configuration; N_{pp} is the number of particles that one parcel represents.

d_p [μm]	N_{pp}
45.6	100
102	10

Table 5.1: Characteristic parameters of the two simulated clouds

The frequency of the injected parcels in the domain is coherent with the constraint of the imposed mass flow rate $G_s = 0.34 \cdot 10^{-3} kg s^{-1}$ for both simulations.

5.2.4 Results

The Unsteady RANS simulation has ran for 10 seconds in order to have the fluid passed about 100 times in the combustor before analyzing results. Also the number of particles has reached a regime value.

Figure 5.5 shows the contour map of the wall-normal velocity component in a symmetry section of the gasification chamber of the combustor; It is possible to recognize a zone, situated near the inlet, in which the fluid flow is characterized by the presence of an high value of velocity due to the swirled flow condition. At higher distance from the inlet the effect of the swirler on the fluid motion is reduced as represented in Figure 5.6 in which are shown the velocity components of the fluid near the wall (20 mm from the wall, on the line visible in Figure 5.5). It is possible therefore suppose that particles are driven toward the combustor walls, mainly in the zone near the injection, by a centrifugal force that the swirled flow exerts on particles; this is mainly an inertial effect. Far from the inlet, the effect of the swirl is reduced so it is possible suppose that particles move mainly parallel to the combustor walls. The gasification chamber starts at $z = 0 m$ and ends at $z = 0.96 m$.

These assumptions are justified by analyzing the concentration of particles in the symmetry section of the combustor as shown in Figure 5.7: this

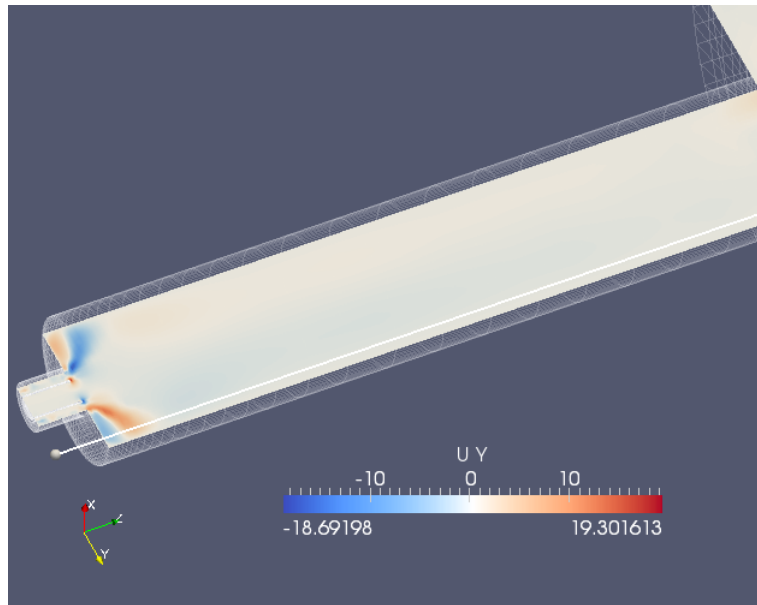


Figure 5.5: Wall-normal velocity component in the gasification chamber [$m s^{-1}$].

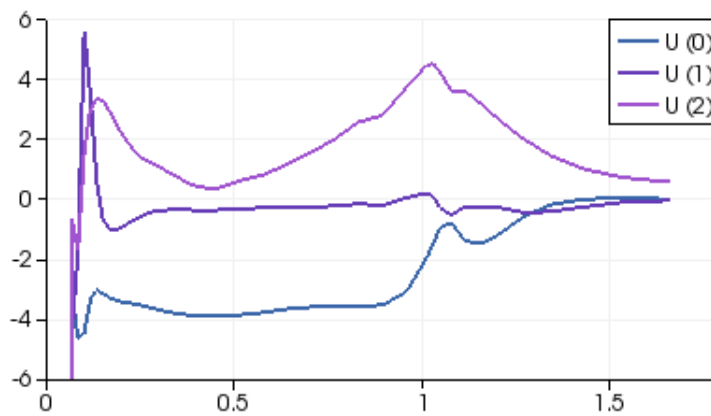


Figure 5.6: Velocity profiles [$m s^{-1}$] along the gasifier length [m]: $U(0)$ is the swirl component, $U(1)$ is the wall-normal component, $U(2)$ is the axial component; Velocities computed at 20 mm distance from the wall.

figure shows the average values of concentration for particles with $d_p = 45 \mu m$ on an equal distribution of 21 time samples from 8s to 10s.

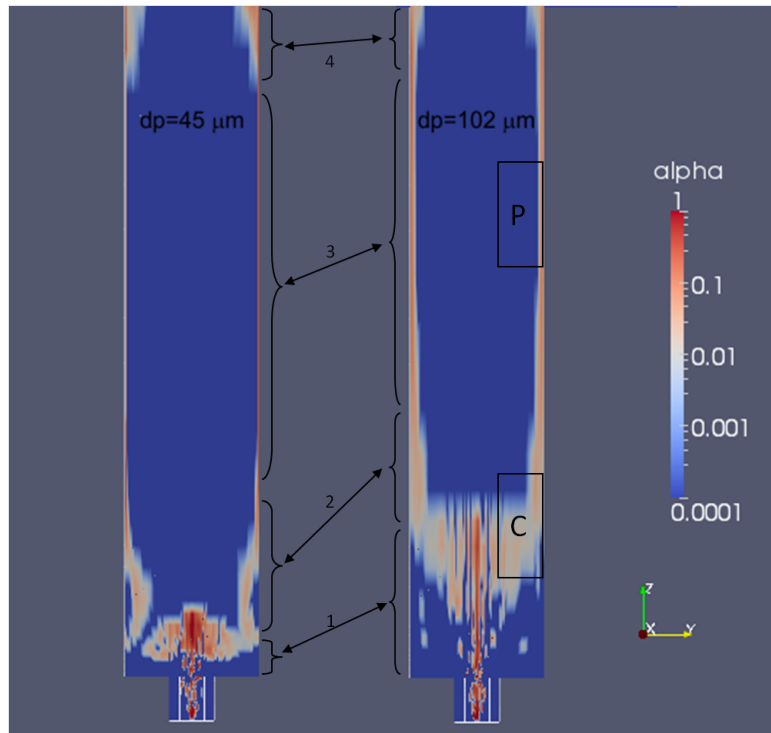


Figure 5.7: Particle mass concentration α for $d_p = 45.6 \mu m$ (right) and $d_p = 102 \mu m$ (left) in the gasification chamber.

As shown in Figure 5.7 it is possible to recognize four different zones with different particle motion:

1. zone with a low number of impacts
2. zone characterized by a large number of impacts (especially particles with large inertia)
3. zone with particle motion parallel to the wall
4. zone with particles lifted from the wall

The zone 1 is too close to the top wall of the combustor that particles, driven initially by the axial fluid velocity, can't reach the wall. The zone 2 corresponds to the zone in which are the higher wall-normal velocity component of the fluid (as can be seen in Figure 5.6) so particles are mainly driven

by the swirled flow and impact on the gasifier wall. The zone 3 is longer than others and is characterized by a small wall-normal velocity component of the fluid: the fluid is mainly parallel to the wall surface. Particles are driven by a velocity that is less of the bulk velocity so particles have a bigger residence time in the gasifier compared to particles that remain far from the walls. Particles in zone 4 are lifted from the wall; this is due to disturbances induced by the approaching outlet section that lift the particles from the wall.

5.2.5 Validation

The choice of investigate this prototype of gasification chamber is due essentially to the fact that there is a large amount of published data available on this configuration, both coming from experimental measurements (Sommerfeld & Qiu, 1993) and numerical investigations with both RANS (Sommerfeld & Qiu, 1993) and LES (Apte *et al.* , 2003) approaches, allowing for proper validation.

The aim of the study at this level is to recognize a qualitative behavior of the fluid and particle motion inside the overall gasifier, one one side, and in particular in the near wall region on the other side. So the choice of the studied configuration has not been focused on study a real gasifier but has been done with the aim of catch qualitative information with also a good level of confidence on results.

As described in appendix C the injection has been implemented with respect of data obtained from the proposed benchmark but a degree of freedom was on the specification of velocity profiles at inlet, particularly on the swirled component: in this work a constant angular velocity has been proposed so the swirled component is proportional to the distance from the center of the chamber (symmetry axis). Due to this assumption there are some differences in the velocity profiles near the gasifier injection zone.

In Figure 5.8 some parcel pathlines obtained post processing the computed particle positions for several time steps from time 8s to 10s and colored with the velocity magnitude of the tracing particles, are shown together with the contour of the gas axial velocity component in the middle plane section. Results are shown for both different particle sizes considered. Lighter particles are drawn by the flow field after few rebounds when they firstly hit the walls while heavier particles are substantially unaffected by drag continuing to rebound for all the gasifier length.

In Figure 5.9, reported from Sommerfeld & Qiu (1993), are shown the pathlines for the same configuration but for particle sizes slightly different

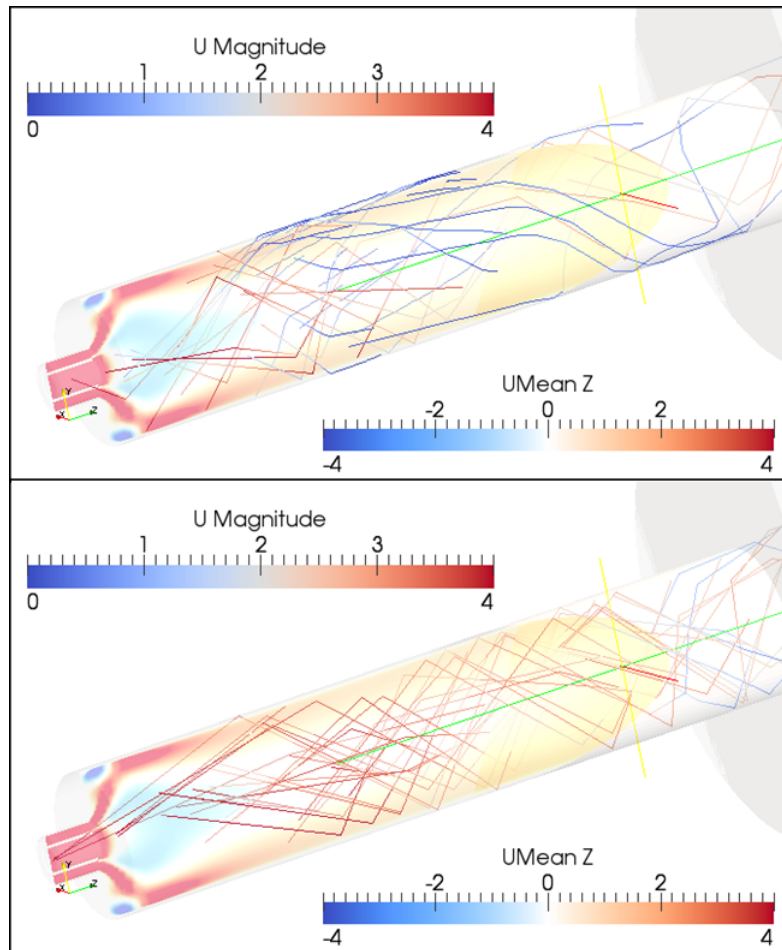


Figure 5.8: Particles pathlines in the gassifier for $d_p = 45.6 \mu m$ (top) and $d_p = 102 \mu m$ (bottom) from time 8s to 10s, U magnitude scale [$m s^{-1}$] refers to particle velocity, Umean Z scale [$m s^{-1}$] refers to flow axial mean velocity.

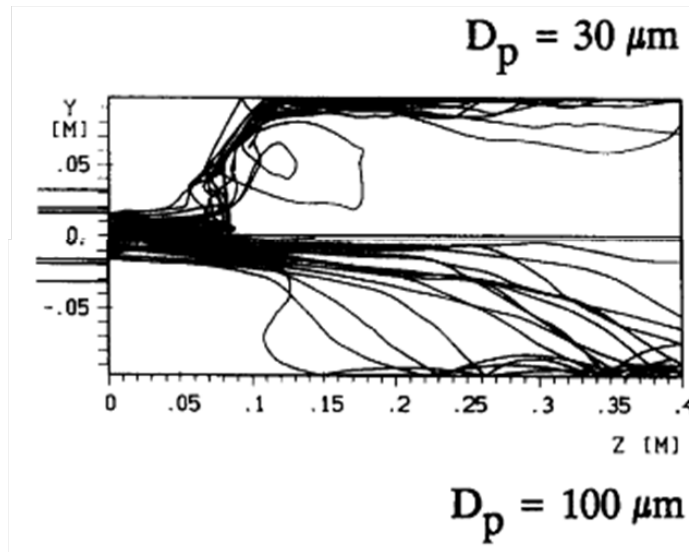


Figure 5.9: Particle trajectories for $d_p = 30 \mu\text{m}$ (top) and $d_p = 100 \mu\text{m}$ (bottom) from Sommerfeld & Qiu (1993).

(same order of magnitude): clearly the qualitative behavior has been reproduced.

5.3 From U-RANS to LES level

Figure 5.7 shows a qualitative behavior of particle segregation in the gasification chamber for both lighter and heavier particles. To better investigate the mechanism of particle-wall interaction, two simplified configurations have to be investigated, with a more detailed model (in particular with a large eddy model) for turbulence description: these configurations are represented by the boxes *C* and *P* in Figure 5.7 that represent a curved and a planar channel respectively, described in the next section. The box *C* represents a zone of the studied gasifier in which the flow velocity is characterized by high swirl conditions. In particular the curvature of the configuration has been set to the same value of a cross section of the gasifier. As it is already noticed through Figure 5.6, in the zone characterized by the parallel to the wall motion of the particles, there is still a swirl component of the fluid velocity. In this context, the planar channel configuration is not intended to represent a real zone in the gasifier rather a conceptual zone in which there is no swirl component of the fluid. Both configurations actually can be seen as not real zones in the gasifier but limit zones in which there are: only swirl and no

axial component of the fluid and is represented by the curved configuration, only axial and no swirl component of the fluid and is represented by the planar configuration.

In the P zone, turbophoresis is considered to be the dominant effect for particle segregation so, in the channel configuration it is important to reproduce a turbulent flow condition compatible with the one in the gasifier. Figure 5.10 shows the contour map of the shear stress τ_w on the walls of the gasifier chamber.

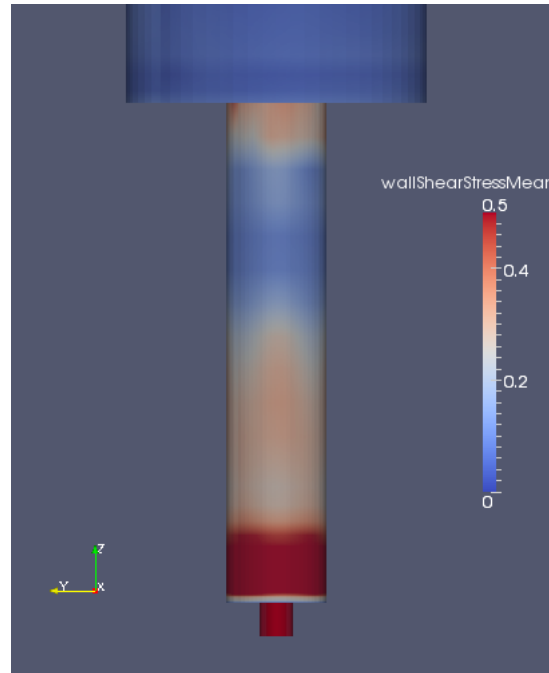


Figure 5.10: Distribution of the wall shear stress of the gasifier chamber.

If it is possible to consider the parallel-to-wall flow in the gasifier like a parallel-to-wall flow in a channel, it is important to have similarity between velocity profiles of the parallel velocity near the wall in order to have a Re_τ of the same order of magnitude. Taking a look at the velocity profile in a section of the gasifier as reported in Figure 5.11 it is possible to note that the parallel-to-wall velocity is going from zero on the wall to a value of about $u = 4 \text{ m s}^{-1}$ at a distance of about $h = 0.02 \text{ m}$ from the wall. Putting these values in the definition of

$$Re_\tau = \frac{\rho u_\tau h}{\mu}$$

and being $u_\tau = \sqrt{\tau_w/\rho}$ with τ_w ranging from about 0.05 to about 0.3 on the parallel zone P as shown in Figure 5.10, the value of the Re_τ is ranging from about 250 to about 650. As described in the next section, the choice of the value of Re_τ for the planar channel configuration has been set to 150. This value is lower than the just calculated values. This choice is justified by the need to compare the results with a well established test case and because the flow structure remain comparable, at least for the lower part of this range, to that obtained at $Re_\tau = 150$.

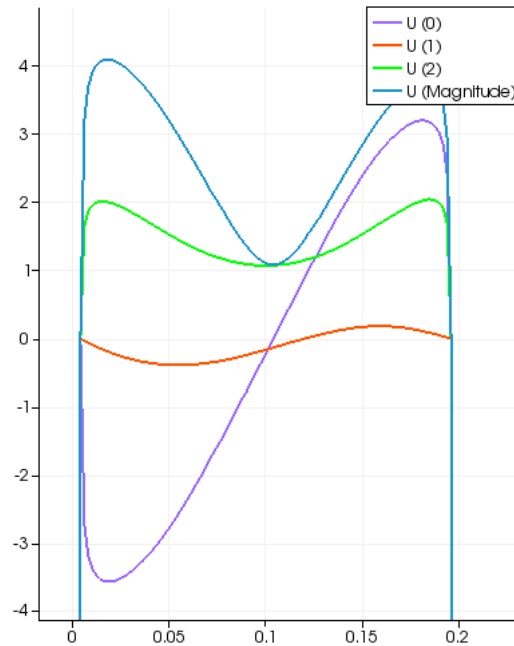


Figure 5.11: Velocity profiles [$m s^{-1}$] in the gasifier chamber section at $z = 0.7 m$; $U(0)$ is the swirl component, $U(1)$ is the wall-normal component, $U(2)$ is the axial component;

Also the Re_τ for the curved configuration is of the same order of magnitude as shown in section 5.4.2.

5.4 LES level

The two configurations considered, as emerging from results of the U-RANS model, are a periodic planar channel and a periodic curved channel.

As described previously, particles in the gasifier are moved toward the reactor walls in different ways depending on the particular flow field inside

the reactor. So we can recognize two different zones, highlighted in Figure 5.7, in which the flow field has different behavior and then the particle wall interaction has different characterization. As shown in the figure, the zone C is characterized by high swirl condition of the flow, so particles are moved toward the walls essentially by the centrifugal force (inertial effect on particles). The zone P on the contrary is characterized essentially by a flow field parallel to the gasifier wall surface.

So the first configuration here proposed aims to characterize an essentially parallel wall-bounded turbulent flow; the second one aims to characterize a non-parallel tangential wall-bounded turbulent flow.

5.4.1 Configurations specification

The case specification of the planar channel is the same of Marchioli *et al.* (2008b) in terms of geometry specification, continuous and particle phases with few exceptions due to limitations and difficulties with the modeling capabilities provided by the CFD toolbox. The physical domain is showed in Figure 5.12. It is a simple three-dimensional flat channel with two infinite flat parallel walls on the top and bottom. These walls confine the jet of particle-laden flow. At the other four sides of the box there are periodic boundary conditions. The origin and orientation of the domain are different from the reference case: the origin is on a bottom corner of the box, the x direction is representing the streamwise direction, z the spanwise and y the wall-normal direction that is the most common choice in literature.

The sizes of the computational domain are the same of the reference case and are $4\pi h \times 2\pi h \times 2h$ with $h = 0.02\text{ m}$ in x , z and y , respectively. The vector fluid velocity is $\mathbf{u} = (u, v, w)$; The plane $y = h$ is a geometrical symmetry plane.

The solver developed to make the computation of the flow field is written within the OpenFOAM toolbox, which is based on the finite volume decomposition method (see section 4.1). Then to have the same level of accuracy, the domain is decomposed in a bigger number of computational cells that leads to a more fine mesh.

This mesh is composed by a structured three-dimensional set of 48×48 equal cells in the x and z direction and of 96 cells in the y direction with size geometrically graded from the walls to the center of the channel. In the y direction the mesh grading have a symmetry respect to a plane parallel to xz and at center of the channel, so the plane $y = h$ is a symmetry plane also for the mesh. The δy^+ of the first cell center near the wall is about 0.2 and at the center of channel is about 21.

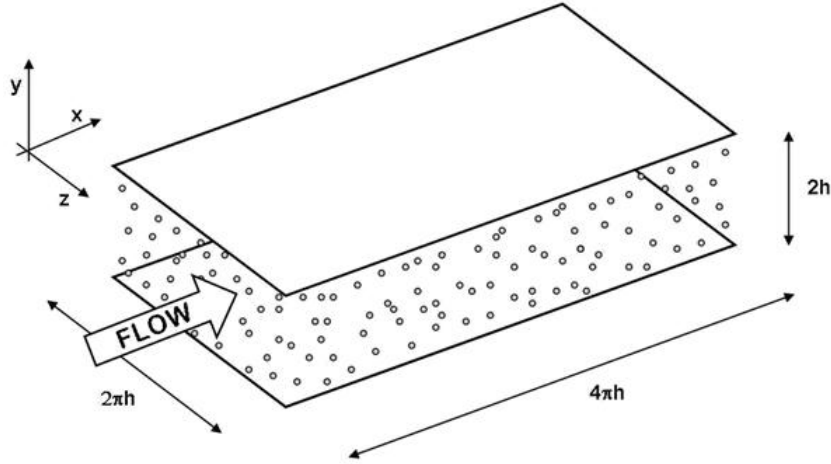


Figure 5.12: Particle-laden turbulent gas flow in a periodic planar channel.

The value of the shear Reynolds number considered is the same of the reference case and is $Re_\tau = 150$ based on the shear velocity $u_\tau = 0.11775 \text{ m s}^{-1}$.

The curved channel configuration proposed is very similar to the planar channel configuration described previously and is shown in Figure 5.13.

As is shown, the curved channel is obtained by a deformation of the planar channel around the axis z . The streamwise direction is an arc and the distance R between the center and the bottom wall (outer wall) is the same of the gasifier configuration described in section 5.2.1. This curvature is the same experienced by a hypothetical fluid flow that, in the gasifier configuration described in section 5.2.1, has only swirl velocity and no axial velocity component. So it can be seen as an extreme situation case. The planar channel configuration, on the other hand, has no curvature so it can be seen as the other extreme situation case in which there is only axial velocity component and no swirl. Spanwise and streamwise dimensions and height of the curved channel are the same of the planar channel. The driven force of the fluid is supplied by the rotation of the inner wall in counterclockwise direction. The walls in the spanwise and streamwise directions are characterized by periodic conditions for both fluid and particle phase as it is in the planar configuration.

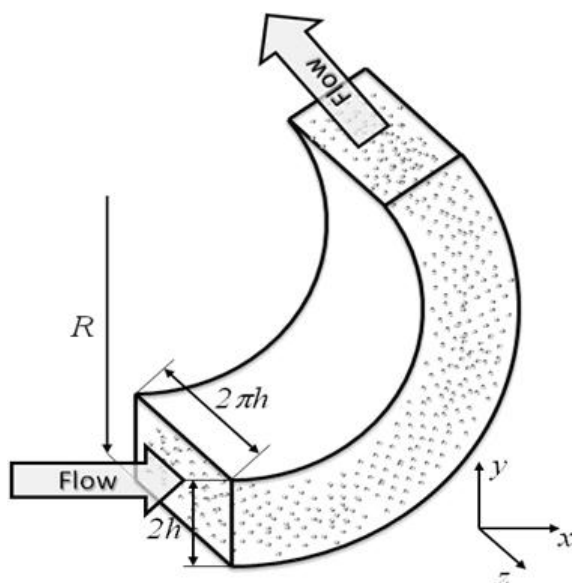


Figure 5.13: Particle-laden turbulent gas flow in a periodic curved channel.

5.4.2 Fluid phase

The gas model used for both configuration is the perfect gas. The dynamic viscosity is $\mu = 1.82 \cdot 10^{-5} \text{ kg m}^{-1} \text{ s}^{-1}$ to obtain at the temperature of $T = 300 \text{ K}$ the density value $\rho = 1.159 \text{ kg m}^3$ and then a cinematic viscosity $\nu = 1.57 \cdot 10^{-5} \text{ m}^2 \text{ s}^{-1}$.

The numerical model is based on the LES method discussed in section 4.2.1.

The solver and numerical schemes used in the simulations are described in detail in appendix A.1. The solver is a standard OpenFOAM compressible PISO solver modified to support the Lagrangian particle tracking method. Moreover, for the planar channel configuration, the momentum equation is modified to take into account a driven force provided by the imposition of a pressure jump in the streamwise direction. This pressure jump is needed to balance the shear stress in the fluid and then to keep statistically constant the mass flow rate of the fluid. The reader can find a detailed description of this pressure jump calculation in appendix B.

Fluid motion in the curved channel configuration is preserved by the rotation of the inner wall with a constant angular velocity $\omega = 72 \text{ rad/s}$ to obtain a bulk velocity similar to that of the planar channel.

Turbulence intensity is expressed by the shear Reynolds number Re_τ . As already specified, for the planar channel has been chosen the reference value

$Re_\tau = 150$. The corresponding value for the curved channel is $Re_\tau \approx 210$, evaluated from the computation of the wall shear stress τ_w being

$$Re_\tau = u_\tau h \rho / \mu$$

$$u_\tau = \sqrt{\frac{\tau_w}{\rho}}$$

$$\tau_w = \mu \left. \frac{dv_\theta}{dr} \right|_R$$

Initial conditions for velocity are represented by a parabolic profile perturbed along the streamwise and spanwise directions in order to promote transition to turbulent regime. The initial temperature profile is assigned to impose a non-zero heat flux through the boundaries using the laminar distribution. Isothermal and no-slip boundary conditions are used on the solid walls. Gravity force is not considered in the momentum source term for both configurations.

5.4.3 Particle phase

For both configurations the simulation started at $t = 0$ s; At time $T = 50$ s a number N of particles are injected in the channel. The injection adopted is not physical indeed the particles were placed instantly in the overall channel domain. Particles are placed randomly along the x , y and z direction respectively. The total number of particles is $N = 100000$.

The initial particle velocity is the same of the fluid at particle positions. Particles are considered point-wise, rigid and spherical. The particle density is $\rho_p = 1000$ kg/m³.

Following the same assumptions made in Marchioli *et al.* (2008c) it's possible to recognize that relevant forces are Stokes drag and buoyancy. Moreover it's not considered the gravity so the differential equations of the particle motion 3.1 and 3.2 become:

$$\frac{d\mathbf{x}_p}{dt} = \mathbf{u}_p \quad (5.1)$$

$$\frac{d\mathbf{u}_p}{dt} = -\frac{3}{4} \frac{C_D}{\rho_p} \left(\frac{\rho}{\rho_p} \right) |\mathbf{u}_p - \mathbf{u}| (\mathbf{u}_p - \mathbf{u}) \quad (5.2)$$

where \mathbf{x}_p is the particle position, \mathbf{u}_p is the particle velocity, ρ_p is the particle diameter and \mathbf{u} is fluid velocity at particle position. The Stokes drag coefficient is computed with the Eq. (4.26). The gravity force has not been taken into account so the drag force is the only one acting on the particles.

Periodic boundary conditions are imposed on particle moving outside the computational domain in streamwise and spanwise directions, so them are reintroduced via periodicity.

Different particle clouds are injected; these are the same clouds considered in the cited work of Marchioli *et al.* (2008c). Each particle of the cloud has the same diameter d_p that is different among the different clouds. Considering as viscous time scale of the flow $\tau_f = \nu/u_\tau^2 = 1.13 \cdot 10^{-3} s$ for the planar channel, it is possible to have two different particle clouds with different Stokes numbers as shown in Table 5.2. The d_p^+ value represents the particle diameter in dimensionless wall unit for both simulated particle clouds. It is important to note that for the curved channel configuration the turbulent velocity profile, shown in Figure 5.31, leads to a $Re_\tau \approx 210$ and therefore to a viscous time scale slightly different to the one related to the planar channel. The considered clouds represent two different Stokes number in the curved channel configuration that are reported also in Table 5.2.

St^p	St^c	$d_p [\mu m]$	d_p^+	$\tau_p [s]$	α_0
5	10	45.6	0.342	$5.66 \cdot 10^{-3}$	0.003361
25	50	102	0.765	$28.32 \cdot 10^{-3}$	0.03761

Table 5.2: Characteristic particle simulation parameters

In Table 5.2 the superscripts p and c applied to the Stokes number notation refer to the planar and curved configuration respectively. The mean concentration of the particle phase is α_0 and it is reported in Table 5.2 for both considered particle clouds. These values are low enough to consider dilute system conditions as the same as Marchioli *et al.* (2008c). One-way coupling between fluid and particle phase is considered so fluid perturbations due to particles as well as particle-particle collision effects are neglected.

The particle-wall interaction model described in section 4.3.1 has been applied. For each of the two considered clouds has been studied the wall interaction considering different normal (ϵ) inelastic restitution coefficient. In particular are been simulated four different values for the normal restitution: $\epsilon = \{0.2, 0.5, 0.8, 1\}$ where $\epsilon = 1$ means perfect elasticity.

5.4.4 Results

The particle concentration α (see section 4.2.2) has been computed for both configurations and for all the different clouds considered (considering only the bottom half part of channels). Each cloud, that is a set of N identical particles, represents a different combination of the two investigated parameters:

the Stokes number St and the wall-normal restitution coefficient ϵ .

In Figure 5.14 and Figure 5.15 is shown the particle mass concentration ratio α/α_0 along the distance from the bottom wall of the planar channel. Results are grouped for different St numbers and shows the effect of different ϵ values. The concentration α is normalized with respect to the initial concentration α_0 . Further information on how these profiles are computed can be found in the validation section 5.4.5.

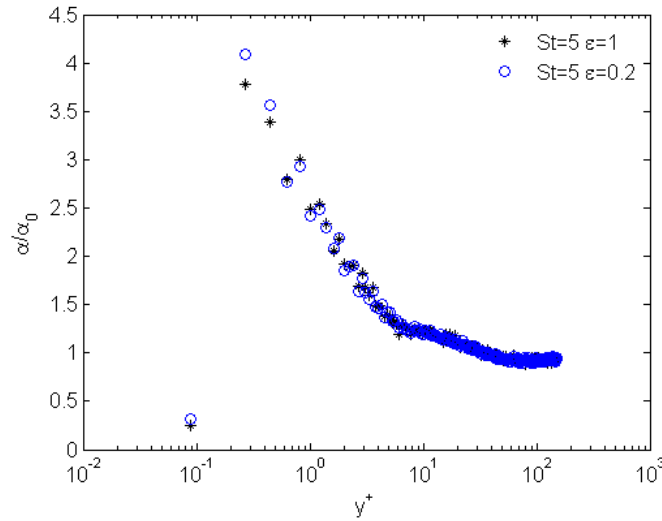


Figure 5.14: Average particle mass concentration α/α_0 along y^+ for the planar channel, $St = 5$ and different ϵ ;

The particle concentration is higher for heavy particles, it means that turbophoresis effect is higher for particle with higher Stokes number. For small particles a limited effect of the restitution coefficient is observed while for heavier particles a higher value of particle concentration is observed when switching from a complete ($\epsilon = 1$) to a more partial ($\epsilon = 0.2$) restitution. The presence of $\alpha > 0$ in the first two coordinate y^+ in Figure 5.15 is due to a still uncorrected bug present in the LPT described in section 4.3.1. The correction proposed by the author and described in appendix A.2 have the aim of simulate a correct wall rebound when particle radius (that is the distance from the particle position represented by its center and the actual particle surface) is bigger then the height of the mesh cell closer to the wall. That correction has proven been effective for perfectly elastic rebound. For not elastic rebound, this error have the behaviour of an accumulation error: it increases with the simulation time. As will be shown, it does not affect the

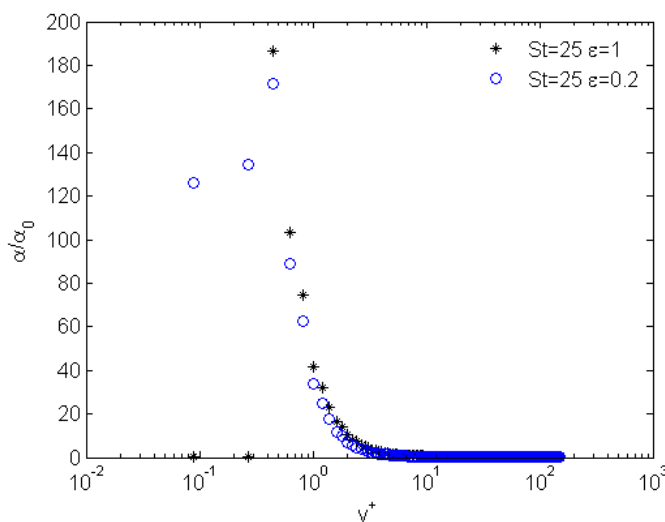


Figure 5.15: Average particle mass concentration α/α_0 along y^+ for the planar channel, $St = 25$ and different ϵ ;

results before a critical time that fortunately is far away the establishment of the statistically steady phase of accumulation, allowing to have enough valid data to collect the required information. In fact, for the cloud characterized by $St = 25$ and $\epsilon = 0.2$, particle statistics are collected in the simulation time interval from $120s$ to $220s$. The cause of the error in the particle concentration profile and how it is related to low ϵ values is still under investigation. The author is aware of the fact that, for $St = 25$, some information particularly in the vicinity of the wall, could be affected by this error if no attention is paid to this issue.

The order of magnitude of maximum particle concentration for $St = 25$ is high enough to invalidate the hypothesis of dilute conditions near wall so more complex coupling phenomena between phases have to be considered. It is observed that the concentration is quite sensitive to the distribution of the slices thickness adopted to compute the concentration values. The same distribution considered by Marchioli *et al.* (2008b) has been here adopted to allow direct comparison with benchmark results. However in section 5.4.5 will be shown some work done in order to validate the results shown above.

In order to calculate the order of magnitude of the impact velocity on the wall, statistics are calculated considering the vertical velocity of all particles being inside a region situated near the wall. Values are obtained considering particles at $y_p \leq 120 \mu m$ and averaging on a suitable time period. In

Figure 5.16 is shown the probability density functions (pdf) of the vertical velocity of particles close the bottom wall of the planar channel for $St = 5$ and different ϵ values: again limited effect of the restitution coefficient is observed. In Figure 5.17 is shown the pdf of the vertical velocity of particles close the bottom wall of the planar channel for $\epsilon = 1$ and different St values: there are more particles with a small vertical velocity in the case of $St = 25$. In all the studied situations the order of magnitude of the particle vertical velocity, that is a good approximation of the impact velocity onto the slag surface, is about $10^{-4} m s^{-1}$. This is a clue on the hypothesis, supposed by Montagnaro & Salatino (2010), that the entrapment regime is not probably due to ballistic reasons.

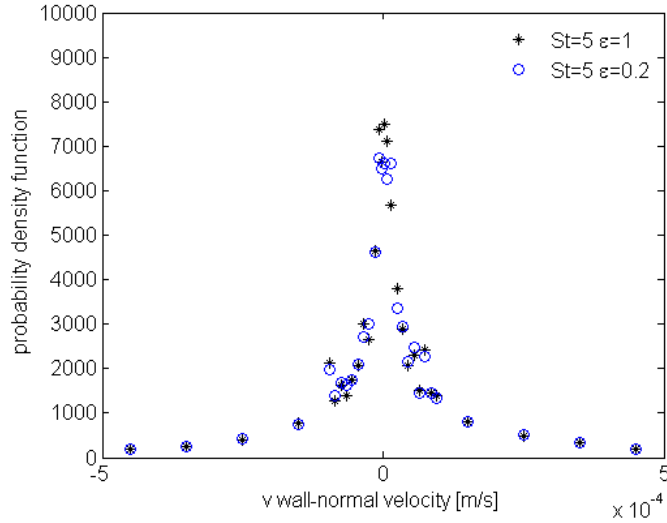


Figure 5.16: Probability density function of the vertical velocity for particles close to the bottom wall of the planar channel: $St = 5$, different ϵ values;

For the curved channel configuration it is possible to recognize a different behavior of particle accumulation:

- accumulation take place much faster due to inertial forces acting on particles (see Figure 5.34);
- particle concentration is much bigger for both considered particle clouds, in particular a dense phase is reached also for light particles. Figure 5.19 shows the average particle mass concentration α/α_0 along the curved channel y^+ for both $St = \{10, 50\}$ and perfect elastic rebound at wall $\epsilon = 1$, only 1s after injection;

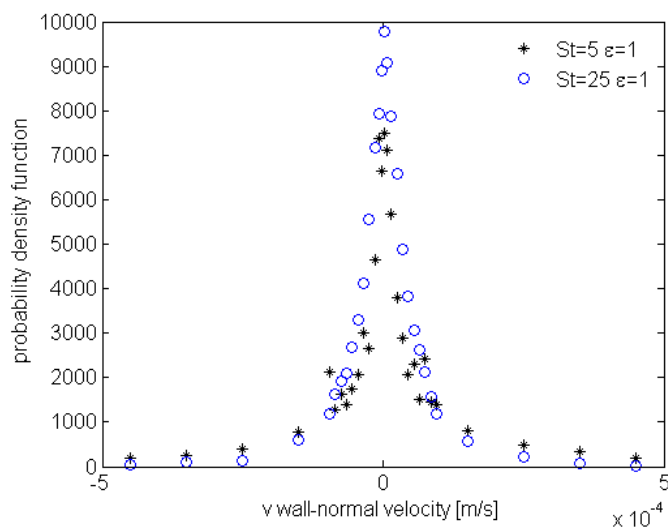


Figure 5.17: Probability density function of the vertical velocity for particles close to the bottom wall of the planar channel: $\epsilon = 1$, different St values;

- impact velocity at wall is higher than that due to turbophoresis (especially for particles with $d_p = 45.6 \mu m$). Figure 5.21 shows the probability density function of the vertical velocity for particles close to the bottom wall of the curved channel: $\epsilon = 1$, different St values, only 1s after injection;
- the effect of the normal restitution coefficient ϵ is enhanced maybe due to the bigger velocity of impact at wall. Figure 5.20 shows the average particle mass concentration α/α_0 along the curved channel y^+ for $St = 10$ and both elastic rebound at wall $\epsilon = \{1, 0.2\}$, only 1s after injection;

In Figure 5.23 are shown top views of the bottom wall of the planar channel for both $St = \{5, 25\}$ and both $\epsilon = \{1, 0.2\}$. In those figures only particles close to the wall (distance lower than $4mm$) are shown so it is possible to see the particle and boundary layer interaction.

In Figure 5.23 it is possible to see different particle concentration along spanwise and streamwise directions. That behavior is due to the presence of turbulent eddies near the wall that are affecting to the particle concentration. This phenomenon is not possible to be caught by a RANS method (Soldati, 2005). The snapshots are taken at time 1200s of the simulation except for the one related to $St = 25$ and $\epsilon = 0.2$ that has been taken at time 200s.

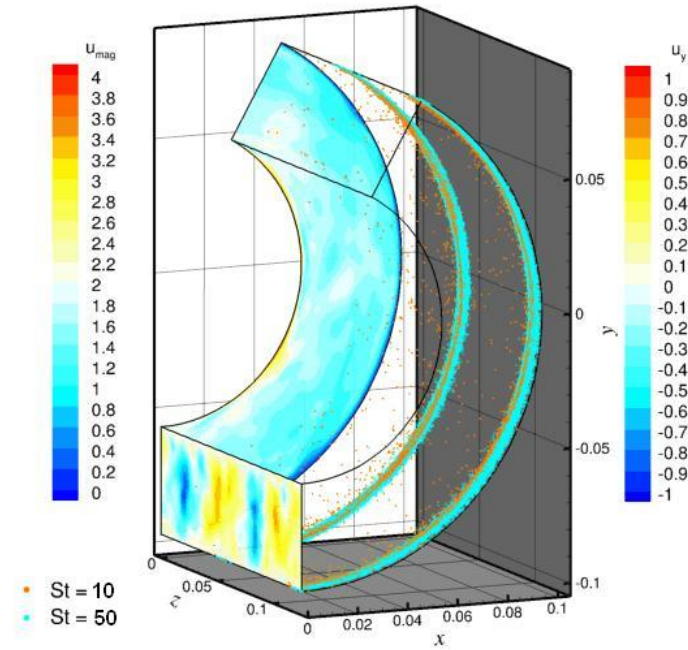


Figure 5.18: 3D view of the curved channel: fluid velocity contours [$m s^{-1}$] and particle positions for $St = \{10, 50\}$ and $\epsilon = 1$ at 30s after injection;

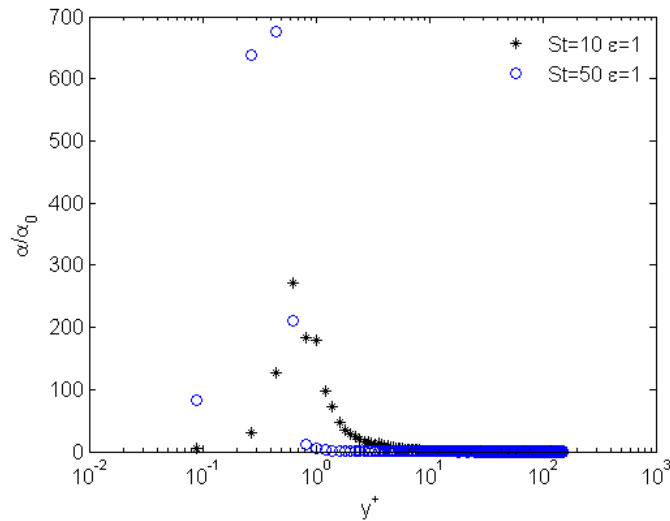


Figure 5.19: Average particle mass concentration α/α_0 along y^+ for the curved channel, $St = \{10, 50\}$ and $\epsilon = 1$, 1s after injection;

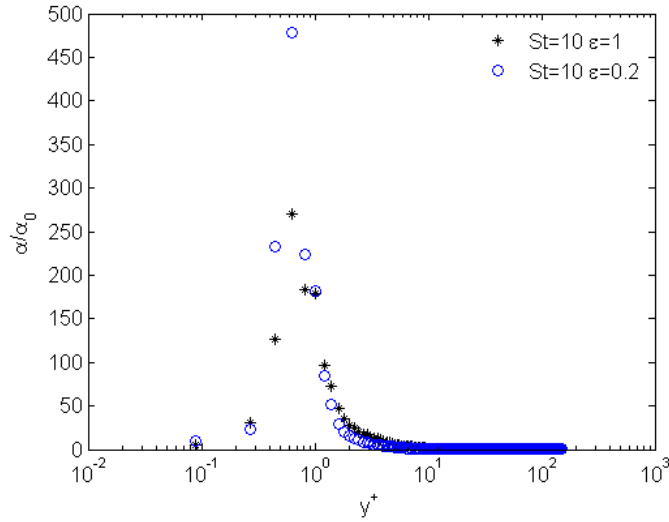


Figure 5.20: Average particle mass concentration α/α_0 along y^+ for the curved channel, $St = 10$ and $\epsilon = \{1, 0.2\}$, 1s after injection;

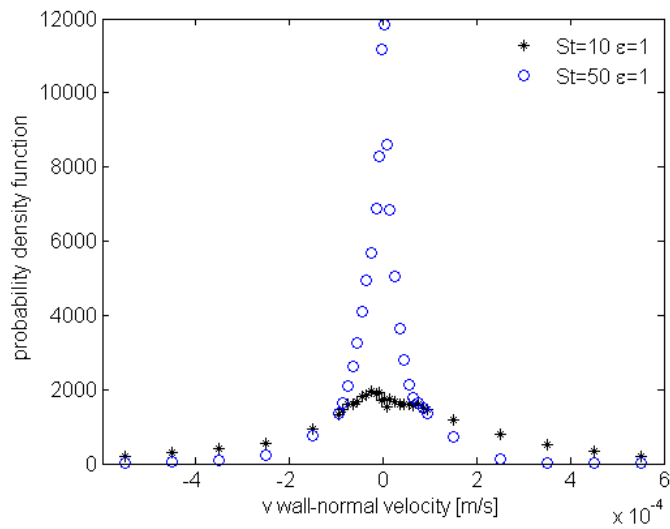


Figure 5.21: Probability density function of the vertical velocity for particles close to the bottom wall of the curved channel: $\epsilon = 1$, different St values, 1s after injection;

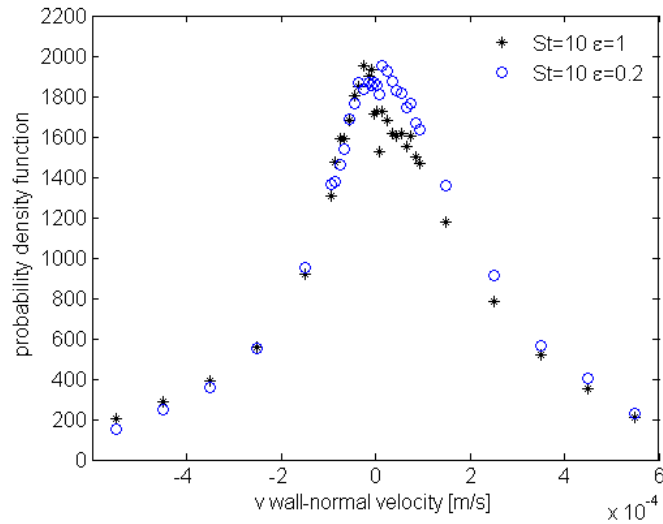


Figure 5.22: Probability density function of the vertical velocity for particles close to the bottom wall of the curved channel for $St = 10$ and $\epsilon = \{1, 0.2\}$, 1s after injection;

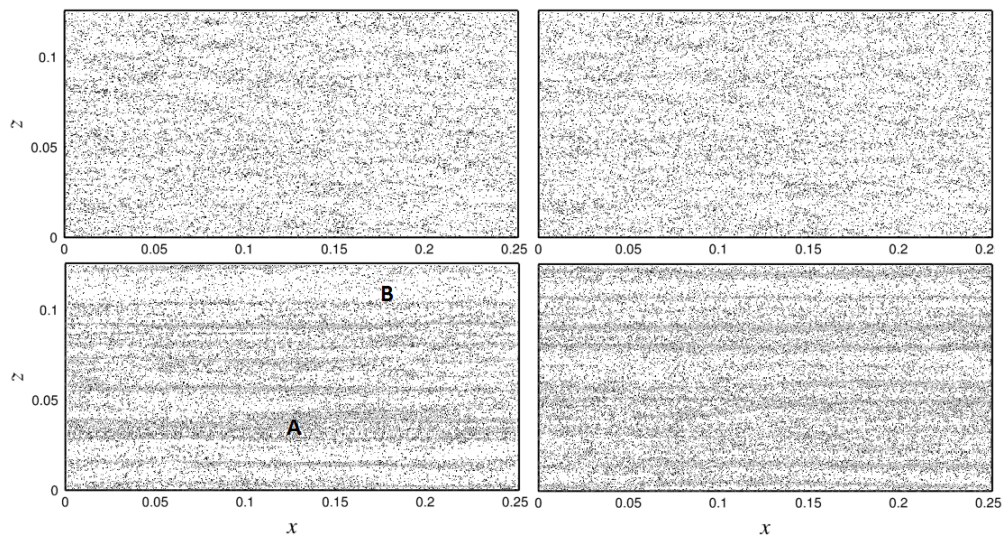


Figure 5.23: Snapshots of the particles distribution near the wall (maximum distance less than 4mm). Planar channel flow case. Top (left and right): $St = 5$. Bottom (left and right): $St = 25$. Left (top and bottom): $\epsilon = 0.2$. Right (top and bottom): $\epsilon = 1$.

The positions A and B in Figure 5.23 are related to points in which there is a high and low concentration respectively. Figure 5.24 shows the particle concentration related to a cylindrical domain of $120 \mu m$ height and radius r for increasing r for the case of $St = 25$ and $\epsilon = 1$. In this figure on the x axis is represented the radius r of the cylinder divided by the particle diameter d_p . The center of the cylindrical domains are the positions A and B described above. In the figure are represented the different local particle concentrations near the wall for the two different positions: the concentration is higher, the closer we are to point A while is smaller the closer we are to point B. Concentration tends to a value that is the average on the all channel with the increase of r .

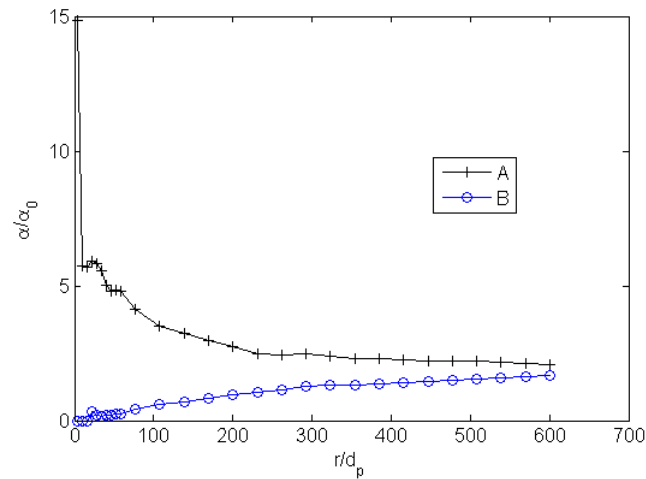


Figure 5.24: Particle concentration α/α_0 along the distance from points A and B in the planar channel: $St = 25$, $\epsilon = 1$

5.4.5 Validation

LES calculations on the planar channel configuration have been performed on two computational grids: a coarse grid made of $32 \times 64 \times 32$ cells (called *LES 1* for simplicity) and a fine grid made of $48 \times 96 \times 48$ cells previously described (called *LES 2*). Both two mesh levels are obtained with a growing geometric distribution of the cell length in the y direction and with a uniform distribution in the x and y directions. The *LES 2* mesh is substantially more accurate toward the center of the channel.

The *LES 2* computational mesh is a little different of the Marchioli *et al.* (2008c) coarse mesh for the LES simulation but near the wall both have approximatively the same level of accuracy. The governing equations were discretized by Marchioli *et al.* (2008c) using a pseudo-spectral method based on transforming the field variables into wavenumber space. They used a Fourier-Galerkin method in the periodic streamwise and spanwise directions, and a Chebyshev-collocation method in the wall-normal direction.

Only a *LES 2* mesh has been implemented for the curved channel configuration.

Fluid phase validation

Here will be now shown some results for the planar channel for both mesh levels; this results are obtained by averaging values in a time interval to obtain valid statistics as previously discussed. The time interval chosen for the averaging is from $T = 500 s$ to $T = 700 s$.

The development of the total kinematic energy has been monitored to have confidence on achieving the fully developed turbulence condition. In Figure 5.25 and Figure 5.26 are shown the total specific kinematic energy of the flow field as a function of time for both mesh levels. The particle injection is done after having reached the fully developed turbulence statistics, in particular particles are injected $T = 50 s$.

In Figure 5.27 are shown the velocity profiles for both mesh levels. You may notice that there are more points for the fine *LES 2* curve especially towards the right side of the graph which corresponds to the center of the channel ($y^+ = Re_\tau$). DNS values are referred to the DNS simulation done by the working group of M.F. Cargnelutti and L.M. Portela indicated with *TUD* and published in Marchioli *et al.* (2008b). That set of data has been chosen from the others published on the same paper because that group has adopted a numerical approach and code similar to those adopted in this work.

In Figure 5.28 are shown the velocity profiles (a) and *rms* (b) for all velocity components for the fine mesh of the planar channel. This results

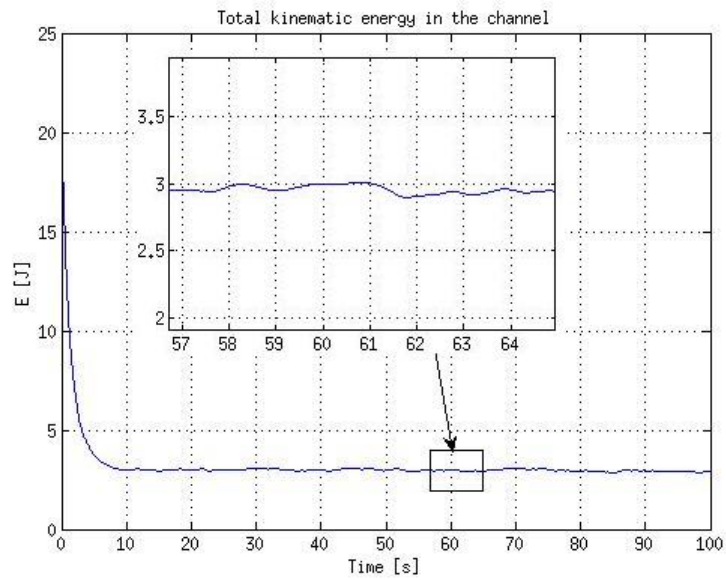


Figure 5.25: Total kinematic energy in the planar channel: mesh coarse (*LES 1*)

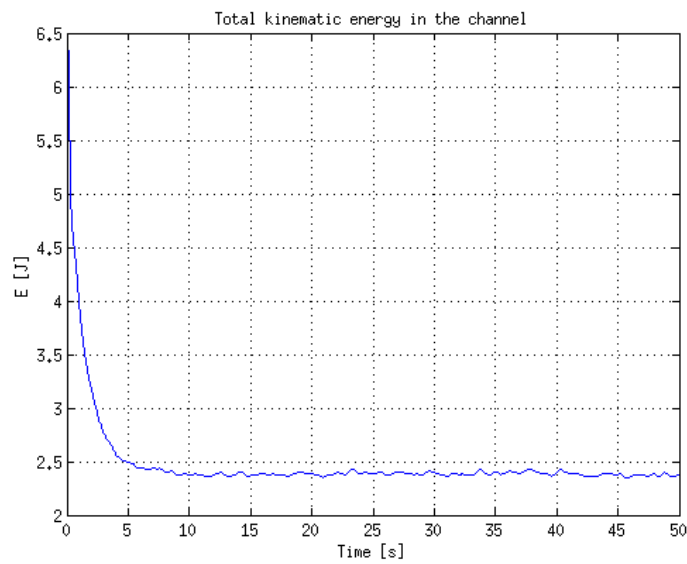


Figure 5.26: Total kinematic energy in the planar channel: mesh fine (*LES 2*)

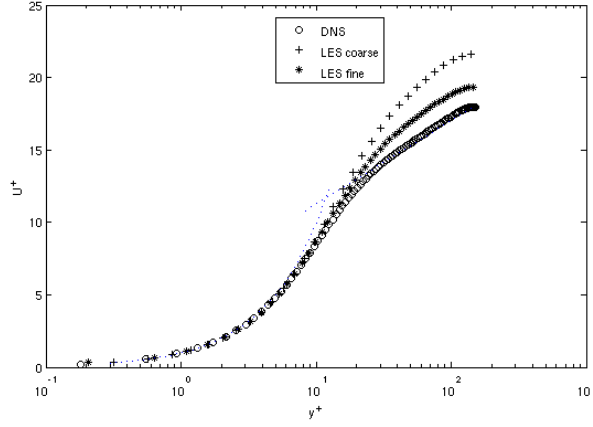


Figure 5.27: Velocity profiles in wall units for the planar channel for different LES levels and DNS data.

show that the level of accuracy attained with the fine grid compare very well with those obtained for the same configuration in the framework of the LES approach, resulting in a slightly greater valued of the centerline velocity with respect to DNS results. This level of accuracy is confirmed by the shape of the rms fluctuations LESinItaly (2011)

In Figure 5.29 are shown the energy spectral density curves for stream and spanwise directions for the coarse mesh *LES-1*. In Figure 5.30 are shown the energy spectral density curves for stream and spanwise directions for the fine mesh *LES-2*. The latter mesh is more accurate in reproducing the characteristic slope $k^{-5/3}$. Both figures are referred to the fluid field in the planar channel configuration.

Figure 5.31 shows the streamwise velocity profile v_θ for the curved channel configuration. The configuration parameters are chosen in order to have a turbulent velocity profile in the bottom half part of the channel as much as possible similar to the profile of the bottom half part of the planar channel. The profile is also similar to the expected profile for such configuration (see White (1991)).

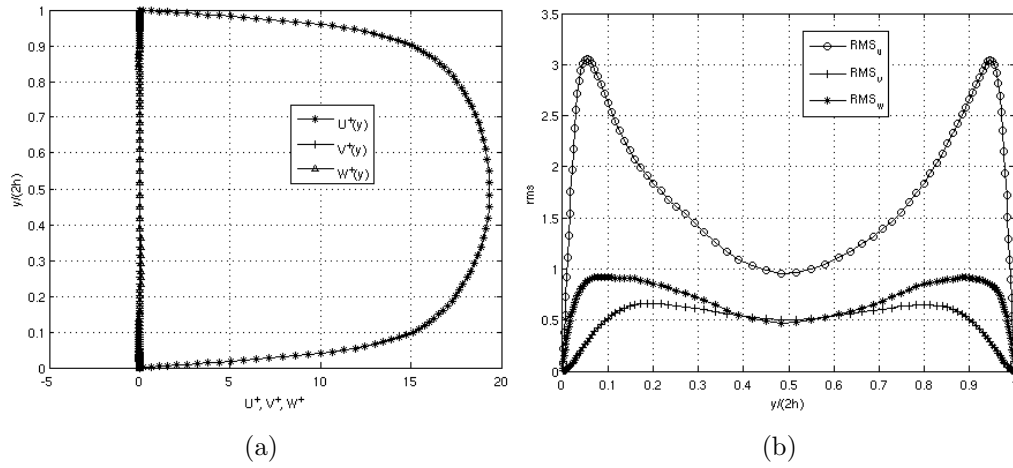


Figure 5.28: Averaged fluid velocities (a) and rms (b) profiles for the fine mesh *LES-2*, planar channel; velocities are dimensionless (divided by u_τ)

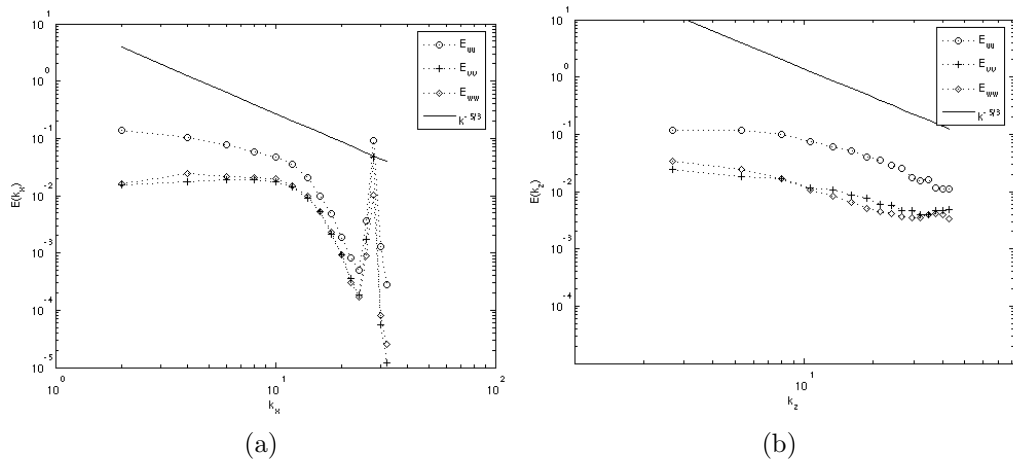


Figure 5.29: Streamwise (a) and spanwise (b) energy spectral density for coarse mesh *LES-1*, planar channel

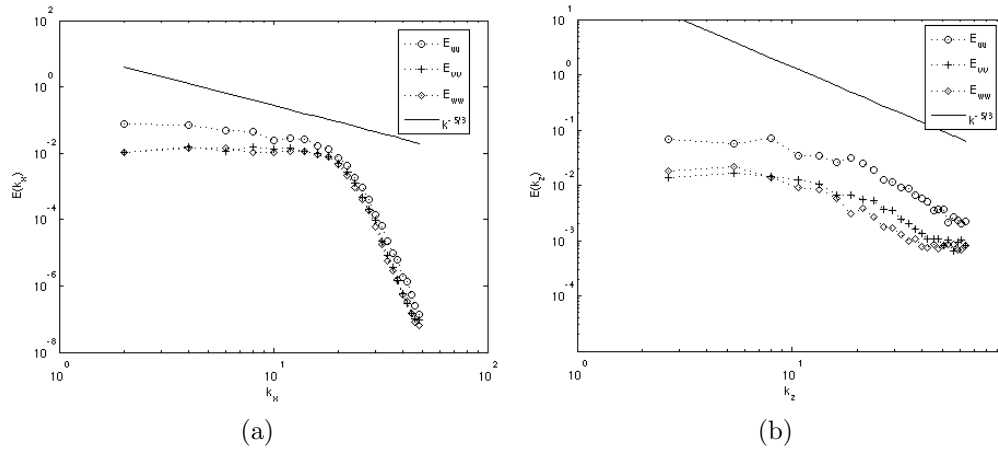


Figure 5.30: Streamwise (a) and spanwise (b) energy spectral density for fine mesh *LES-2*, planar channel

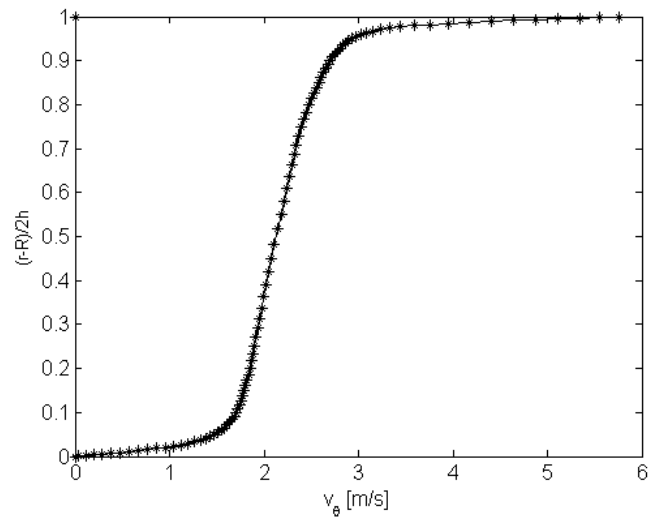


Figure 5.31: Average streamwise fluid velocity v_θ , curved channel;

Particle phase validation

The computation of the particle accumulation in a turbulent boundary layer is strongly influenced by the small scale fluctuation velocity especially for light particles (Marchioli *et al.*, 2008a; Kuerten & Vreman, 2005).

In Figure 5.32 is represented the average particle mass concentration α/α_0 along y^+ for the planar channel and both fine and coarse mesh and for $St = 5$ and $\epsilon = 1$. The turbophoretic effect hasn't been identified by simulations on the coarse mesh *LES-1*. To reduce the effect of the sub grid scale (SGS) velocity the mesh *LES-2* has a very fine resolution near wall: indeed the δy^+ of the first cell near the wall is about 0.2 and the mesh spacing is geometrically incremented in the normal wall direction with a 1.07 ratio.

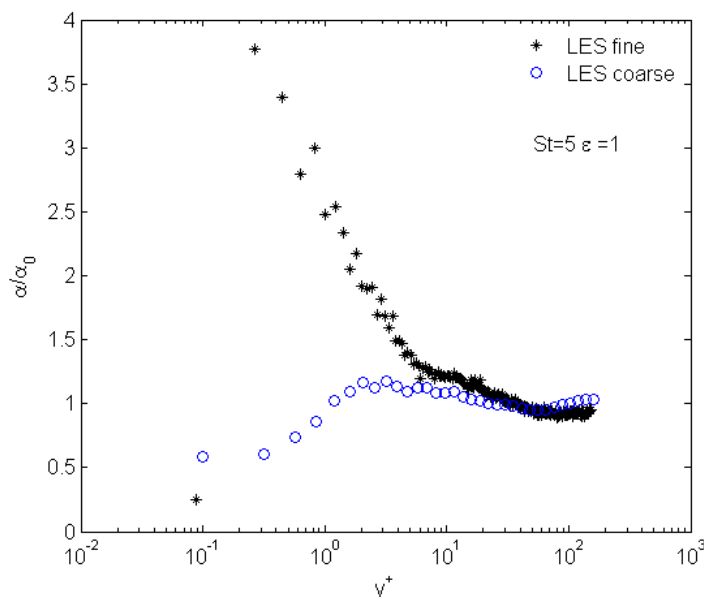


Figure 5.32: Average particle mass concentration α/α_0 along y^+ for the planar channel and both fine and coarse mesh, $St = 5$ and $\epsilon = 1$.

Being turbulence an unsteady phenomenon, the turbophoresis drift is also unsteady. To reach a statistically steady-state for the particle distribution, the process of accumulation was followed over time starting from an initial condition of randomly distributed particles. Results are obtained averaging particle properties at different times temporally equidistant in a period in which the turbophoresis effect is statistically steady. To determine if the accumulation process is in a steady-state, the parameter used has been the maximum value, along the normal wall distance, of the particle concentration

α/α_0 described before. Figure 5.33 shows the time evolution of the maximum value α/α_0 near the wall for the planar channel configuration. In that figure are reported the time evolution profiles for both considered Stokes numbers ($St = \{5, 25\}$) and for the two extreme considered normal restitution values ($\epsilon = \{1, 0.2\}$).

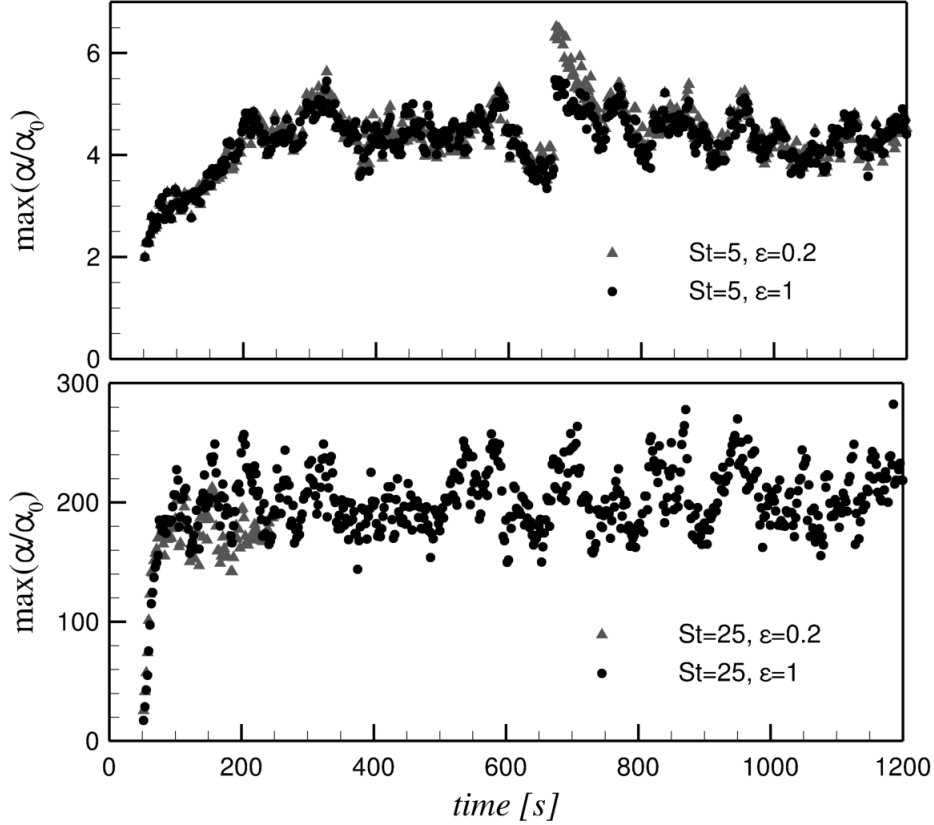


Figure 5.33: Maximum particle concentration α/α_0 at the wall as function of time for the planar channel: $St = 5$ (top) and $St = 25$ (bottom), $\epsilon = \{1, 0.2\}$

Due to the unresolved bug in the LPT (discussed in the previous section), the maximum particle concentration values for the cloud characterized by $St = 25$ and $\epsilon = 0.2$ are been removed from the graph: a no-physical accumulation behavior along time has indeed detected after about time 250s. All the results related to the planar channel and presented in the previous section 5.4.4 are obtained averaging from time 1000s to 1200s, except for the just discussed cloud characterized by $St = 25$ and $\epsilon = 0.2$ for which results are obtained averaging from time 120s to 220s, considering a sampling step of $\Delta t = 10s$ (it has been also verified that results are very weakly influenced

by a different sampling step: other Δt tested are $\Delta t = 1s$ and $\Delta t = 20s$).

The interaction between particles and turbulent eddies leads to an unsteady particle distribution also in the curved channel configuration. Figure 5.18 shows a 3D view of the particles accumulation on the bottom wall of the curved channel, 30s after the injection. It's possible to recognize a strong particles agglomeration in streamwise direction due to particle interaction with characteristic vortical structures in such a particular flow field (annular axial Couette flow, White, 1991).

Figure 5.34 shows the time evolution of the maximum value α/α_0 near the wall for the curved channel configuration. In that figure are reported the time evolution profiles for both considered Stokes numbers ($St = \{10, 50\}$) and for the four considered normal restitution values ($\epsilon = \{1, 0.8, 0.5, 0.2\}$).

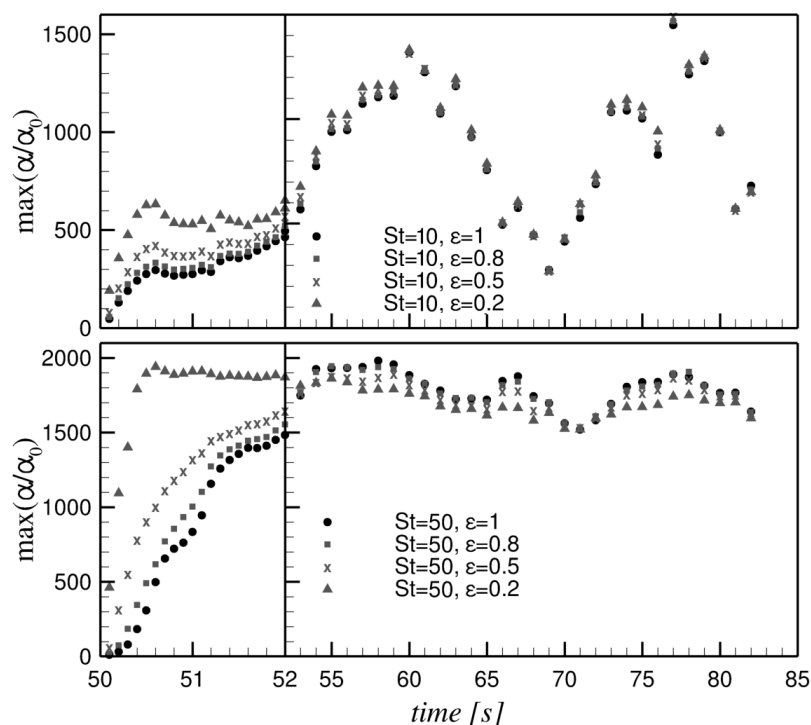


Figure 5.34: Maximum particle concentration α/α_0 at the wall as function of time for the curved channel: $St = 10$ (top) and $St = 50$ (bottom), $\epsilon = \{1, 0.8, 0.5, 0.2\}$

Particles accumulate on the wall very quickly, compared to turbophoresis, and show an unsteady evolution of this phenomenon. Due to the short simulated time interval, results on the curved configuration shown in the previous section are not averaged in time.

All channel simulations are conducted with the one-way coupling assumption. Considering the classification map of dispersed two-phase flows from Elghobashi (2006) and shown in Figure 3.2, it's possible to compute the values of the ratio α/α_0 that are corresponding to the boundary between the 1-way, 2-way and 4-way coupling validity regions. These values are summarized in Table 5.3 (has been neglected for simplicity the difference in volume of the curved configuration with respect to the planar one).

d_p	1 – way	2 – way	four – way
45.6 μm	$\alpha/\alpha_0 \leq 0.257$	$0.257 < \alpha/\alpha_0 \leq 257$	$257 < \alpha/\alpha_0 \leq 1.89 \cdot 10^5$
102 μm	$\alpha/\alpha_0 \leq 0.0229$	$0.0229 < \alpha/\alpha_0 \leq 22.9$	$22.9 < \alpha/\alpha_0 \leq 1.69 \cdot 10^4$

Table 5.3: α/α_0 validity values for different coupling levels for both planar and curved channel configurations.

Turbophoresis leads to a particle accumulation degree that correspond to a dilute dispersion for light particle clouds (for $St = 5$ the concentration is high enough to request the two-way coupling assumption) and a dense suspension for heavy particle clouds (for $St = 25$ the concentration is high enough to request the four-way coupling assumption). The inertial effect on particles, that is due to the swirl, leads to a particle accumulation degree that corresponds to a dense suspension for both light and heavy particle clouds (therefore there is the need of the four-way coupling assumption). On one hand the one-way coupling model, applied to all these simulations, indicates that it is possible to assume that there is a tendency to segregate only in its initial phase but, on the other hand, there are no signs that suggest that this trend is being reversed with a more complex phase coupling implementation.

To obtain statistical values of various entities depending on the distance from the wall the average is done decomposing the channel domains in wall-parallel slices with the same distance from the bottom wall. These slices are distributed non uniformly in the wall-normal direction (so they have a thickness that increase with the wall distance) and are curved for the curved channel configuration.

Particle concentration was obtained as follows: the flow domain is divided into slices as previously described; at each time-step the mass of the particles within each slice is determined multiplying the particle density by the number of particles within the slice; it is also determined the mass of the fluid in the slice (obtained by multiplying the volume of that slice by the fluid density); the local mass concentration of each slice α is computed dividing the mass of the particles by the mass of the fluid; finally, α is normalized by its initial value, α_0 , computed at injection time (this value is uniform in

all the channel domain due to the random uniform particle distribution at injection). According to this procedure, the ratio α/α_0 is in fact a particle number density distribution and will be larger than unity in the flow regions where particles tend to preferentially distribute and smaller than unity in the regions with few particles.

Results shown in the previous section 5.4.4 are obtained decomposing the domain in the same manner as has been in Marchioli *et al.* (2008b); The thickness of the n -th slice, $\Delta y(n)$, was obtained by means of hyperbolictangent binning with stretching factor $\gamma = 1.7$:

$$\Delta y(n) = \frac{h}{\tanh(\gamma)} \left[\tanh\left(\gamma \frac{n}{N_n}\right) - \tanh\left(\gamma \frac{n-1}{N_n}\right) \right] \quad (5.3)$$

where $N_n = 193$ is the number of slices.

The maximum value of the concentration ratio α/α_0 depends on the particular thickness slice distribution implemented in the post-processing procedure. In fact Figure 5.35 and Figure 5.36 show the maximum particle concentration α/α_0 at the wall as function of time for the planar channel for both $St = \{5, 25\}$, $\epsilon = 1$ and different slice distributions: in the figures *fine* is the proposed distribution expressed by Eq. (5.3) and *mesh* is the distribution of slices corresponding to the Eulerian mesh discretization of the wall-normal direction. In the figures are represented values computed at each second in the simulation interval from $t = 1000s$ to $t = 1200s$.

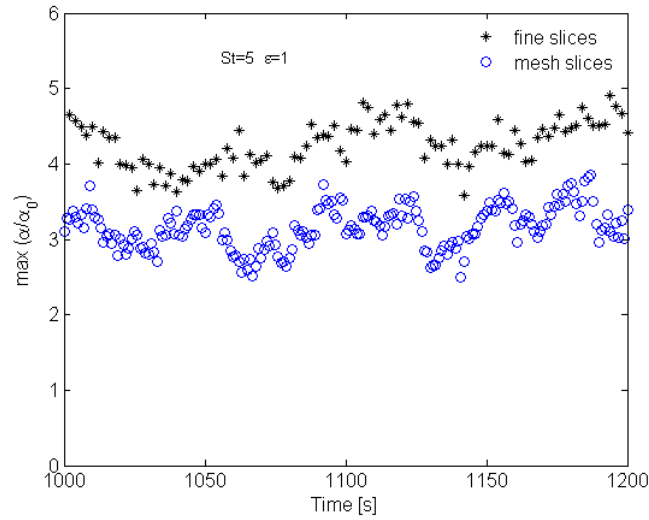


Figure 5.35: Maximum particle concentration α/α_0 as function of time for different slices distribution on the planar channel: $St = 5$, $\epsilon = 1$;

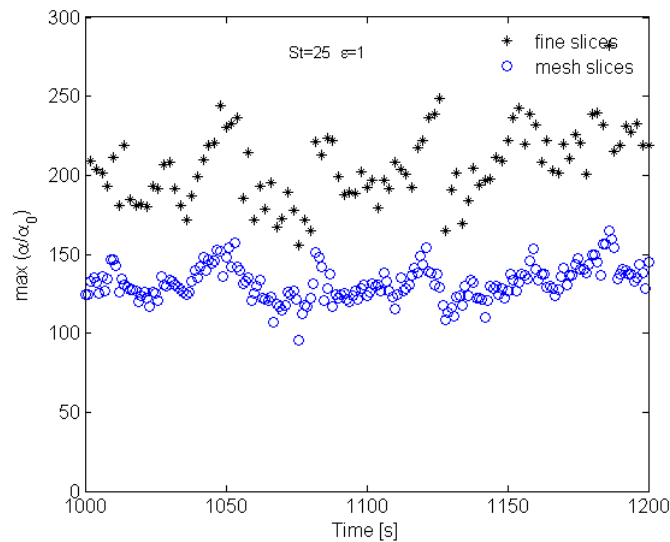


Figure 5.36: Maximum particle concentration α/α_0 as function of time for different slices distribution on the planar channel: $St = 25$, $\epsilon = 1$;

Chapter 6

Further results

In this chapter are illustrated and discussed some very recent results obtained from the multilevel approach model. This results are very recently obtained by simulations and are in post-processing at the time of writing. Because of the little time spent on this results, they could be not very accurate, or affected by errors of interpretation and not enough validated.

Results described in the two next sections regards the effect of the tangential restitution coefficient in the particle-wall interaction and the effect of the two-way coupling between dispersed and fluid phases. All results are related to the planar channel configuration of the LES level described in section 5.4.1.

6.1 Effect of a tangential restitution coefficient at wall

In order so consider the slag presence also as an inelastic restitution in the wall-parallel direction, the effect of a tangential restitution coefficient μ_w at wall is evaluated. The meaning of μ_w is defined in Eq. (4.33) in the section 4.3.1 here reported:

$$u_p^{tt} = (1 - \mu_w) \cdot u_p^t \quad (6.1)$$

where u_p^t and u_p^{tt} are the wall-parallel component of the particle velocities before and after the wall collision.

The effect has been computed for several particle clouds characterized by different combinations, but not all of them, of Stokes number and normal restitution coefficient. Particles starting positions has been set to the positions of the same particle cloud at $T = 1000$ s and perfect elastic tangential

rebound ($\mu_w = 0$). The simulation has ran up to $T = 1040$ s at the time of writing so the statistics on particle positions can be done on a not enough amount of data.

In Figure 6.1 is reported the average particle mass concentration α/α_0 along y^+ for the planar channel and $\mu_w = \{0, 0.2, 0.5\}$, $St = 5$ and $\epsilon = 1$.

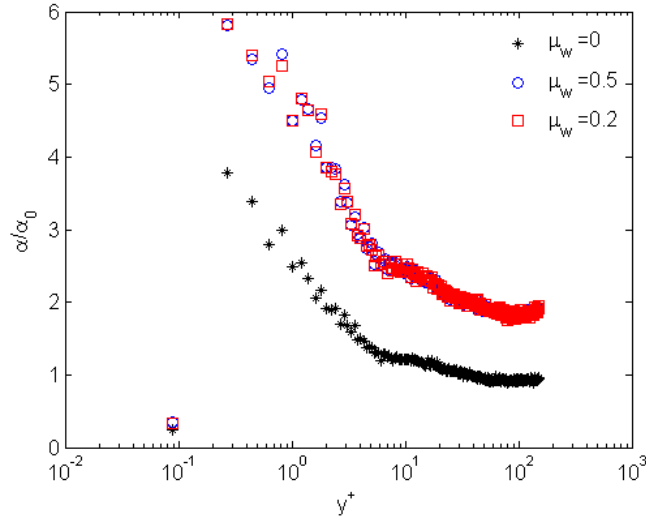


Figure 6.1: Average particle mass concentration α/α_0 along y^+ for the planar channel and both one-way and and $\mu_w = \{0, 0.2, 0.5\}$, $St = 5$ and $\epsilon = 1$.

It can be noticed that the effect of inelastic restitution in the wall-parallel direction in the planar channel is in increasing the segregation as expected. The slightly difference between the two chosen inelastic concentration profiles (with $\mu_w > 0$) indicate that the effect is already marked at very small inelastic coefficient values.

6.2 Effect of two-way coupling

For evaluate the effect of the two-way coupling model, between particle and gas phases, in relation to the more approximate and earlier discussed one-way coupling model, simulations are conducted considering the contribution to the momentum exchange in the momentum equation (details are discussed in section 4.2.3). This effect has been computed only for the particle cloud characterized by $St = 25$ and $\epsilon = 1$. Particles starting positions has been set to the positions of the same particle cloud at $T = 1000$ s computed with the one-way coupling model. The simulation has ran from $T = 1000$ s to

$T = 1200 s$ allowing the same previous time interval for evaluating particle position statistics.

In Figure 6.2 is reported the average particle mass concentration α/α_0 along y^+ for the planar channel and both one-way and two-way coupling models, $St = 25$ and $\epsilon = 1$.

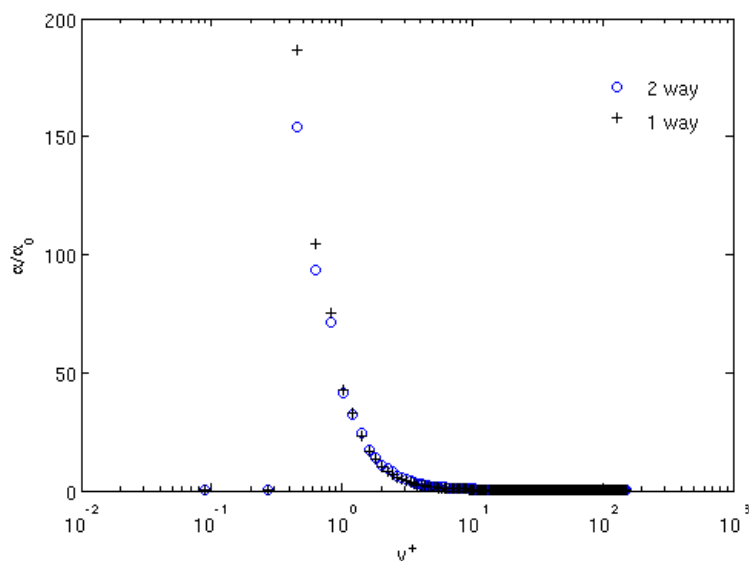


Figure 6.2: Average particle mass concentration α/α_0 along y^+ for the planar channel and both one-way and two-way coupling models, $St = 25$ and $\epsilon = 1$.

In Figure 6.3 is reported the the average probability density function of the vertical velocity for particles close to the bottom wall of the planar channel for both one-way and two-way coupling models, $St = 25$ and $\epsilon = 1$.

The segregation is resulting slightly overestimated with the one-way coupling assumption but the order of magnitude is preserved. It has been noticed that in this case particles are still considered point-wise and, in the proximity of the wall, have diameter length of the same order of the cell size. These can lead to an overestimation of the momentum exchange in many computational cells.

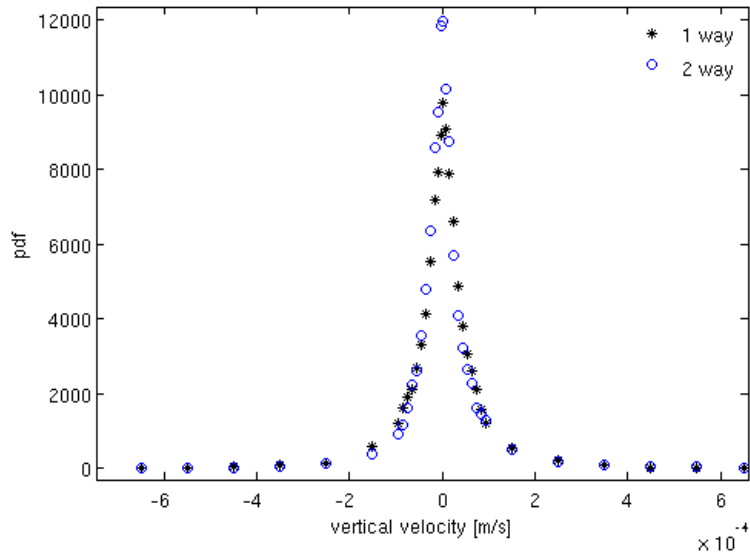


Figure 6.3: Probability density function of the vertical velocity for particles close to the bottom wall of the planar channel for both one-way and two-way coupling models, $St = 25$ and $\epsilon = 1$.

Chapter 7

Conclusions

7.1 Discussion of results

The obtained results confirm the experimental evidence that finer particles could be mainly responsible of particle layering near the solid walls as they, after their first impinging on the wall, assumes a pathway parallel to the wall. In contrast, larger particles continue to bounce over the walls along the whole length of the gasifier (see Figure 5.8). The identification of these two different regions and the characterization of particle classes representative of partially burned coal particles, was the basis for the proper setup of numerical simulations based on a Large Eddy Simulation approach. These simulations aim to characterize, in more details, the interaction between the particle-laden flow and the vortical structures of the turbulent boundary layers near the wall (Figure 7.1 shows a snapshot of this interaction for the planar channel configuration: iso-Q surfaces, where Q is the second invariant of ∇U , are showing the coherent structures in the boundary layer of the bottom wall).

Numerical simulation results do confirm the tendency of the establishment of a region near the wall slag layer (the dense-dispersed phase referred to in the introduction, leading to the formation of the slag fines), in which particles impacting the slag tend to accumulate to an extent depending on the system fluid-dynamics and on parameters such as particles inertia and restitution coefficient. The establishment of this dense-dispersed phase is considered to be beneficial to carbon gasification, due to the increased mean residence time in the gasifier of char particles belonging to this phase. As has been already underlined the one-way coupling model, applied to all the simulations, indicates that it is possible to assume that there is a tendency to segregate only in its initial phase but there are no signs that suggest that this trend is being reversed with a more complex phase coupling implementation.

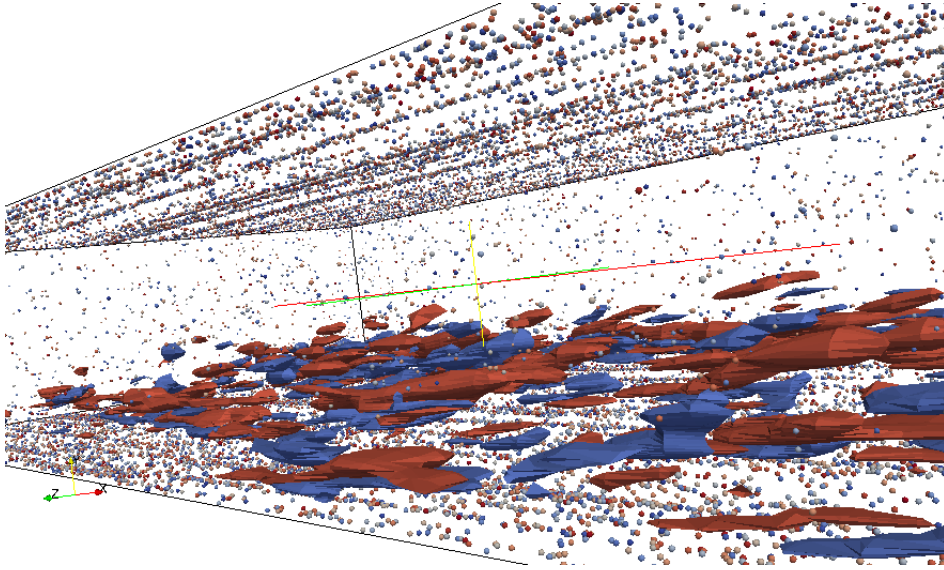


Figure 7.1: Snapshot of particles and vortical turbulent structures in the planar channel configuration.

The segregation of char particles near the wall is evident for both turbophoresis and for the presence of swirl driven flow. This latter cause has two main effects on segregation: one on the one hand it is more enhanced (maybe due to the bigger velocity of impact at wall), on the other hand it appears to take place within a relatively short time since particle injection (see Figure 5.34). Moreover this time scale is compatible with the average residence time of char particles in a gasifier.

In order to model the particle-wall interaction, the wall has been treated as a not perfectly elastic wall defining a coefficient for the normal-wall momentum restitution ϵ (in chapter 6 some very recent results that consider the effect of the tangential friction at wall are shown). Results show that limited effect of the restitution coefficient is observed on turbophoresis, when switching from a complete ($\epsilon = 1$) to partial ($\epsilon = 0.2$) restitution (see Figure 5.14 and Figure 5.15). In the presence of swirl driven flow, the effect of the restitution coefficient is observed in the velocity of segregation to take place (see Figure 5.34); in particular the lower is the restitution, the lower is time of segregation to take place.

Different particle classes representative of partially burned coal particles are been considered. The dimensionless parameter chosen to represent the different particle inertia due to different particle size has been the Stokes number. For both turbulence and swirl effect, segregation has been shown

to be enhanced for coarser particles (bigger Stokes number).

Numerical results show that, invariably with the chosen parameters, particle concentration near the wall in all the simulated cases does not appear perfectly uniform and steady. The spatial distribution of the particles near the wall, as appearing from snapshots in the case of the planar channel flow, is reported in Figure 5.23. Different levels of clustering are clearly recognizable, for instance looking at the regions indicated with letters A and B. The maximum local particle concentration shows values significantly higher than the averaged values. Results for this case suggest that, even when surface particle distribution is fully governed by turbophoretic effects, different levels of segregation can coexist, shedding doubts on models that assume uniform particle deposition rates onto the slag. A similar but even more enhanced behavior is observed in the curved channel flow, as clearly recognizable in Figure 5.18. Furthermore, the presence of dense particle clusters introduces a kind of *roughness* into the limiting gas/slag interface, that can be expected to impact the particle segregation mechanism. This behavior cannot be simulated with the current version of the model, as it would be necessary to take into account both particle-particle interaction and the effects of particles on the fluids in both the density and momentum balances.

The clustering structures are clearly unsteady as can be understood by looking at the Figure 5.33 and Figure 5.34 in which is shown that for both channel configurations the maximum particle concentration is an oscillating function of time.

Beside the regime SC, the analysis of the experimental evidence (see section 1.3) showed the presence of particles belonging to the entrapment regime E. Results shown that the order of magnitude of the particle impact velocity onto the slag surface is very low. This is a clue on the hypothesis, supposed by Montagnaro & Salatino (2010), that the entrapment regime is not probably due to ballistic reasons.

7.2 Future works

At the present day, the results investigation is oriented in order to modeling and analyze the effects of the no-elasticity of the wall, that represents the slag covering, also in the wall-parallel direction. Simulations at the LES level of the multilevel approach are then conducted on the planar channel configured in the exactly same way for both fluid and particle phases, except for the particle-wall interaction in which the value of the inelastic restitution coefficient in the wall-parallel direction is changed from perfect elasticity.

In order to obtain accurate results in particle-laden flow simulations, some

work has been done for validation. As shown in section 5.4.5, the segregation effects leads to a formation of not dilute layers of dispersed particle. To improve accuracy, has been already modeled the effect of the two-way coupling between particle and gas phases. The effect of the two-way coupling, instead of the more approximate one-way, is already under investigation.

An additional modeling effort is under way, by the author and by the research group in which it is included, to take into account the effect of particle-particle collisions that are more relevant in dense dispersed phase. The implementation of the four-way coupling seems to be already implemented in some libraries of newer releases of OpenFOAM, the numerical CFD package used in this work. There is also an investigation for other possible computational solutions (different from OpenFOAM) that implement the particle-particle interaction.

The dispersed phase tracking can be also modeled considering secondary forces acting on particles. It may be considered, for example, the effect of the lift force, that can be significant in the boundary layers of both channel configurations.

It should be considered that the multilevel model is very well parametrized so, a more accurate tuning can be done on several parameters such as:

- different particle size distribution (no more uniform d_p but a more realistic and interesting distribution) to represent particles with different inertia due, for example, to the different residence time in the gasifier.
- different turbulence levels characterized by different Re_{tau} values; In order to set different Re_{tau} values, different pressure gradient values can be imposed in the planar channel and different angular velocity of the inner wall can be imposed in the curved channel configuration.
- the swirl effect can be tuned by changing the swirl number of the gasifier (through the swirl velocity at the inlet) and the angular velocity of the inner wall in the curved channel configuration.

In order to setup predictive simulations, in future, a proper and more realistic modeling of the gasifier conditions has to be made. In fact the real fluid dynamic field in a gasifier are characterized by operating conditions that, first of all, are very far to be at ambient pressure and temperature. A non uniform temperature field indeed is responsible of termophoretic effects on particles. An other important improvement in the modeling, in order to have more predictive simulations, is to consider the kinetics effect on the dispersed phase. The aim should be to relating particle properties, such as their size or stickiness, to some aspects of the underlying complex chemical phenomena, for instance the conversion degree of the single coal particle.

Appendix A

OpenFOAM

Here will be discussed and illustrated in more details the numerical implementation of the computed simulations described in chapter 5. As mentioned in chapter 4 the numerical work is done through the use of OpenFOAM package (OpenCFD, 2008), starting from version 1.5 at the very beginning to 1.6.x at present days. The latter version is a bug-fixed version so it is continuously updated and was recompiled several times. So in this chapter all the source code illustrated and discussed is referred to the **1.6.x** version.

Will be in particular discussed about the numerical solvers designed and used to do the numerical simulations on the configurations related to the multilevel approach and on the mentioned improvement of the numerical library that implement the Lagrangian Particle Tracking model.

A.1 The solvers

To solve the Navier-Stokes equations the solvers is implemented with the pressure-implicit split-operator (*PISO*) algorithm. The solvers are made to solve transient compressible flow fields although the operating conditions are of incompressible flow.

Each equation is solved with an iterative method: preconditioned conjugate (bi-conjugate for asymmetric matrices) gradient to solve each discretized equation; the conditioner method is Diagonal Incomplete-Cholesky for symmetric and Diagonal Incomplete-LU for asymmetric matrices. The time-step used at RANS level is adjustable at run time with the condition of the maximum Courant number value of 0.3; simulations at LES level have a fixed time-step value of $dt = 0.0002$ s.

In OpenFOAM the discretization is managed (on a user hand) by setting a dictionary in which are specified the numerical scheme for discretize each

numerical operator (gradient, divergence, laplacian ...) of each discretized equation. In simulation described in this work are used:

- linear (central differencing) scheme for interpolations;
- standard second order finite volume discretization (Gaussian integration with linear scheme for interpolating values from cell centers to face centers) for gradient terms (except for the pressure gradient in the U-RANS level that is discretized with a second order scheme);
- second order scheme for divergence terms;
- unbounded second order conservative scheme for laplacian terms;
- explicit non-orthogonal correction for surface normal gradient terms;
- implicit second order scheme for time derivative terms.

A.1.1 Turbulence modeling

In the U-RANS level of the multilevel approach the *kOmegaSST* implementation of the compressible version of the $k - \omega$ SST model is used. Wall functions are applied to turbulent properties, particularly:

variable:	wall function
k	compressible::kqRWallFunction
ω	compressible::omegaWallFunction
α_t	compressible::alphanWallFunction
ϵ	compressible::epsilonWallFunction
μ_t	compressible::mutWallFunction

In the LES level of the multilevel approach the *dynOneEqEddy* implementation of the compressible version of localized dynamic model LDKM is used:

```
dynOneEqEddyCoeffs
{
    ce          1.05;
    filter      simple;
}
```

A.2 Improvement in the standard LPT algorithm

As described in section 4.3.1 when a particle radius (that is the distance from the particle position represented by its center and the actual particle surface) is bigger then the height of the mesh cell closer to the wall, the collision model goes wrong because the collision should happen when the particle (its center) is in an interior mesh cell and not in a boundary one. The author has proposed and implemented a correction that have the aim of simulate a correct wall rebound of particles bigger then the height of the wall boundary mesh cells.

The correction has been implemented to be act only in the planar channel configuration in order to be more efficient and to significantly improve the computing speed.

In Figure A.1 is shown the particle mass fraction α/α_0 along y^+ , 30 seconds after particle injection, for different wall impact algorithms: as it is possible to see there are many particles with a center position too much close to the wall (wrong position) with the standard LPT calculation. The maximum particle concentration value is more close to the wall. Being particle velocity interpolated up to zero on the wall, particles that are too close to the wall tend to do not bounce away from it. The effect is an accumulation in time of particles too much close to the the wall that leads to an overestimation of the maximum particle concentration value. With the standard wall collision model, for particle with $d_p = 102 \mu m$, the maximum concentration value is resulting as a growing function of time in the planar channel configuration; this is a numerical error effect.

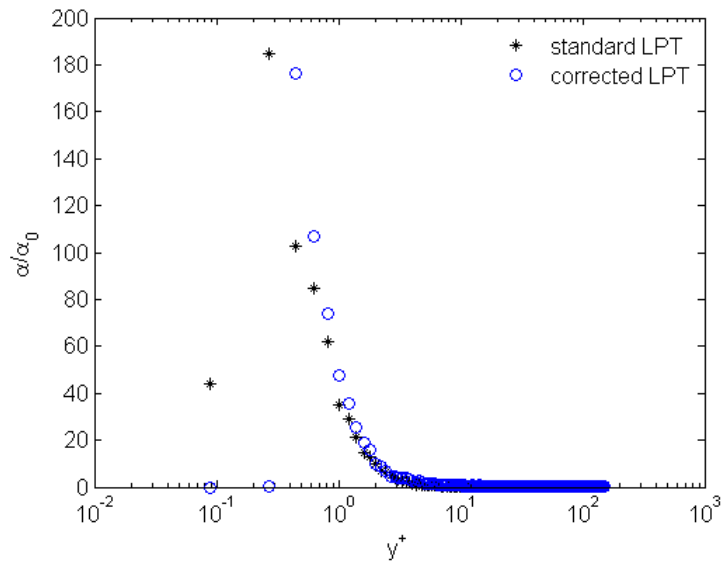


Figure A.1: Particle mass fraction α/α_0 as a function of y^+ for different wall impact algorithms: $St = 25$, $\epsilon = 1$, $T = 80$ s, planar channel configuration;

Appendix B

Planar channel driving force

Here are briefly described the computations done to ensure an average flow field that have the particular value of $Re_\tau = 150$ in the planar channel configuration. As described in Pope (2000) the lateral mean-momentum equation reduces to

$$0 = -\frac{d}{dy} \langle v^2 \rangle - \frac{1}{\rho} \frac{\partial \langle p \rangle}{\partial y} \quad (\text{B.1})$$

which, with the boundary condition $\langle v^2 \rangle_{y=0}$, integrates to

$$\langle v^2 \rangle + \frac{\langle p \rangle}{\rho} = \frac{p_w(x)}{\rho} \quad (\text{B.2})$$

where $p_w = \langle p(x, 0, 0) \rangle$ is the mean pressure on the bottom wall. So the mean axial pressure gradient is uniform across the flow:

$$\frac{\partial \langle p \rangle}{\partial x} = \text{const} = \frac{dp_w}{dx} \quad (\text{B.3})$$

The axial momentum equation can be written

$$\frac{\partial \tau}{\partial y} = \frac{dp_w}{dx} \quad (\text{B.4})$$

where the total shear stress $\tau(y)$ is

$$\tau = \rho\nu \frac{d \langle u \rangle}{dy} - \rho \langle uv \rangle \quad (\text{B.5})$$

So τ is a linear function of y . Defining

$$\tau_w \equiv \tau(0) \quad (\text{B.6})$$

and being $\tau(y)$ antisymmetric respect to the mid-plane, it follows that $\tau(h) = 0$ and $\tau(2h) = -\tau_w$. Hence the solution of the Eq. (B.4) is

$$-\frac{dp_w}{dx} = \frac{\tau_w}{h}. \quad (\text{B.7})$$

Being, by definition, the friction velocity u_τ

$$u_\tau \equiv \sqrt{\frac{\tau_w}{\rho}} \quad (\text{B.8})$$

then, from Eq. (B.7), the pressure gradient can be written

$$\frac{dp_w}{dx} = -\frac{\rho}{h} u_\tau^2 \quad (\text{B.9})$$

Then to obtain a particular value of Re_τ in a fully developed turbulent channel flow, it has been set a $\Delta P/L$ value given by

$$\frac{\Delta P}{L_x} = u_\tau^2 \frac{\rho}{h} \quad (\text{B.10})$$

where

$$u_\tau = Re_\tau \frac{\nu}{h}$$

Appendix C

On the initial conditions in the Gasifier simulations

The U-RANS simulation of the first level of the multilevel approach (see section 5.2) is based on the gasifier prototype proposed by Sommerfeld & Qiu (1993) and studied also by other research groups (for example Apte *et al.*, 2003). In order to eventually compare results, an effort has been made to set up the simulation in the same conditions of the benchmark experiment. In order to set up proper simulation parameters, such as gas density and viscosity, fluid velocity profile at inlet in both central and annular swirled jets, some calculations have to be done on parameters related to the configuration proposed by Sommerfeld & Qiu (1993). Using subscript *1* to indicate variables related to the central inlet of the jet and subscript *2* to indicate those related to the annular swirled jet is possible to summarize:

$$\begin{aligned}G_1 &= 9.9 \cdot 10^{-3} \text{ kg s}^{-1} \\G_2 &= 38.3 \cdot 10^{-3} \text{ kg s}^{-1} \\A_1 &= 8.04 \cdot 10^{-4} \text{ m}^2 \\A_2 &= 2.08 \cdot 10^{-3} \text{ m}^2 \\U_{ref} &= 12.89 \text{ m s}^{-1} \\Re &= 26200 \\S_n &= 0.47\end{aligned}$$

where G_1 and G_2 are the mass flow rate of the primary and secondary inlet respectively, A_1 and A_2 are the surface area of the two separated inlets, U_{ref} and Re are the axial reference velocity and the Reynolds number respectively, both related to the entire inlet, S_n is the swirl number.

Being $R = 0.032 \text{ m}$ the radius of the entire inlet jet, the inlet area is

$A = R^2\pi$. Hence is possible to calculate the density of the flow ρ as

$$\rho = \frac{G_1 + G_2}{A} \frac{1}{U_{ref}}$$

obtaining $\rho = 1.162 \text{ kg m}^{-3}$ and then the axial velocities of the two separated inlets as

$$V_1 = \frac{G_1}{A_1} \frac{1}{\rho} = 10.59 \text{ m s}^{-1}$$

$$V_2 = \frac{G_2}{A_2} \frac{1}{\rho} = 15.82 \text{ m s}^{-1}$$

Being

$$Re = \frac{\rho R U_{ref}}{\mu} \Rightarrow \mu = \frac{\rho R U_{ref}}{Re} = 1.83 \cdot 10^{-5} \text{ kg m}^{-1} \text{ s}^{-1}$$

then

$$\nu = \frac{\mu}{\rho} = 1.57 \cdot 10^{-5} \text{ m}^2 \text{ s}^{-1}$$

The swirl number is considered to be the ratio of the axial flux of angular momentum to the axial flux of linear momentum, which were obtained by integration across both the primary and annular inlets. So the following definition of the swirl number is used:

$$S_n = \frac{\int_{A_3} \rho v_z (v_\theta r) \text{ d}A}{R_c \int_{A_3} \rho v_z^2 \text{ d}A} \quad (\text{C.1})$$

where $R_c = 0.096 \text{ m}$ is the radius of the combustor chamber, r is the radial coordinate, v_z and v_θ are the axial and tangential velocity respectively and $A_3 = A_1 \cup A_2$ is the total inlet area.

Considering that in Eq. (C.1) $\rho = \text{const}$, $v_z = V_1 = \text{const}$ in A_1 and $v_z = V_2 = \text{const}$ in A_2 , $\text{d}A = 2\pi r \text{ dr}$, $v_\theta = 0$ in A_1 and putting $v_\theta(r) = \omega r$ with $\omega = \text{const}$ in A_2 , the value of $\omega = 1209 \text{ s}^{-1}$ is obtained for the swirl number value of $S_n = 0.47$.

Bibliography

- Ambrosino, Fiorenzo, Arovitola, Andrea, Brachi, Paola, Marra, Francesco Saverio, Montagnaro, Fabio, & Salatino, Piero. 2011a. Char-Slag Interaction During Entrained-Flow Gasification: from Experimental Evidence to Numerical Simulations. *In: 12th International Conference Multiphase Flow in Industrial Plants, Ischia, Italy - September 21-23*.
- Ambrosino, Fiorenzo, Arovitola, Andrea, Brachi, Paola, Marra, Francesco Saverio, Montagnaro, Fabio, & Salatino, Piero. 2011b. Numerical modeling of char particle segregation in entrained-flow slagging gasifiers. *In: 12th International Conference Multiphase Flow in Industrial Plants, Ischia, Italy - September 21-23*.
- Apte, S. V., Mahesh, K., Moin, P., & Oefelein, J. C. 2003. Large-eddy simulation of swirling particle-laden flows in a coaxial-jet combustor. *International Journal of Multiphase Flow*, **29**(8), 1311–1331.
- Barroso, J., Ballester, J., & Pina, A. 2007. Study of coal ash deposition in an entrained flow reactor: Assessment of traditional and alternative slagging indices. *Fuel Processing Technology*, **88**(9), 865–876.
- Benyon, Peter John. 2002. *Computational Modelling of Entrained Flow Slagging Gasifiers*. Ph.D. thesis, School of Aerospace, Mechanical & Mechatronic Engineering - University of Sydney.
- Bockelie, Mike, Swensen, Dave, & Denison, Martin. 2002. *A Computational Workbench Environment for Virtual Power Plant Simulation - Quarterly Progress Report - Reporting Period Start Date: January 1, 2002 End Date: March 31, 2002*. Tech. rept. Reaction Engineering International.
- Bracco, G., Podda, S., Migliori, S., D'Angelo, P., Quintiliani, A., Giammattei, D., De Rosa, M., Pierattini, S., Furini, G., Guadagni, R., Simoni, F., Perozziello, A., Gaetano, A. De, Pecoraro, S., Santoro, A., Scio, C., Rocchi, A., Funel, A., Raia, S., Aprea, G., Ferrara, U., Novi, D., , & Guarnieri,

- G. 2009. CRESCO HPC System Integrated into ENEA-GRID Environment. *In: FINAL WORKSHOP OF GRID PROJECTS, PON RICERCA 2000-2006, AVVISO 1575.*
- Chen, Caixia, Horio, Masayuki, & Kojima, Toshinori. 2001. Use of numerical modeling in the design and scale-up of entrained flow coal gasifiers. *Fuel*, **80**(18), 1513–1523.
- Costen, P.G., Lockwood, F.C., & Siddique, M.M. 2000. Mathematical modeling of ash deposition in pulverized fuel-fired combustors. *Proceedings of the Combustion Institute*, **28**(2), 2243–2250.
- Crowe, Clayton T. (ed). 2006. *Multiphase Flow handbook*. CRC Press.
- Crowe, Clayton T., & Michaelides, Efstathios E. 2006. *Multiphase Flow Handbook*. CRC Press. Chap. 1 - Basic Concepts and Definitions.
- Elghobashi. 2006. *Multiphase Flow Handbook*. CRC Press. Chap. 13 - Modeling, pages 34–36.
- Fan, J. R., Jin, J., Zhang, X. Y., & Cen, K. F. 2001. A numerical model for dense particle-laden jets. *Powder Technology*, **115**(3), 256–264.
- Fang, Qingyan, Wang, Huajian, Wei, Yan, Lei, Lin, Duan, Xuelong, & Zhou, Huaichun. 2010. Numerical simulations of the slagging characteristics in a down-fired, pulverized-coal boiler furnace. *Fuel Processing Technology*, **91**(1), 88–96.
- Garnier, E., Adams, N., & Sagaut, P. 2009. *Large Eddy Simulation for Compressible Flows*. Springer.
- Germano, Massimo, Piomelli, Ugo, Moin, Parviz, & Cabot, William H. 1991. A Dynamic Subgrid-Scale Eddy Viscosity Model. *Phys. Fluids A*, **3** (7), 1760–1765.
- Guha, Abhijit. 2008. Transport and Deposition of Particles in Turbulent and Laminar Flow. *Annual Review of Fluid Mechanics*, **40**, 311–341.
- Hill, S. C., Eaton, A. M., & Smoot, D. 2000. *Computational Fluid Dynamics in Industrial Combustion*. CRC Press. Chap. 4 - PCGC-3, pages 95–160.
- Horn, M., & Schmid, H.-J. 2008. A comprehensive approach in modeling Lagrangian particle deposition in turbulent boundary layers. *Powder Technology*, **186**, 189–198.

- Huang, L. Y., Norman, J. S., Pourkashanian, M., & Williams, A. 1996. Prediction of ash deposition on superheater tubes from pulverized coal combustion. *Fuel*, **75**(3), 271–279.
- Kim, W.-W., Menon, S., & Mongia, H. C. 1999. Large eddy simulations of a gas turbine combustor flow. *Combustion Science and Technology*, **143**, 25–62.
- Kuerten, J. G. M., & Vreman, A. W. 2005. Can turbophoresis be predicted by large-eddy simulation? *Phys. Fluids*, **17**, 011701(4).
- Lee, F. C. C., & Lockwood, F. C. 1999. Modelling ash deposition in pulverized coal-fired applications. *Progress in Energy and Combustion Science*, **25**(2), 117–132.
- LESinItaly, Group. 2011. A comparative test for assessing the performances of large-eddy simulation codes. *In: XX Congresso AIMETA, Bologna, 12-15 settembre*.
- Li, Suhui, Wu, Yuxin, & Whitty, Kevin J. 2010. Ash Deposition Behavior during Char-Slag Transition under Simulated Gasification Conditions. *Energy & Fuels*, **24**(3), 1868–1876.
- Loth, E. 2006. *Multiphase Flow Handbook*. CRC Press. Chap. 13 - Modeling, pages 1–20.
- Loth, E., Tryggvason, G., Tsuji, Y., Elghobashi, S.E., Crowe, C.T., Berlemont, A., Reeks, M., Simonin, O., Frank, Th., Onishi, Y., & van Wachem, B. 2006. *Multiphase Flow Handbook*. CRC Press. Chap. 13 - Modeling.
- Macpherson, Graham B., Nordin, Niklas, & Weller, Henry G. 2009. Particle tracking in unstructured, arbitrary polyhedral meshes for use in CFD and molecular dynamics. *Communications in Numerical Methods in Engineering*, **25**, 263–273.
- Marchioli, C., Salvetti, M. V., & Soldati, A. 2008a. Some issues concerning large-eddy simulation of inertial particle dispersion in turbulent bounded flows. *Phys. Fluids*, **20**(4), 040603–11.
- Marchioli, C., Soldati, A., Kuerten, J.G.M., Arcen, B., Tanire, A., Goldensohn, G., Squires, K.D., Cargnelutti, M.F., & Portela, L.M. 2008b. Statistics of particle dispersion in direct numerical simulations of wall-bounded turbulence: Results of an international collaborative benchmark test. *International Journal of Multiphase Flow*, **34**(8), 879–893.

- Marchioli, Cristian, Salvetti, Maria, & Soldati, Alfredo. 2008c. Appraisal of energy recovering sub-grid scale models for large-eddy simulation of turbulent dispersed flows. *Acta Mechanica*, **201**(1), 277–296.
- Martin, M.P., Piomelli, U., & Candler, G.V. 2000. *Theoretical and Computational Fluid Dynamics*, **13**, 361–376.
- Maurstad, O. 2005. *An overview of coal based integrated gasification combined cycle (IGCC) technology*. Tech. rept. Massachusetts Institute of Technology, Laboratory for Energy and the Environment. Cambridge, LFEE.
- Menter, Florian, Carregal, Jorge, Esch, Ferreira Thomas, & Konno, Brad. 2003. The SST Turbulence Model with Improved Wall Treatment for Heat Transfer Predictions in Gas Turbines. *In: International Gas Turbine Congress, Tokyo November 2-7*.
- Moin, P., Squires, K.D., Cabot, W., & Lee, S. 1991. *Physics of Fluids*, **A3**, 2746–2757.
- Mondal, P., Dang, G.S., & Garg, M.O. 2011. Syngas production through gasification and cleanup for downstream applications – Recent developments. *Fuel Processing Technology*, **92**(8), 1395–1410.
- Montagnaro, F., Brachi, P., & Salatino, P. 2011. Char-Wall Interaction and Properties of Slag Waste in Entrained-Flow Gasification of Coal. *Energy & Fuels*, **25**, 3671–3677.
- Montagnaro, Fabio, & Salatino, Piero. 2009. The Role of Slag Formation on Late Carbon Conversion in Entrained Flow Gasification of Coal. *In: Combustion Colloquia - 32nd Combustion Meeting, Napoli, April 2009*.
- Montagnaro, Fabio, & Salatino, Piero. 2010. Analysis of char-slag interaction and near-wall particle segregation in entrained-flow gasification of coal. *Combustion and Flame*, **157**(5), 874–883.
- Mueller, Christian, Selenius, Maria, Theis, Mischa, Skrifvars, Bengt-Johan, Backman, Rainer, Hupa, Mikko, & Tran, Honghi. 2005. Deposition behaviour of molten alkali-rich fly ashes—development of a submodel for CFD applications. *Proceedings of the Combustion Institute*, **30**(2), 2991–2998.
- Myhnen, Kari, & Hyppnen, Timo. 2011. A Three-Dimensional Model Frame for Modelling Combustion and Gasification in Circulating Fluidized Bed Furnaces. *International Journal of Chemical Reactor Engineering*, **9**, A25.

- OpenCFD (ed). 2008. *OpenFOAM Programmers Guide v. 1.6*.
- OpenCFD, Ltd. last visited October 2011. *OpenFOAM website:* <http://www.openfoam.com/>.
- Poinsot, T., & Veynante, D. 2001. *Theoretical and numerical combustion*.
- Pope, Stephen B. 2000. *Turbulent Flows*. Cambridge University Press.
- Pyykonen, Jouni, Jokiniemi, Jorma, & Jacobson, Tommy. 2002. Development of a Prediction Scheme for Pulverised Coal-Fired Boiler Slagging. *Pages 735–752 of: Gupta, R. P., Wall, T. F., & Baxter, L. (eds), Impact of Mineral Impurities in Solid Fuel Combustion*. Springer US.
- Ranade, Vivek V. 2002. *Computational Flow Modeling for Chemical Reactor Engineering*. Academic Press.
- Richards, Galen H., Slater, Peter N., & Harb, John N. 1993. Simulation of ash deposit growth in a pulverized coal-fired pilot scale reactor. *Energy & Fuels*, **7**(6), 774–781.
- Sagaut, P. 2001. *Large Eddy Simulation for Incompressible Flows*. Springer.
- Seggiani, M. 1998. Modelling and simulation of time varying slag flow in a Prenflo entrained-flow gasifier. *Fuel*, **77**(14), 1611–1621.
- Shannon, G.N., Rozelle, P.L., Pisupati, Sarma V., & Sridhar, S. 2008. Conditions for entrainment into a FeO_x containing slag for a carbon-containing particle in an entrained coal gasifier. *Fuel Processing Technology*, **89**(12), 1379–1385.
- Shimizu, Tadaaki, & Tominaga, Hiroaki. 2006. A model of char capture by molten slag surface under high-temperature gasification conditions. *Fuel*, **85**(2), 170–178.
- Silaen, Armin, & Wang, Ting. 2010. Effect of turbulence and devolatilization models on coal gasification simulation in an entrained-flow gasifier. *International Journal of Heat and Mass Transfer*, **53**(9-10), 2074–2091.
- Slezak, Andrew, Kuhlman, John M., Shadle, Lawrence J., Spenik, James, & Shi, Shaoping. 2010. CFD simulation of entrained-flow coal gasification: Coal particle density/sizefraction effects. *Powder Technology*, **203**(1), 98–108.

- Snider, Dale M., Clark, Samuel M., & O'Rourke, Peter J. 2011. Eulerian-Lagrangian method for three-dimensional thermal reacting flow with application to coal gasifiers. *Chemical Engineering Science*, **66**(6), 1285–1295.
- Soldati, Alfredo. 2005. Particles turbulence interactions in boundary layers. **85**(1), 683–699.
- Sommerfeld, M. 2000. Overview and Fundamentals. *In: Theoretical and Experimental Modelling of Particulate Flows*. Lecture Series 2000-06. von Karman Institute for Fluid Dynamics.
- Sommerfeld, M., & Qiu, H.-H. 1993. Characterization of particle-laden, confined swirling flows by phase-doppler anemometry and numerical calculation. *International Journal of Multiphase Flow*, **19**(6), 1093–1127.
- Sun, Bo, Liu, Yongwen, Chen, Xi, Zhou, Qulan, & Su, Ming. 2011. Dynamic modeling and simulation of shell gasifier in IGCC. *Fuel Processing Technology*, **92**(8), 1418–1425.
- Tomeczek, Jerzy, Palugniok, Henryk, & Ochman, Jzef. 2004. Modelling of deposits formation on heating tubes in pulverized coal boilers. *Fuel*, **83**(2), 213–221.
- Tominaga, H., Yamashita, T., Ando, T., & Asahiro, N. 2000. Simulator Development of Entrained Flow Coal Gasifiers at High Temperature and High Pressure Atmosphere. *The IFRF Electronic Combustion Journal*, **200004**.
- Vreman, B., Geurts, B., & Kuerten, H. 1996. *International Journal for Numerical Methods in Fluids*, **22**, 297–311.
- Wang, Q., Squires, K. D., Chen, M., & McLaughlin, J. B. 1997. On the role of the lift force in turbulence simulations of particle deposition. *International Journal of Multiphase Flow*, **23**(4), 749–763.
- Wang, X.H., Zhao, D.Q., He, L.B., Jiang, L.Q., He, Q., & Chen, Y. 2007. Modeling of a coal-fired slagging combustor: Development of a slag sub-model. *Combustion and Flame*, **149**(3), 249–260.
- Watanabe, H., & Otaka, M. 2006. Numerical simulation of coal gasification in entrained flow coal gasifier. *Fuel*, **85**(12-13), 1935–1943.
- Watanabe, Hiroaki, Kurose, Ryoichi, & KOMORI, Satoru. 2009. Large-Eddy Simulation of Swirling Flows in a Pulverized Coal Combustion Furnace

- with a Complex Burner. *Journal of Environment and Engineering*, **4**, 1–11.
- White, Frank M. 1991. *Viscous Fluid Flow*. 2nd edn. McGraw-Hill.
- Wu, C.L., Berrouk, A.S., & Nandakumar, K. 2009. Three-dimensional discrete particle model for gas-solid fluidized beds on unstructured mesh. *Chemical Engineering Journal*, **152**(2-3), 514–529.
- Wu, Tao, Gong, Mei, Lester, Ed, Wang, Fuchen, Zhou, Zhijie, & Yu, Zunhong. 2007. Characterisation of residual carbon from entrained-bed coal water slurry gasifiers. *Fuel*, **86**(7-8), 972–982.
- Xu, Qiang, Yang, Xiongtao, Liu, Chaowei, Li, Kuyen, Lou, Helen H., & Gossage, John L. 2009a. Chemical Plant Flare Minimization via Plantwide Dynamic Simulation. *Industrial & Engineering Chemistry Research*, **48**(7), 3505–3512.
- Xu, Shenqi, Zhou, Zhijie, Gao, Xuxia, Yu, Guangsu, & Gong, Xin. 2009b. The gasification reactivity of unburned carbon present in gasification slag from entrained-flow gasifier. *Fuel Processing Technology*, **90**(9), 1062–1070.
- Zhao, Xianglong, Zeng, Cai, Mao, Yanyan, Li, Wenhua, Peng, Yun, Wang, Tao, Eiteneer, Boris, Zamansky, Vladimir, & Fletcher, Thomas. 2010. The Surface Characteristics and Reactivity of Residual Carbon in Coal Gasification Slag. *Energy & Fuels*, **24**(1), 91–94.
- Zhou, Haosheng, Flamant, Gilles, & Gauthier, Daniel. 2007. Modelling of the turbulent gas-particle flow structure in a two-dimensional circulating fluidized bed riser. *Chemical Engineering Science*, **62**(1-2), 269–280.